Seismoelectric signals from earthquakes: detection, analysis and interpretation

Dissertation
zur Erlangung des Doktorgrades
der Mathematisch - Naturwissenschaftlichen Fakultät
der Christian-Albrechts-Universität zu Kiel

vorgelegt von

Laura Dorothee Dzieran

Kiel, 2020

Erster Gutachter: Prof. Dr. Wolfgang Rabbel
Zweiter Gutachter: Prof. Dr. Stéphane Garambois

Tag der mündlichen Prüfung: 18.05.2020

Zusammenfassung

Wenn sich seismische Kompressionswellen im Untergrund ausbreiten, können auf Grund elektrokinetischer Kopplungseffekte ‘seismoelektrische’ (SE) Signale erzeugt werden. Diese SE-Signale reagieren sowohl auf poroelastische als auch auf elektrische Gesteinseigenschaften sensitiv, während ihr Auflösungsvermögen dem von seismischen Wellen ähnelt. Es besteht daher die Möglichkeit mit SE-Untersuchungen Erkenntnisse zu erweitern, die ansonsten mit klassischen geophysikalischen Methoden gewonnen werden.

SE-Signale werden in der Regel in ‘koseismische’ Wellen und ‘Interface Responses’ (IRs - Signale von Grenzflächen) unterschieden. Koseismische Wellen sind an seismische Wellen gekoppelt und enthalten daher nur Informationen über die direkte Umgebung der jeweiligen Messstation. IRs werden erzeugt, wenn die (ko)seismischen Wellen elektrische oder hydraulische Diskontinuitäten überqueren. Sie reagieren sensitiv auf die Porosität und Permeabilität der Gesteine sowie auf die Salinität und Viskosität der Porenfluide. Da sich IRs unabhängig vom seismischen Wellenfeld ausbreiten, können aus ihnen auch Informationen aus einiger Entfernung zur Messstation gewonnen werden. Für gewöhnlich liegt daher das Hauptaugenmerk bei SE-Untersuchungen auf den IRs.

Das Ziel dieser Dissertation ist es, SE-Signale zu untersuchen, die durch Erdbeben erzeugt werden. Ein besonderer Fokus liegt dabei auf der Detektierung, der Analyse und der Interpretation der Signale. Während durch Erdbeben erzeugte koseismische Signale bereits beobachtet wurden, steht die Identifizierung von erdbeben-erzeugten IRs noch aus.

Im ersten Teil dieser Arbeit werden Abstand-Magnituden-Grenzwerte präsentiert, welche die Möglichkeit quantifizieren, SE-Signale zu beobachten. Anhand über 16 000 Erdbeben wurde ermittelt, dass 67 % der Beben mit einer Magnitude größer als $2.3 \cdot \log_{10}(\mathrm{r/km})$ in einer Hypozentraldistanz r klar identifizierbare SE-Signale hervorrufen, falls der lokale Rausch-Pegel unterhalb von $0.1\,\mu\mathrm{V/m}$ liegt. Des Weiteren konnte durch SE-Signale, die in der Atacama Wüste in Nord-Chile aufgenommen wurden, ein lokaltionsspezifisches Signalverhalten nachgewiesen werden. Dazu wurden im Zeitbereich seismische und SE-Einhüllenden (Envelopen) miteinander verglichen und im Frequenzbereich seismoelektrische spektrale Verhältnisse (SESRs) als ein neues Konzept zur Evaluierung des Einflusses von IRs auf das Gesamtsignal, vorgestellt.

Das Prinzip der SESRs wird im zweiten Teil der Dissertation detaillierter untersucht. Unter anderem mit Hilfe eines Inversions-Algorithmus wurde ein aus Felddaten berechneter SESR synthetisch nachmodelliert. Die Berechnungen zeigten, dass die Form des SESRs hauptsächlich durch IRs, die in den ersten paar hundert Metern des Untergrundes erzeugt werden, beeinflusst wird. Dabei reagierte der untersuchte SESR sensitiv auf die Porosität des Untergrundes, die Salinität des Porenfluids und die Tiefenlage der IR erzeugenden Grenzflächen.

Im letzten Teil der Dissertation werden numerische SE-Signale analysiert, die auf Grundlage eines mehrschichtigen Untergrundmodells berechnet wurden. Ziel ist es, ein eventuelles passives SE-Feldexperiment auf der Armutlu Halbinsel in der Türkei zu simulieren. Die Ergebnisse zeigen, dass die Möglichkeit einzelne IRs in einem SE-Wellenzug zu identifizieren, am größten ist, wenn die Messgeräte nah am Epizentrum der Beben platziert sind. Durch die Analyse der synthetischen SESRs und SE-Einhüllenden konnten zudem Porositäts- und Salinitäts-Änderungen im oberen Erdboden detektiert werden. Bei einem realen Feldexperiment würden jedoch - abhängig vom lokalen Rausch-Pegel - aller Voraussicht nach die geringen Amplituden der SE-Signale eine Herausforderung darstellen.

Zusammenfassend zeigen die Untersuchungen dieser Dissertation, dass durch Erdbeben generierte SE-Signale innerhalb einer begrenzten Entfernung zum Hypozentrum detektiert werden können, falls die Beben-Magnituden groß genug sind, dass die erzeugten SE-Amplituden den anthropogenen Rausch-Pegel übersteigen. Der Weite des Detektierradius ist dabei abhängig von dem Ziel der Messung (Observation von IRs oder koseismischen Wellen). Wenn das Signal/Rausch-Verhältnis ausreichend gut ist, könnten SESRs und die Analyse von Einhüllenden genutzt werden, um Porositäts- und Salinitäts-Änderungen in den oberen hunderten Metern des Untergrundes zu detektieren. Dabei müssen die Ergebnisse jedoch vermutlich mit weiteren Informationen eingegrenzt werden. Um die Schlussfolgerungen dieser Dissertation zu verifizieren, werden Feldmessungen empfohlen.

Summary

When seismic pressure waves propagate through the subsurface they can excite 'seismoelectric' (SE) signals via electrokinetic coupling. These SE signals are sensitive towards poroelastic as well as electrical properties while providing the resolutions of seismic measurements. They might therefore add information to conventional geophysical measurements.

SE signals are generally divided into coseismic waves and interface responses (IRs). The coseismic waves are bound to seismic waves and can therefore only reveal information about the direct vicinity of the recording stations. Interface Responses (IRs) are excited when the (co)seismic waves cross electric or hydraulic discontinuities. They are sensitive to the rocks' porosity and permeability as well as the salinity and viscosity of the pore fluids. As they propagate independently from the seismic fields they can contain information from interfaces further away from the recording stations. Therefore, IRs are usually the main focus of SE investigations.

The goal of this thesis is to investigate SE signals generated by earthquakes with a special focus on the detection, analysis and interpretation of these signals. While coseismic signals have been observed during earthquakes, IRs have yet to be detected.

In the first part of this thesis distance-magnitude-thresholds are established that quantify the possibility to observe SE signals from earthquakes. Based on over 16,000 events we found that 67 % of earthquakes with magnitude $\mathrm{M} \geq 2.3 \cdot \log_{10}(\mathrm{r}/\mathrm{km})$ at hypocentral distance r showed clear SE signals if the noise level is below 0.1 µV/m. Furthermore we confirmed the site-dependency of SE earthquake signals recorded in the Atacama Desert of Northern Chile by comparing seismic and SE envelopes and introducing SE spectral ratios (SESRs) as a new concept to evaluate the influence of IRs on SE signals in the frequency domain.

The concept of SESRs is explained in the second part of this thesis in more detail. We approximated a SESR calculated from field data through synthetic modelling with the help of an inversion algorithm. The calculations implied that the shape of the SESR is primarily influenced by IRs generated in the first few hundred meters of the subsurface and that a sensitivity exists towards to the rock's porosity, the pore-fluid's salinity and the depth of the interfaces that generate IRs.

Last but not least, the response of numerical SE signals to a multi-layered subsurface model was analysed, simulating a possible passive SE field experiment on the Armutlu Peninsula in Turkey. The results showed that the chance to identify single IRs in a SE wavetrain is highest if the recording stations are placed close to the epicenter of the earthquakes. Through the analysis of SESRs and SE envelopes, porosity and salinity changes in the upper subsurface could be detected. Nevertheless, depending on the local noise level the estimated small amplitudes of the field data will provide a challenge.

All in all, the investigations of this thesis showed that SE signals can be detected in a limited radius from the hypocenter if the magnitudes of the earthquakes are large enough for the generated SE amplitudes to overcome the anthropogenic noise-level. The detection radius thereby depends on the observation target (IRs or coseismic signals). If the signal-to-noise ratio is sufficient, SESRs as well as envelope analysis could be used to detect porosity and salinity changes in the first few hundred meters of the subsurface, although the results have probably to be constrained by previous information. Field measurements are now required to verify the findings of this thesis.

Contents

1 Introduction

A glossary of all coefficients appearing in this chapter can be found at the end of this chapter (section 1.7)

1.1 Motivation

When seismic waves propagate through the subsurface they can be accompanied by so-called seismoelectric (SE) signals. One explanation for the generation of these signals are electrokinetic coupling effects in the electric double layer between the rock matrix and the pore-fluids (see section 1.4).

SE signals have been researched sporadically since the late 1930's and more intensively since the 1990's (see section 1.2). But although the number of publications focusing on SE waves is constantly increasing, the attention towards this particular field of research is still small in the geophysical community. This is surprising since SE signals offer a lot of potential. While being sensitive towards poroelastic parameters, such as porosity or the pore-fluid's conductivity, SE signals additionally provide a resolution similar to seismic waves.

SE signals have successfully been recorded and evaluated during field experiments with artificial seismic sources (see section 1.2). Besides that, SE signals have also been observed during earthquakes. An advantage of analysing SE signals from earthquakes is that earthquakes are usually associated with higher energies than artificial seismic sources, which could for example lead to greater investigation depths. On the downside, passive SE field experiments are more difficult to control, since source strength and position cannot be influenced. Nevertheless one hope when analysing earthquake generated SE signals is that they can provide new insights into nucleation processes and/or earthquake associated variations of the subsurface.

The number of publications focusing on SE signals generated by earthquakes is not overwhelmingly large, yet. Furthermore, most of these studies focus on the numerical investigation of general concepts, like for example the generation of and distinction between different SE signal-types. However, if one wants to explore the potential of SE signals generated by earthquakes, field experiments and their evaluations are inevitable. The focus of this thesis therefore lies on earthquake generated SE signals that can be measured during passive SE field studies. The goal is to analyse the probabilities to detect the SE signals, develop approaches to analyse them and evaluate interpretation possibilities. The hope is to broaden the knowledge about SE signals generated by earthquakes in general, while keeping in mind the possibilities of future field experiments.

1.2 History of seismoelectric research

The investigation of SE signals started in the late 1930's when first observations of coupling effects between seismic and electromagnetic (EM) wavefields were reported (Blau and Statham, 1936; Thompson, 1936, 1939; Ivanov, 1939). Shortly afterwards Frenkel (1944) offered a first theoretical approach for an "electrification" of elastic waves, calling it the "seismoelectric effect of the second kind". Due to its historic significance Frenkels paper was republished in 2005 (Frenkel, 2005) although he did not consider the whole set of Maxwell's equations limiting his calculations to the coseismic electric field (Pride and Garambois, 2005). Following Frenkels paper in 1944, the overall interest in SE phenomena remained small, even though Martner and Sparks (1959) claimed to have recorded electrical signals arriving before seismic waves from an explosion source.

It wasn't until the 1990's that the so-called SE effect came back into focus. In 1993 Thompson and Gist successfully observed an interface response (IR) from a 300 m deep gas-water interface. One year later Pride (1994) derived a set of governing equations - that were later complemented by two follow-up papers (Pride and Haartsen, 1996; Haartsen and Pride, 1997) - describing the coupling between seismic and EM waves in a fully saturated medium. Today, it is commonly accepted that it was Prides work that reintroduced the interest in SE research to the geophysical community.

This newly found interest in SE research led to a variety of field experiments (e.g. Butler et al., 1996; Dupuis et al., 2007; Strahser et al., 2011), laboratory studies (e.g. Block and Harris, 2006; Bordes et al., 2008; Holzhauer et al., 2016) and numerical investigations (e.g. Garambois and Dietrich, 2002; Revil and Jardani, 2010; Kröger et al., 2013). A detailed overview on SE studies since the 1990's can be found in chapter 1 of Maureen Devi's PhD-thesis (Devi, 2017).

Pride's governing equations were developed for fully saturated media. In 2013, Warden et al. extended these equations to include partially saturated materials. At the same time, Revil et al. (2013) proposed an alternative approach towards the SE theory suggesting a poro-acoustic model coupled with dynamic electrokinetic theory for partially saturated porous media.

In recent years the interest in SE phenomena has been rising constantly. In 2015 the first book on "the seismoelectric method" was released (Revil, 2015) providing an overview on fundamental concepts of SE theory. A year later Jouniaux and Zyserman (2016) published a review on the "electrokinetically induced seismo-electrics, electro-seismics, and seismo-magnetics for Earth sciences". A second book with the title "Seismoelectric exploration: Theory, experiments and applications" focusing on SE applications is expected to be published in 2020 (personal information).

The advancing number of publications on SE phenomena shows that the interest in the topic is constantly growing. However, as most of the studies target theoretical concepts, reports of field applications are still rare. It is therefore important to shift the focus from numerical investigations of general questions to the actual application of SE measurements in the field.

1.3 Seismoelectric signals generated by earthquakes

Most of the studies mentioned in section 1.2 either explore general questions concerning SE coupling or are aimed at controlled-source SE experiments. However, a coupling between seismic and EM fields can also be observed during passive measurements or in other words ‘during earthquakes’.

Numerous reports of electrical (and magnetical) signals that were recorded during earthquakes exist. These signals show a great similarity to the simultaneously recorded seismic signals (e.g. Johnston, 2006; Huang, 2011; Sun et al., 2019). Over time, geophysicists have offered different explanations for this phenomenon. Among them were the consideration of piezoelectric effects (e.g. Gershenzon et al., 1993; Huang, 2002) or a ‘seismic dynamo effect’ through which the electrical signals are induced by a conductive crust vibrating in the earth’s magnetic field (e.g. Honkura et al., 2000; Matsushima et al., 2013). However, these studies were seldom able to explain all recorded signals or waveforms. Today the theory of electrokinetic coupling is therefore probably the most accepted explanation for the observed signals although a mixture of different effects cannot be excluded.

To better understand the EM signals created during earthquakes a great number of numerical studies have been conducted. Different source types have been simulated such as a double-couple source (Gao and Hu, 2010) or a finite fault (Ren et al., 2010; Hu and Gao, 2011) and the characteristics of different EM wave-types excited during earthquakes have been discussed (Gao et al., 2013; Ren et al., 2015). However most of the numerical models consist only of one or two layers in combination with half-spaces. In contrast to that, Gao et al. (2016) used a model consisting of 9 layers to recalculate the EM waveforms for the MW6.0 Parkfield earthquake. Sun et al. (2019) included a scattering effect into their simulation of a 7-layer model so the resulting waveforms better reflected their observations from a M5.4 earthquake in Japan. These studies show the importance of including realistic subsurface parameters and a sufficient number of layers into simulations if one wants to understand SE signals generated by earthquakes.

While there has been great progress in the understanding of SE signals generated by earthquakes as well as the related synthetic modelling, the analysis of actual field data has been neglected. This thesis can be seen as a first step to close this gap by providing information on the detection, analysis and interpretation of SE data recorded during passive experiments.

1.4 Theory of seismoelectric signals

The effect of SE coupling is explained by Haartsen and Pride (1997) in the following way: When solid grains come into contact with a fluid a so-called electric double layer (EDL) is formed. The EDL consists of ions that are stuck to the surface of the grains and counter-ions that move freely in the pore-fluid, balancing the immobile ions (see Fig. 1.1). When a seismic wave travels through the subsurface the counter-ions in the fluid start moving relatively to the immobile ions on the grains resulting in a ‘streaming current’.

If the passing seismic wave is compressional the mobile counter-ions accumulate in the peaks of the seismic wave and dissipate in the troughs. The resulting unbalance creates an electric field perpendicular to the seismic wavefront leading to a ‘conduction current’. When the conduction and streaming currents equalise themselves the net current becomes zero. This is the reason why only electric and not magnetic fields accompany compressional waves.

In case of seismic shear waves conduction currents are not generated since there is no divergence and therefore no peaks and troughs that can initiate charge separation. The streaming current that is excited by the relative motion between the grains and fluids then results in a magnetic field accompanying the seismic waves. This magnetic field can in turn induce an electric field, although this is expected to be much smaller than the electric field excited by compressional waves.

The electric and magnetic fields described above are bound to their respective seismic counterparts. As they cannot exist without them, they are called ‘coseismic’ waves. Further details on coseismic waves will be given in section 1.5.1.

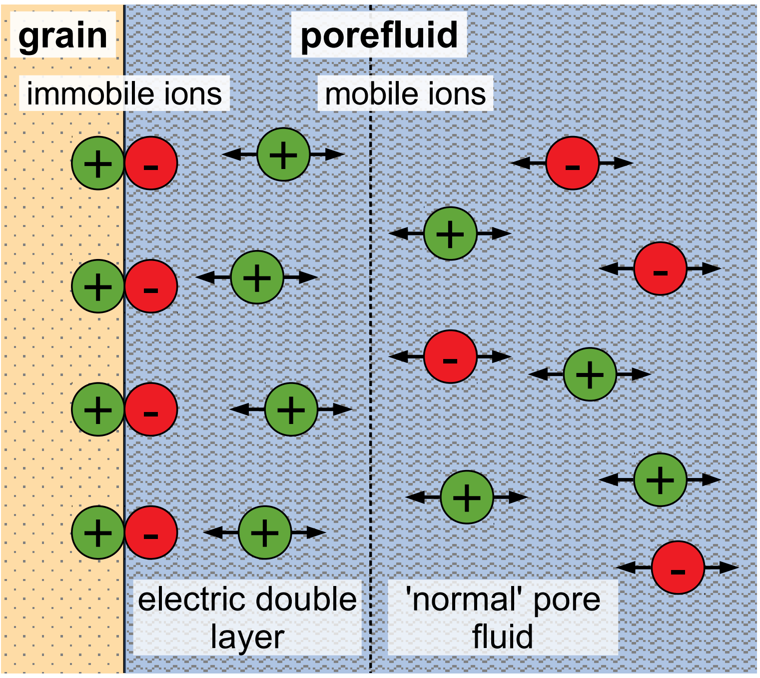

Fig. 1.1: *Sketch of the electric double layer (EDL): The EDL consists of immobile ions stuck on the grains’ surface and mobile counter-ions in the pore fluid. When the mobile ions start moving relatively to the immobile ions due to passing seismic waves a ‘streaming current’ is generated resulting in electric and magnetic fields, depending on the seismic wave-type.*

1.4.1 Governing equations

In 1994 and 1997 Pride and Haartsen and Pride published the following set of governing equations describing the electrokinetic coupling between seismic and electromagnetic waves in an isotropic, fully saturated medium assuming a time dependence of $e^{-i\omega t}$:

$$\nabla \cdot \tau = -\omega^2[\rho\vec{u} + \rho_f\vec{w}] + \vec{F} \tag{1.1}$$

$$\tau = [K_G\nabla \cdot \vec{u} + \mathrm{C}\nabla \cdot \vec{w}]\vec{I} + G[\nabla\vec{u} + \nabla\vec{u}^T - \frac{2}{3}\nabla \cdot \vec{u}\vec{I}] \tag{1.2}$$

$$-P = \mathrm{C}\nabla \cdot \vec{u} + \mathrm{M}\nabla \cdot \vec{w} \tag{1.3}$$

$$-i\omega\vec{w} = \frac{k}{\eta}[-\nabla P + \omega^2\rho_f\vec{u} + \vec{f}] + L\vec{E} \tag{1.4}$$

$$\vec{J} = L[-\nabla P + \omega^2\rho_f\vec{u} + \vec{f}] + \sigma\vec{E} \tag{1.5}$$

$$\nabla \times \vec{E} = i\omega\vec{B} - \vec{M} \tag{1.6}$$

$$\nabla \times \vec{H} = -i\omega\vec{D} + \vec{J} + \vec{C} \tag{1.7}$$

$$\vec{D} = \varepsilon\vec{E} \tag{1.8}$$

$$\vec{B} = \mu\vec{H} \tag{1.9}$$

Equations 1.1 - 1.3 are based on Biot's theory for acoustic propagation in porous media (Biot, 1956, 1962) while equations 1.6 - 1.9 are Maxwell's electromagnetic field equations. Equations 1.4 and 1.5 are called 'dynamic transport equations' and were developed by Pride (1994). They couple the EM wavefields to the mechanical wavefields. Equation 1.5 states, that the macroscopic current density $\vec{J}$ is the sum of the streaming current densities (first term of 1.5) and the average conduction densities (second term of 1.5). The Darcy filtration velocity $-i\omega\vec{w}$ from equation 1.4 can equally be separated into a mechanically fluid flow (first term of 1.4) and a fluid flow caused by the electric field (second term of 1.4).

Equations 1.4 and 1.5 are both connected via the dynamic coupling coefficient $L(\omega)$. If L is zero, the seismic and electric fields are entirely decoupled and no electrical (or magnetical) signal is excited by seismic waves. According to Pride (1994), the coupling coefficient is the product of a static coefficient L_0 as well as a frequency dependent function:

$$L_0 = -\frac{\phi}{\alpha_\infty}\frac{\varepsilon_0\kappa_f|\zeta|}{\eta}\left(1 - 2\frac{\tilde{d}}{\Lambda}\right) \tag{1.10}$$

$$L(\omega) = L_0\left[1 - i\frac{\omega}{\omega_t}\frac{m}{4}\left(1 - 2\frac{\tilde{d}}{\Lambda}\right)^2\left(1 - i^{3/2}\tilde{d}\sqrt{\frac{\omega\rho_f}{\eta}}\right)^2\right]^{-1/2} \tag{1.11}$$

with ω_t being the 'transition frequency'. This frequency, sometimes also known as Biot-frequency, separates the viscous flow at low frequencies from the inertial flow at high frequencies. It is defined as:

$$\omega_t = \frac{\phi\eta}{\alpha_\infty k_0 \rho_f} \tag{1.12}$$

If $\omega_t >> \omega$, the coupling coefficient L becomes frequency independent. This is generally the case for SE applications as for typical subsurface parameters ω_t can be expected to be much larger than 1000 Hz, which is well above the frequency range of typical seismic applications.

Equation 1.10 was developed for fully saturated media. Warden et al. (2013) extended Pride's theory to partially saturated conditions. In that case the static coefficient becomes:

$$L_0(S_w) = -\frac{\phi}{\alpha_\infty}\frac{\varepsilon_w|\zeta|}{\eta}\left(1 - 2\frac{\tilde{d}}{\Lambda}\right)S_w^n S(S_w) \tag{1.13}$$

where $S(S_w)$ is a saturation function. In the modelling code used for this thesis the saturation function from Guichet et al. (2003) is implemented ($S = (S_w - S_{wr})/(1 - S_{wr})$, $S_{wr} = 0.1$ being the 'residual saturation'). However, other saturation functions as for example from Revil et al. (2007) or Allègre et al. (2010) could be considered. For more details on the numerical modelling of SE wave propagation in partially saturated materials and the influence of the different saturation functions see Warden et al. (2013).

1.5 Seismoelectric wave-types

1.5.1 Coseismic waves

As described before, the electrical and magnetical signals excited by electrokinetic coupling are bound to their respective seismic waves and cannot exist independently. Hence, they are known as coseismic waves.

Garambois and Dietrich (2001) developed the following transfer-functions for the coseismic electric and magnetic field:

$$\vec{E} \simeq \frac{1}{\sigma_f}\frac{\varepsilon_0 \rho_f \kappa_f \zeta}{\eta}\left(1 - \frac{\rho}{\rho_f}\frac{\mathrm{C}}{\mathrm{H}}\right)\ddot{\vec{u}} \tag{1.14}$$

$$|\vec{H}| \simeq \frac{\phi}{\alpha_\infty}\frac{\varepsilon_0 \rho_f \kappa_f |\zeta|}{\eta}\sqrt{\frac{G}{\rho}}|\ddot{\vec{u}}| \tag{1.15}$$

While eq. 1.14 is valid for longitudinal P-waves, eq. 1.15 is valid for transverse SH- and SV-waves. Equations 1.14 and 1.15 were developed for fully saturated media. Extensions for un- and partly saturated media have been proposed by Bordes et al. (2015) and Zyserman et al. (2016).

The transfer-functions show that the electric field is proportional to the seismic acceleration $\ddot{\vec{u}}$ and sensitive to the fluid's electric conductivity σ_f. Meanwhile the magnetic field is proportional to seismic velocity $\dot{\vec{u}}$ and sensitive to the porosity ϕ. As the coseismic signals are directly connected to the seismic amplitudes, they only provide information limited to the immediate vicinity of the recording station. Information from deeper layers cannot be retrieved.

Coseismic electric fields have successfully been recorded during active as well as passive field measurements (e.g. Strahser et al., 2011; Matsushima et al., 2002). During the investigation of the field records a distinct S-phases can often be identified in the data, even though the electric field should only accompany compressional waves. As illustrated in Fig. 1.2, this apparent contradiction can easily be resolved, considering that SE signals also accompany S-to-P converted waves, which are generated at the earths surface as well as at the numerous interfaces in the subsurface.

Reports of recorded coseismic magnetic fields exist as well (e.g. Matsushima et al., 2002). Unfortunately, it is extremely difficult to distinguish between the actual coseismic magnetic field and artificial induction signals caused by the movement of the recording stations. Reports of observed coseismic magnetic signals are therefore usually treated with caution. Bordes et al. (2008) were able to record magnetic coseismic signals in the Low Noise Underground Laboratory of Rustrel (France) during a precisely designed experiment, carefully excluding any magnetic signals caused by induction. The accurate setup of the experiment demonstrates how hard it would be to record the magnetic signals in the field without artificial interference. Because of these challenges this thesis will only focus on the electrical signals as many other studies do as well.

1.5.2 Interface responses

Beside coseismic waves a second type of SE signals exists, commonly known as an interface response (IR). The term 'converted signals', which can be found especially in older publications, describes the same wave-type.

As the name 'Interface Response' suggests, IRs are excited when the (co)seismic waves cross an interface. Differing electric or poroelastic parameters on either side of the boundary lead to a charge separation, which then acts as a source for a new EM field. As the resulting EM wave is not bound to a seismic wave anymore, it usually propagates at a significantly larger speed than the (co)seismic waves and can therefore be observed before them (see Fig. 1.2).

A sensitivity study of Garambois and Dietrich (2002) showed that IRs respond to changes of rock- porosity and -permeability as well as the salinity and viscosity of the pore fluids. Furthermore IRs can contain information from deeper layers, because - contrary to coseismic waves, which only provide information about the direct vicinity of the recording stations (see section 1.5.1) - they are not directly bound to the seismic field. Hence, IRs are usually the prime target of SE investigations.

In recent years scientists started to distinguish between two different IR types: radiant and evanescent IRs. Radiant IRs (rIRs) are only excited at very small incident angles, meaning 'vertically above the source'. However, due to their fast velocities they seemingly appear on all traces of a SE shot-gather simultaneously. Contrary to that, evanescent IRs (eIRs) are generated at larger offsets. They therefore have a moveout similar to that of the seismic waves, which is why they are also known as quasi-coseismic signals (Ren et al., 2015; Butler et al., 2018). Detailed information on eIRs and rIRs is provided in chapter 4.

1.5.3 Seismoelectric signals from the source

Besides coseismic signals and IRs a third type of EM wave is generated during an earthquake. This EM wave is related to the nucleation processes and should be recorded immediatly after the origin time of the earthquake. As the amplitudes of these signals are expected to be comparably small, their detection is rather unlikely (Gao et al., 2013). Hence, they will not be discussed in this thesis.

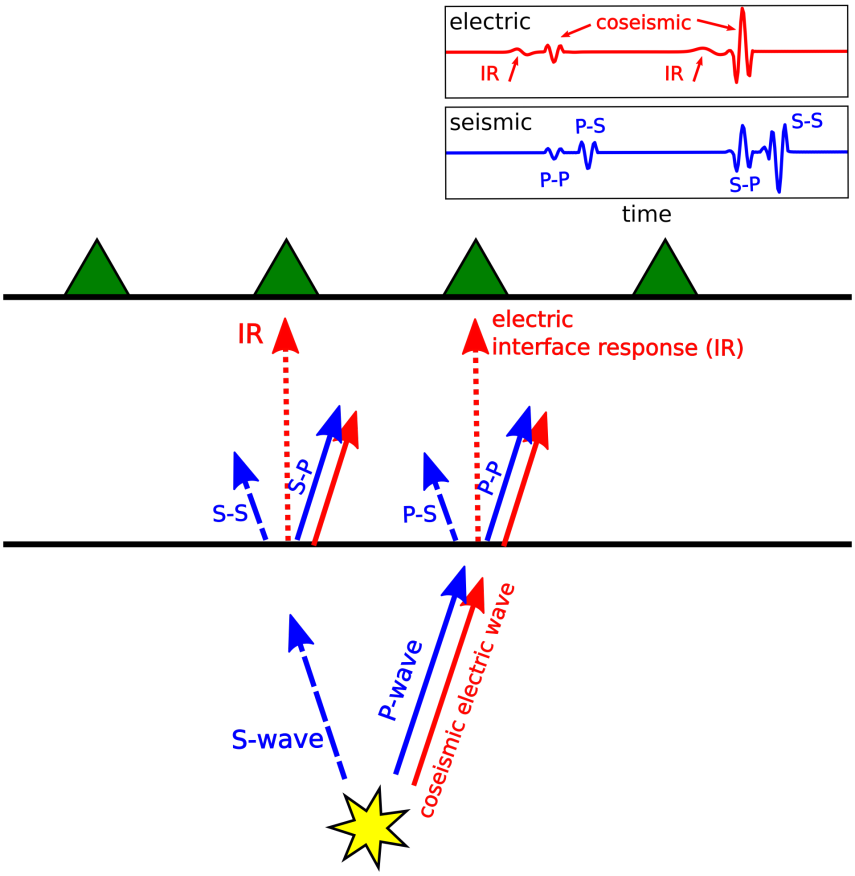

Fig. 1.2: *Schematic overview on SE signals observed during earthquakes. Coseismic signals accompany P-waves and are proportional to the seismic acceleration. IRs are excited at interfaces and reach the surface faster than their coseismic counterparts.*

1.6 Thesis outline

The goal of this thesis is to broaden the knowledge about SE signals generated by earthquakes by focusing on detection, analysis and interpretation scenarios. The actual value of passive SE field experiments can of course only be assessed by conducting and evaluating SE measurements. However, the investigation of previously gathered data as well as numerical calculations can help to determine under which circumstances these experiments will most likely be successful. One hope for this thesis therefore is that it helps to pave the way for future passive SE field experiments.

The main body of this thesis consists of three scientific papers that investigate SE signals generated by earthquakes. In the first paper (chapter 2) we established logarithmic distance-magnitude thresholds to investigate at which hypocentral distances SE signals can be expected to be observed if they were generated by an earthquakes with a distinct magnitude. We then compared SE signals from various earthquakes recorded at different locations in the Atacama Desert (Northern Chile) to detect site-specific behaviour. We recognised this site-dependency with SE spectral ratios (SESRs) - which were introduced by us - as well as envelope-analysis. This supports our assumption that SE signals can be used to study the local subsurface.

In the second paper (chapter 3) the concept of SESRs is explored as a new analysing tool with which the the influence of the IRs on the SE signal can be evaluated. Field data from the Pisagua-Iquique earthquake sequence is compared to modelling results, showing that SESRs can probably be used to study the local subsurface in up to a few hundred meters.

In the last paper (chapter 4) the analysis of SE earthquake signals is concluded with the numerical investigation of the SE response to a multi-layered subsurface model. The study was conducted to evaluate the possibility of gaining information from a passive SE field experiment with local upper crustal seismicity. It was shown that the chances to identify single IRs in a SE wavetrain is highest if the records are obtained close to the epicenter of the earthquake generating the signals. Furthermore it was established that both - SESRs as well as envelope-analysis - can be used to detect porosity and salinity changes in the upper subsurface. Nevertheless, local noise levels and small amplitudes remain a challenge.

In the last chapter (chapter 5) of this thesis the main results of the three studies are summarised by answering the following questions: 1) Under which conditions can SE signals from earthquakes best be detected? 2) How can SE signals from earthquakes be analysed? 3) How can SE signals from earthquakes be interpreted?

The answers show that coseismic signals can be observed over 400 km away from the earthquake source, depending on magnitude, whereas information from IRs are best analysed if recorded in close vicinity to the earthquakes' epicenters. SESRs and envelope-analysis can be used to obtain site-dependent subsurface information without having to focus on single IR amplitudes. In general, the SE signals show a sensitive behaviour towards changes of subsurface porosity and the salinity of the pore-fluid. Nevertheless, the distinction between the effects of the different varying parameter might be difficult. Before drawing the final conclusion, it is suggested in an outlook on possible future investigations, to conduct passive SE field experiments as soon as possible, as this is the inevitable next step to understand SE signals generated by earthquakes.

1.6.1 Authors contribution

The introduction and conclusion of this thesis (chapters 1 and 5) were written by me (Laura Dzieran). I provided the manuscripts for the three scientific papers (chapters 2 to 4), created all figures and conducted the analyses with contributions from Wolfgang Rabbel and Martin Thorwart. Oliver Ritter and Jaime Araya Vargas provided and helped understanding the SE field data recorded in Northern Chile (chapters 2 and 3).

1.7 Glossary

α_∞	tortuosity
$\vec{B}$	magnetic flux density
$\vec{C}$	an applied current-density source
C	C, H, M are coefficients from Biot (1962), related to bulk moduli of the fluid and solid phases
$\tilde{d}$	length $\tilde{d} \leq d$, d is the Debye length, related to the thickness of the EDL
$\vec{D}$	dielectric displacement
η	pore fluid viscosity
ε	electric permittivity
ε_0	electric permittivity of the vacuum
ε_w	electric permittivity of the water
$\vec{E}$	electric field
$\vec{f}$	an applied body-force acting on the fluid-phases
$\vec{F}$	an applied body-force acting on the bulk material
G	stiffness or shear modulus of the framework of grains
H	C, H, M are coefficients from Biot (1962), related to bulk moduli of the fluid and solid phases
$\vec{H}$	magnetic field
$\vec{I}$	identity matrix
$\vec{J}$	electric current density
k	dynamic permeability
k_0	static permeability
κ_f	fluid's dielectric permittivity
K_G	Gassmann's bulk modulus
L	dynamic electrokinetic coupling coefficient
L_0	static electrokinetic coupling coefficient
Λ	geometric pore parameter
m	geometric parameter; $m = \phi\Lambda^2/(\alpha_\infty k_0)$, usually between 4 and 8
M	C, H, M are coefficients from Biot (1962), related to bulk moduli of the fluid and solid phases
$\vec{M}$	an applied magnetic-current source
μ	magnetic permeability
n	Archie exponent
ω	radial frequency
ω_t	transition frequency, separating low frequency viscous flow from high frequency inertial flow
P	pore fluid pressure
ϕ	porosity
ρ	bulk density
ρ_f	pore fluid density
S_w	saturation

S_{wr}	residual saturation
σ	electric conductivity
σ_f	fluid's electric conductivity
τ	bulk-stress tensor
$\vec{u}$	average displacement of the solid grains
$\ddot{\vec{u}}$	seismic velocity
$\ddot{\vec{u}}$	seismic acceleration
$\vec{w}$	average relative fluid-solid displacement multiplied by porosity
ζ	zeta-potential

2 Seismoelectric ground response to local and regional earthquakes

This chapter is based on the paper 'Seismoelectric ground response to local and regional earthquakes' accepted for publishing in the book 'Seismoelectric exploration: Theory, experiments and applications' by the editors N. Grobbe, A. Revil, Z. Zhu and E. Slob.
Citation: Dzieran, L., W. Rabbel, M. Thorwart, and O. Ritter, 2020: 'Seismoelectric ground response to local and regional earthquakes'. Seismoelectric exploration: Theory, experiments and applications, N. Grobbe, A. Revil, Z. Zhu, and E. Slob, Eds., Wiley OnlineLibrary, in press.

Abstract We analyze the seismoelectric (SE) ground response to seismic waves radiated from local earthquakes and its dependency on magnitude and recording location. We establish a magnitude-distance relationship describing the magnitude threshold to be exceeded for observing SE signals with standard magnetotelluric stations. Based on 16,341 events we found that 67% of earthquakes with magnitude $\mathrm{M} \geq 2.3 \cdot \log_{10}(\mathrm{r/km})$ at hypocentral distance *r* showed clear SE signals if the noise level is below 0.1 µV/m. The logarithmic term results from geometric spreading. A comparison of records from different earthquakes and stations shows that both the magnitude and the geology at the receiver site influence the observability of SE arrivals. The site effect is frequency dependent. To quantify this, we computed seismoelectric spectral ratios (SESRs) defined as the ratio of the amplitude spectra of SE records and acceleration seismograms. Some stations show almost constant SESRs in the main frequency range indicating that the response is mainly composed of coseismic SE signals. Others show consistently a decrease of SESRs with increasing frequency suggesting interference of coseismic and interface response arrivals. The transfer function of SE to seismic amplitudes is of the order of values for dry sand found in previous studies.

2.1 Introduction

The seismo-electromagnetic effect has been explored in numerous near surface studies (e.g. Thompson and Gist, 1993; Garambois and Dietrich, 2001; Thompson et al., 2007; Strahser et al., 2007, 2011). However, the coupling between seismic and electric signals can also be observed during earthquakes (e.g. Honkura et al., 2000; Matsushima et al., 2002; Huang, 2011; Gao et al., 2016).
In this chapter we investigate seismoelectric (SE) signals caused by regional and local

earthquakes using seismic and magnetotelluric (MT) field data mainly from the subduction zones of Central and South America. We focus on the following two main questions: First, which is the minimum earthquake magnitude required for observing SE fields at a given hypocentral distance with standard state-of-art seismic and MT field equipment under low to moderate noise conditions? Second, how do site effects influence SE signals? We answer the first question statistically by analyzing datasets from Costa Rica, Chile and Norway. We establish a threshold magnitude-distance-relationship which can be used as a guideline to whether or not SE effects might be observable. The second question is approached by comparing SE signals from the 2014 Pisagua (Iquique) earthquake recorded at different epicentral distances by seismic and MT stations in northern Chile and by comparing the site responses of selected stations for different magnitude earthquakes. The chapter is organized in the following way: The applied instrumentation and analyzed data sets are described in section 2.2. We then determine threshold magnitude-distance relationships for the observation of SE signals in section 2.3. In section 2.4 SE site effects are evaluated.

2.2 Instrumentation and field data

Our study of the magnitude-distance-relationship (section 2.3) is based on MT field data from stations in Costa Rica, Chile and Norway.
The Costa Rica station ZOM was deployed on the Nicoya Peninsula from May to November 2010 as well as February to June 2011. With the help of the ISC catalog (International Seismological Centre, 2015) we identified 203 earthquakes with ML > 1.9 within 5° epicentral distance.
In northern Chile we used recordings from stations PB02, PB09 and PB15 from the CX network of the Integrated Plate boundary Observatory Chile (IPOC), located in the Atacama Desert (GFZ & CNRS-INSU, 2006; Vargas and Ritter, 2015). 16,126 earthquakes with ML > 1.2 occurred within a 5° radius around 69.5° West and 22° South in the year 2014, including the MW8.1 Pisagua earthquake that took place in the night of April 1, 2014 (Cesca et al., 2016) and its aftershocks.
The magnitude-distance analysis also includes two small magnitude earthquakes from Norway (courtesy of Geological Survey of Norway (NGU)). These events occurred on July 30 and August 1, 2015 in northern Norway and were coincidentally registered by two short-term arrays of MT-stations which consisted of six stations each and were deployed by a field campaign from NGU. Array 1 recorded the event on July, 30 and Array 2 the event on August,1.
The analyzed events as well as the location of the stations can be seen in Fig. 2.1. Tab. 2.1 lists the location, average noise level and electrode distance of the individual stations.
For the analysis of the SE site effects (section 2.4) we used recordings of the MW8.1 Pisagua earthquake from April 1, 2014 and two of its largest aftershocks. Additionally to the data from stations PB02, PB09 and PB15 of the CX network, we included data from stations PB01, PB03, PB06 and PB07 of the same network. The electric data were complemented with seismic data recorded at the same location. Information about the stations

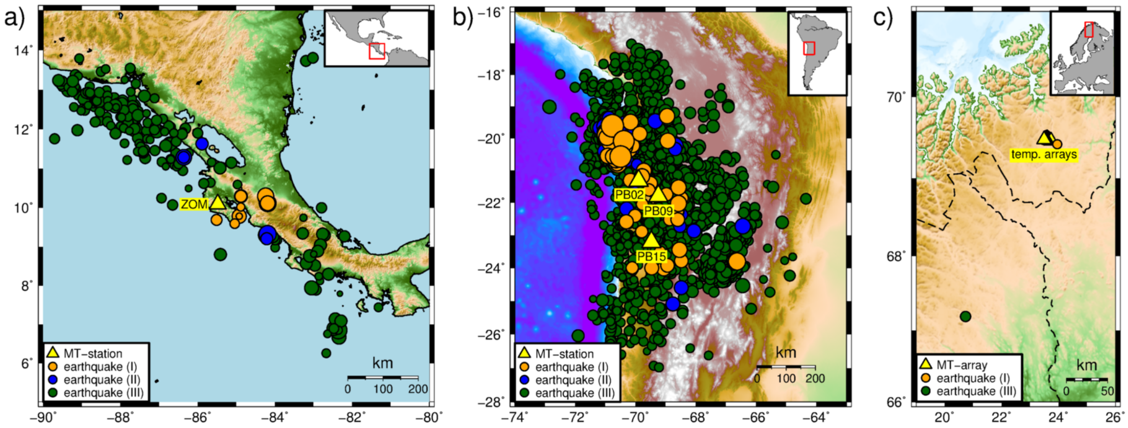

Fig. 2.1: *Maps of earthquake epicenters from the ISC catalog and recording stations in (a) Costa Rica, (b) Chile and (c) Norway used for the magnitude-distance analysis in this study (section 2.3). The epicenters are color-coded according to their category. Category I includes earthquakes where P-and S-phases could be clearly distinguished in the SE data. Category II holds earthquakes where only large SE amplitudes could be identified. For earthquakes in category III no SE signals could be found.*

can be found in Tab. 2.1. The locations and magnitudes of the earthquakes are listed in Tab. 2.2 and plotted in Fig. 2.2. Backazimuths as well as epicentral distances between the stations and the earthquakes are listed in Tab. 2.3.
All electric signals in this study were gathered via MT-stations equipped with non-polarizable Ag-AgCl-electrodes. In Costa Rica and Chile the signals were digitized with a sampling rate of 20 Hz and stored by 24-bit EarthData loggers. The seismic data used in section 2.4 were also sampled with a rate of 20 Hz, recorded by FBA-EST accelerometers. The instruments were provided by the Geophysical Instrument Pool Potsdam. The events in Norway were registered by the NGU with a sampling rate of 500 or 512 Hz.

2.3 Threshold magnitude-distance relationship

For determining the minimum magnitude required for the observation of SE fields on MT stations we restricted our analysis to earthquakes within 5° epicentral distance with M_W or M_L magnitudes specified in the ISC catalog (section 2.2). Based on this information, we inspected the electric data in the respective time windows to investigate at which level SE earthquake signals exceeded the background noise level. We applied a restitution filter to eliminate the instrument response and a bandpass filter between 0.1 Hz and 5 Hz. The strengths of the magnitudes were provided by the ISC catalog. For each earthquake an individual noise level was determined by calculating the standard deviation of the amplitude distribution of the electric field data recorded on a station in the three minutes before the event. The average noise level for each station is listed in Tab. 2.1. It differs between 0.1 μV/m and 2.6 μV/m.
For evaluation we divided the SE signals into three categories: Category I includes all

	station	latitude	longitude	noise level	electrode distance (NS/EW)
Costa Rica	ZOM	10.09°	-85.481°	1.0 µV/m	60.0 m / 60.0 m
Chile	PB01	-21.0432°	-69.4874°	0.2 µV/m	81.4 m / 80.3 m
Chile	PB02	-21.3197°	-69.8960°	1.0 µV/m	84.8 m / 80.9 m
Chile	PB03	-22.0485°	-69.7531°	2.0 µV/m	71.5 m / 80.4 m
Chile	PB06	-22.7058°	-69.5719°	1.5 µV/m	80.8 m / 79.3 m
Chile	PB07	-21.7267°	-69.8862°	2.0 µV/m	80.5 m / 81.3 m
Chile	PB09	-21.7964°	-69.2419°	0.1 µV/m	80.0 m / 80.8 m
Chile	PB15	-23.2083°	-69.4709°	0.2 µV/m	80.7 m / 80.8 m
Norway	Array 1	23.6405°	69.4823°	2.6 µV/m	62.0 m / 62.0 m
Norway	Array 2	23.5603°	69.4816°	0.1 µV/m	64.3 m / 66.2 m

Tab. 2.1: *Attributes of recording stations in Costa Rica, Chile and Norway.*

	time	latitude	longitude	depth	magnitude
EQ 1	2014-04-01 23:46:48.20	-19.6100°	-70.7690°	25 km	8.1
EQ 2	2014-04-03 02:43:12.71	-20.571°	-70.493°	22.4 km	7.6
EQ 3	2014-04-03 01:58:27.96	-20.311°	-70.576°	24.1 km	6.5

Tab. 2.2: *Attributes of the M_W8.1 Pisagua earthquake from April 1, 2014 and two of its largest aftershocks used for the SE site effect analysis in section 4.*

	PB01	PB02	PB03	PB06	PB07	PB09	PB15
EQ 1							
backazimuth	320°	334°	338°	340°	338°	326°	341°
epicentral dist.	208 km	211 km	290 km	365 km	252 km	290 km	420 km
EQ 2							
backazimuth	296°	323°	335°	338°	334°	316°	340°
epicentral dist.	117 km	104 km	181 km	255 km	143 km	188 km	311 km
EQ 3							
backazimuth	305°	328°	336°	338°	335°	320°	340°
epicentral dist.	139 km	132 km	211 km	285 km	172 km	215 km	341 km

Tab. 2.3: *Epicentral distances and backazimuths between the M_W8.1 Pisagua earthquake from April 1, 2014 and two of its largest aftershocks (Tab. 2.2) to stations from the CX network (IPOC) in Chile (Tab. 2.1).*

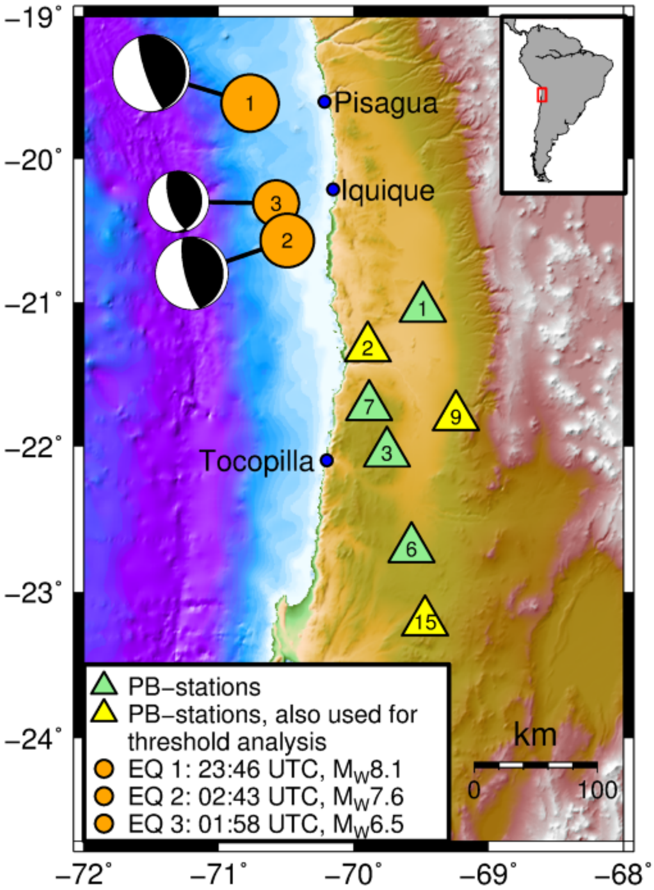

Fig. 2.2: *Location map of the CX network of the Integrated Plate boundary Observatory Chile (IPOC) in northern Chile and the location of the 2014 Pisagua earthquake (EQ1) and two aftershocks (EQ2 & EQ3). The recordings of the earthquakes were used for the analysis of the SE site effects (section 2.4).*

earthquakes where the SE earthquake signals could be clearly identified with distinguishable P- and S-phases. Category II holds earthquakes where only parts of the seismic wave train can be recognized, usually large amplitude S-waves and coda. Earthquakes not recognizable on the electric records were classified as category III.
Overall 16,341 earthquakes were classified in this study. Fig. 2.1 shows the location of the analyzed earthquakes and the stations at which they were recorded. The epicenters are color-coded according to their category (orange = I, blue = II, green = III).
Of the 203 earthquakes recorded in Costa Rica (Fig. 2.1a) only 11 events (5%) fall into category I, and 6 (3%) into category II. The remaining 186 earthquakes (92%) could not be observed in the electric field time series and were classified as category III.
The majority of the earthquakes in this study occurred in Chile (Fig. 1b). Of the 16,126 events 65 (0.4%) fall into category I and 131 into category II. The 15,930 remaining earthquakes (99%) were not identifiable in the electric field data and thus attributed category III.
From the two events in Norway, the one closer to the temporary MT arrays (hypocentral

distance < 20 km) was classified as category I and the other event (hypocentral distance $\sim$ 280 km) as category III.

The classification shows that only a small percentage of the recorded earthquakes can be observed in the electric signals. Due to the areal distribution of these events (Fig. 2.1) the assumption can be made that earthquakes occurring closer to the recording stations are more likely to be fully observable. Additionally, the earthquakes in category I seem to represent larger magnitude events.

When trying to establish a magnitude-distance relationship for visible SE signals from earthquakes, one has to consider the noise conditions of the recording stations. Fig. 2.3a) shows that the number of earthquakes analyzed in this study decreases when the maximum allowed noise limit is lowered. However, when lowering the noise limit from 10 to 0.1 µV/m, 55% of the earthquakes in category III are eliminated from consideration, while in category II and I only 15% and 32% are excluded, respectively.

Fig. 2.3b) and 2.3c) show the events' magnitudes in relation to their hypocentral distances. While Fig. 2.3b) includes all events with a noise level < 10 µV/m, the limit in Fig. 2.3c) corresponds to 0.1 µV/m. The events' categories are again color-coded and show a clear distribution pattern.

Coseismic SE amplitudes are proportional and therefore linked to seismic ground acceleration. Hence, we assume that the threshold magnitudes separating the domains of the SE categories depend mainly on the initial seismic amplitude and geometric spreading just as seismic amplitudes do. As magnitude is proportional to the logarithm of seismic energy and, respectively, displacement or acceleration, the magnitude-distance relationship in question will be logarithmic, too.

For these reasons we applied an approach of the form $M = c \cdot log_{10}(r)$ for defining the SE detection swell, where M is a threshold magnitude, r is the hypocentral distance in km and c is a constant. Adjusting constant c, we define three thresholds for the events in Fig. 2.3b) and c):

$$M1 = 2.7 \cdot log_{10}(r) \tag{2.1}$$

$$M2 = 2.1 \cdot log_{10}(r) \tag{2.2}$$

$$M3 = 2.3 \cdot log_{10}(r) \tag{2.3}$$

Thresholds $M1$ and $M2$ apply to earthquakes recorded at a noise level lower than 10 µV/m. These thresholds (Fig. 2.3b) were chosen in such a way that for $M1$ 67% (or 2/3) of all earthquakes above this threshold are either in category I or II. This means that SE signals are identifiable with a chance of 67% for earthquakes with magnitude $\geq$ M1 at hypocentral distances $\leq r$. Threshold $M2$ corresponds to an identification chance of 33% (or 1/3). Threshold $M3$ applies to earthquakes recorded at a noise level lower than 0.1 µV/m (Fig. 2.3c). $M3$ was defined such that 67% of the earthquakes above this threshold are classified as category I. This means that if the noise level is below 0.1 µV/m, events of magnitude M > 4, 5, 6 have a chance of 67% to produce fully observable SE signals at hypocentral distances r < 50, 150, 400 km, respectively.

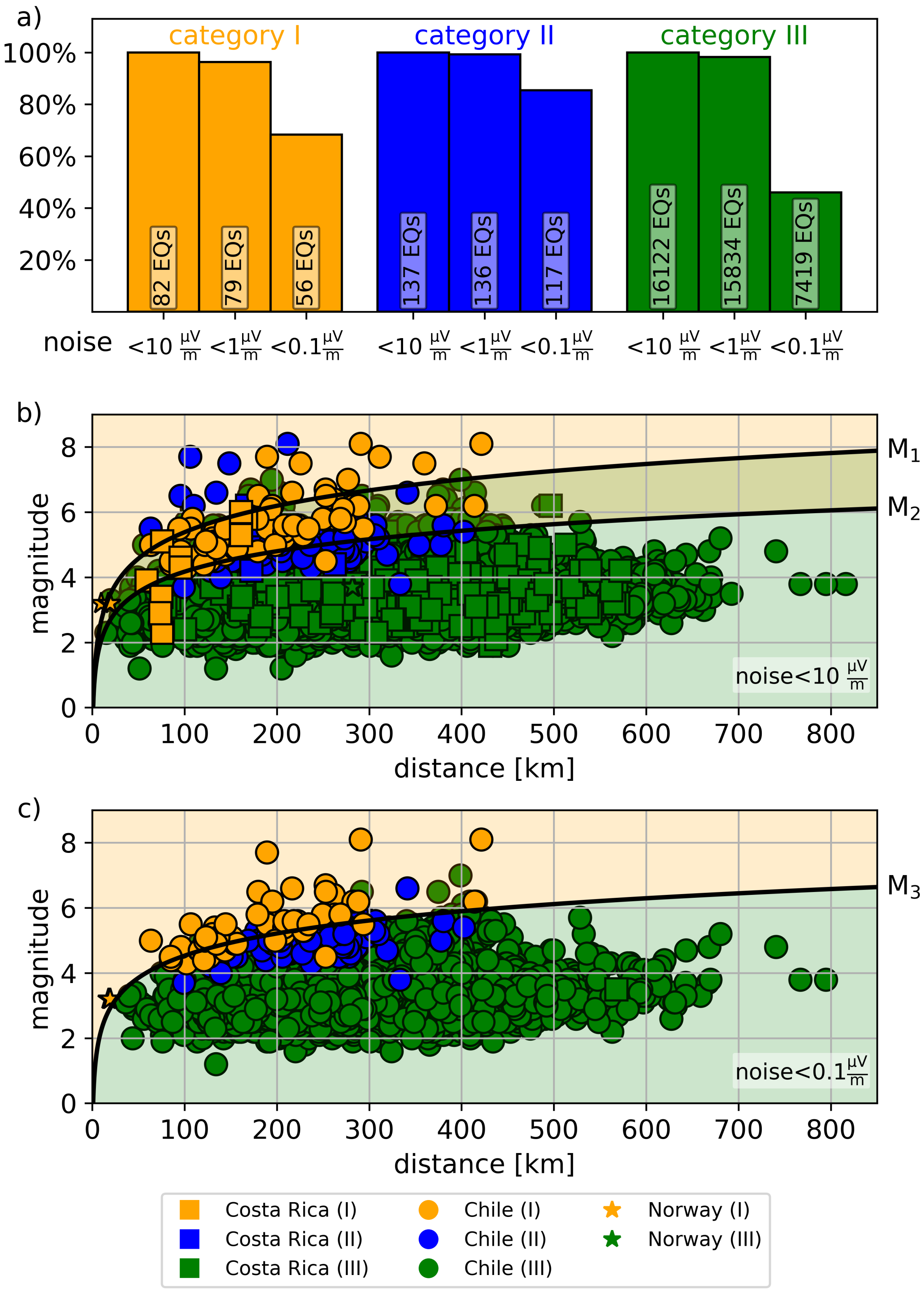

Fig. 2.3: *a) number of earthquakes in different categories for three noise limits. Categories I, II, III (orange, blue, green) correspond to observable, partly observable and non-observable SE signals. b) Magnitude-hypocentral distance diagram for earthquakes from Costa Rica, Chile and Norway with a noise level < 10 µV/m (Fig. 2.1).* $M1$ *and* $M2$ *are threshold magnitude-distance functions according to equations 2.1 and 2.2. Above* $M1$ *the chance to observe an earthquake of category I or II is 67%, above M2 the chance is 33%. c) Magnitude-hypocentral distance diagram for earthquakes from Costa Rica, Chile and Norway with a noise level < 0.1 µV/m. M3 is a threshold magnitude-distance function according to equation 2.3. Above M3 the chance to observe SE signals of an earthquake of category I is 67%.*

2.4 Seismoelectric site effects

In this section we investigate SE site effects using the IPOC data set from northern Chile. In a first step we compare SE signals from one earthquake recorded at different stations, in a second step we compare signals from different earthquakes recorded at two selected stations.

2.4.1 Spatial variation of SE signals

For step one we selected the M_W8.1 Pisagua 2014 earthquake, which took place on April 1, 2014 at 23:46:48.2 UTC, breaking the central fraction of the so called northern Chile seismic gap (Schurr et al., 2014) (EQ1 in Tab. 2.2). The recording stations line up through the Atacama Desert (Fig. 2.2). Station PB01 is closest to the epicenter while station PB15 is furthest away (Tab. 2.3).

The following steps of data processing and analysis were applied to compare the seismic and SE records:

1. Despiking: Some of the electric field records were contaminated with spike-type signals occurring irregularly in time. For despiking two different approaches were applied. Some records showed spike-type signals of a specific shape. In these cases, the time function of these signals was determined from parts of the time series that contained no earthquake signal and then rescaled and subtracted from where it occurred in the earthquake record. Where this was not possible we reduced the spikes by applying a smoothing filter of 50 samples window length. Within this window the median absolute amplitude was calculated and each sample whose amplitude exceeded eight times this mean value was reset to this mean value.

2. Correction for instrument response and high-pass filter (Havskov and Ottemoller, 2010): The instrument response was eliminated for the SE and seismic time series. Then seismic and electric signals were filtered with a 0.2 Hz high-pass to suppress low frequency undulations.

3. Coordinate system: The coordinate system of the sensors was rotated from north-east orientation into radial and transversal components where ‘radial’ corresponds to the back-azimuth (Tab. 2.3). In case of subhorizontal layering this step would lead to a separation of P-SV waves and SH-waves and possibly related SE fields onto the radial and transverse components (e.g. Bormann et al., 2002).

4. Envelope analysis: For comparing the strength of seismic and SE amplitudes we computed scaling factors for each site based on envelope functions (e.g. Taner et al., 1979). The envelopes of the traces were calculated via Hilbert transform and smoothed with a moving-average filter. Then the scaling factor was determined by linear regression between SE and seismic envelope functions. For displaying the envelopes, the intercept value of the regression line was subtracted from the electric field envelope and the result rescaled by the slope factor.

5. Seismoelectric spectral ratios (SESRs): For quantifying the SE site response with respect to the incoming seismic field we computed the ratio of the spectra of the SE and

seismic earthquake signals.
Seismic and coseismic electric signals originate from the same source mechanisms, meaning that calculating their spectral ratio eliminates the influence of the source function. Both seismic acceleration $\ddot{U}(t)$ and SE records $E(t)$, can be understood as the convolution of the respective Green's functions $G\ddot{U}(t)$ and $GE(t)$ with the same source-time function $S(t)$ in the time domain. This corresponds to a multiplication of the respective spectra in the frequency domain:

$$\begin{aligned} \ddot{U}(\omega) &= G\ddot{U}(\omega) \cdot SF(\omega) \qquad (2.4) \\ E(\omega) &= GE(\omega) \cdot SF(\omega) \qquad (2.5) \end{aligned}$$

Therefore, the ratio of seismic and SE frequency spectra creates a function that is basically the spectral ratio of the SE and seismic Green's functions. We call this function SESR (SeismoElectric Spectral Ratio):

$$SESR(\omega) = \frac{E(\omega)}{\ddot{U}(\omega)} = \frac{GE(\omega)}{G\ddot{U}(\omega)} \qquad (2.6)$$

Hence, the analysis of spectral trends in the SESR is indicative of the mechanism causing the SE signals.

Figs 2.4 and 2.5 show the results of the analysis for the radial (r) and transverse (t) components of the seven stations. The stations are sorted according to their distance to the earthquakes epicenter.
Columns a) and b) in Figs 2.4 and 2.5 show the time series of the electric field and corresponding seismic ground acceleration at the same amplitude scale from origin time to 210 seconds travel time. The earthquake signals are clearly identifiable on all traces despite varying noise levels. In the records of stations PB01 and PB02, which are closest to the epicenter, a first aftershock is visible at the end of the traces. Except for stations PB09 and PB15, the amplitudes of the seismic signals decrease with increasing epicentral distance as expected. The deviations from this trend are an expression of the seismic site effect. The electric traces show a similar trend, but the deviations from it occur at different stations. This indicates that SE and seismic site effects are not strictly correlated.
The relation of SE and seismic signal strengths is quantified in terms of scaling factors (s) listed in columns c) of Figs 2.4 and 2.5 and plotted in Fig. 2.6. The Figs of column c) show smoothed envelope time functions of the SE and ground acceleration traces E and Ü, that are found in columns a) and b). For comparison, the scaling factor was applied (see processing item 4 above). The envelopes of E and Ü agree generally well in shape. According to Garambois and Dietrich (2001) the coseismic electric signals should be proportional to the seismic acceleration of compressional waves. The similarity of the envelopes of the E and Ü fields confirms this prediction in general. However, more subtle deviations from this trend become visible through the SESRs shown in columns d) (processing item 5).
The SESRs (Figs 2.4 and 2.5 d) show mainly two frequency trends: They are either flat

(PB02, PB07, PB15) or decrease with increasing frequency (PB01, PB09, PB03, PB06). Flat SESR functions indicate that the major part of the SE signal is directly proportional to the seismic signal. They can therefore be explained by coseismic SE arrivals according to the relation derived by Garambois and Dietrich (2001). A frequency dependence of the SESRs can have two possible explanations: either the physical and hydraulic parameters steering the E-Ü relation of the coseismic signals are indeed frequency dependent, or IR signals contribute significantly to the SE ground response function. IR signals can be expected to be frequency dependent because they are affected by frequency dependent electromagnetic absorption, which differs from seismic absorption and can therefore not be compensated by forming a spectral ratio.
The scaling factor calculated in processing item 4 represents the station-specific value of d|E|/d|Ü|, averaged over all frequencies. It shows a strong dependence on station location but not on epicentral distance (Fig. 2.6). It varies between 5 and $\sim$ 40 µVs^2/m^2 for the radial components and 5 and $\sim$ 120 µVs^2/m^2 for the transverse components. The average scaling factor over all stations is $\sim$ 20 µVs^2/m^2 for radial and $\sim$ 40 µVs^2/m^2 for transversal components with a spatial variation of approximately $\pm$100%. The scaling factors of r- and t-components show the same pattern of spatial variation. The lowest scaling factors are found at stations with a flat SESR (PB02, PB07 and PB15).
As mentioned in processing item 3 the rotation of the coordinate system was applied to separate P-SV-waves on the radial from SH-waves on the transversal component. This should result in different magnitudes of the SE signals and of the scaling factors on the r- and t-component, too, because coseismic signals are caused by compressional wave portions only (Garambois and Dietrich, 2001). Unexpectedly, we found that radial and transverse components are of the same order of magnitude both in signal strength and scaling factors. For 1D or 2D media we would expect to find P-SV- waves and related SE-waves polarized only in the vertical plane, oriented in backazimuth direction (radial direction). The transverse sensor (horizontal component, orthogonal to the backazimuth) may show SH-waves but no SE arrivals. SE energy can be observed on transverse components only if the corresponding rays arrive from directions horizontally oblique to the backazimuth. Therefore, the observation of SE energy on the transverse component indicates that the assumption of a 1D or 2D medium is an oversimplification and that the subsurface structure is essentially 3D such that intense 3D scattering can occur.
As an intermediate summary we can state that stations show differences in the SE responses, which are not correlated with epicentral distance. These differences concern SE signal strength, scaling factors and frequency trends of the SESR, which do not show any epicentral systematic. In the next step we test if these characteristics can indeed be regarded as site specific effects by comparing if the SESRs remain similar for different earthquake source functions.

2.4.2 Site-specific SE ground response

In the last section we showed that the SE signals from one selected earthquake do reveal different characteristics at different stations. To verify whether or not these characteristics can be considered as site-specific effects we compare SE signals from different

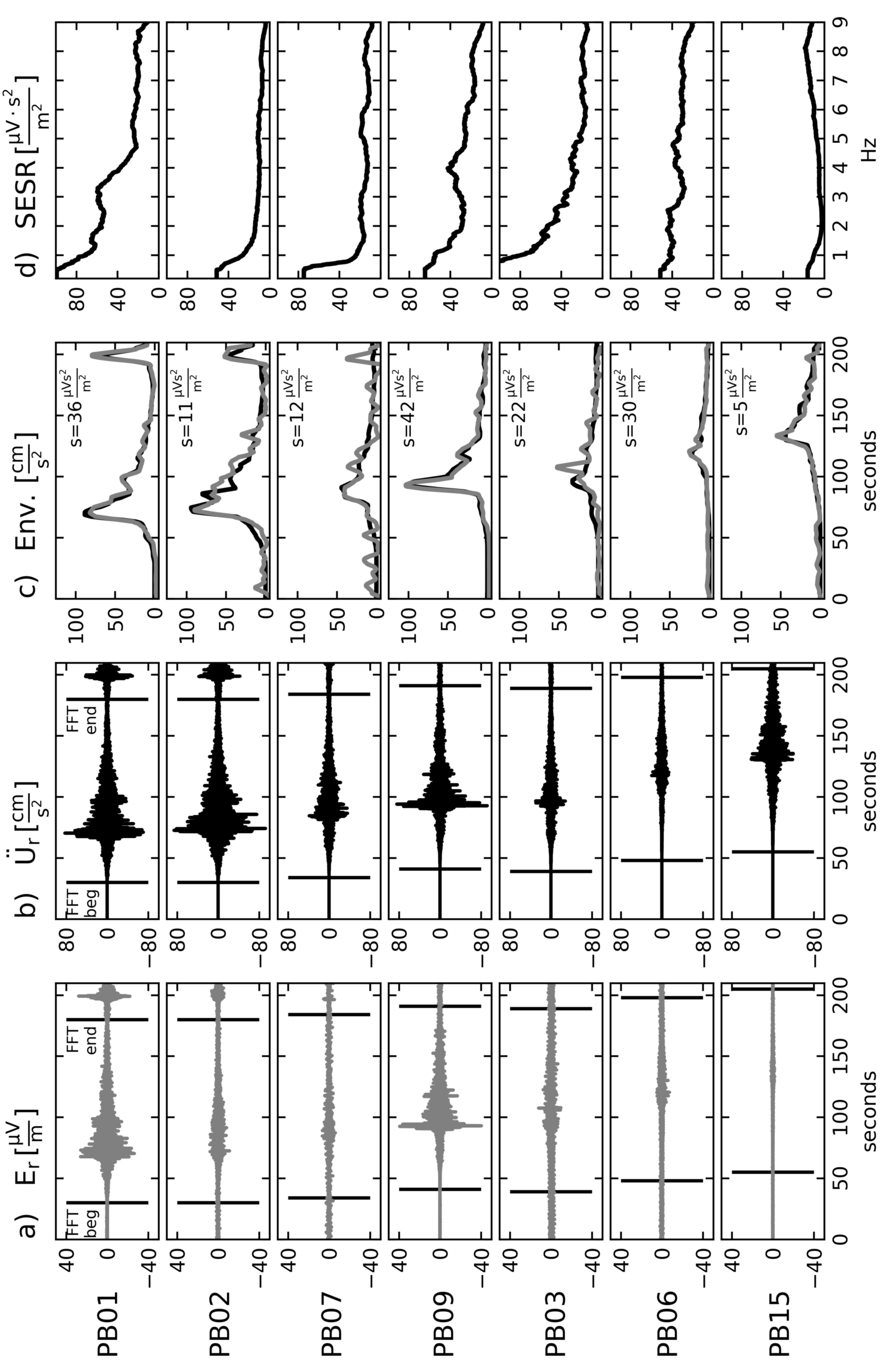

Fig. 2.4: *Radial components of a) electric field E_r and b) ground acceleration $\ddot{U}_r$ recorded for the M_W8.1 Pisagua earthquake at stations PB01 to PB15 of the CX network of IPOC ordered by epicentral distance (locations in Tab. 2.1 and Fig. 2.2), c) corresponding envelopes and scaling factors s representing an average of $d|E_r|/d|\ddot{U}_r|$, and d) SE spectral ratios (SESRs). The envelopes and SESRs were smoothed by averaging the functions in a moving window. The SESRs were computed from the spectra of the time intervals indicated in column a).*

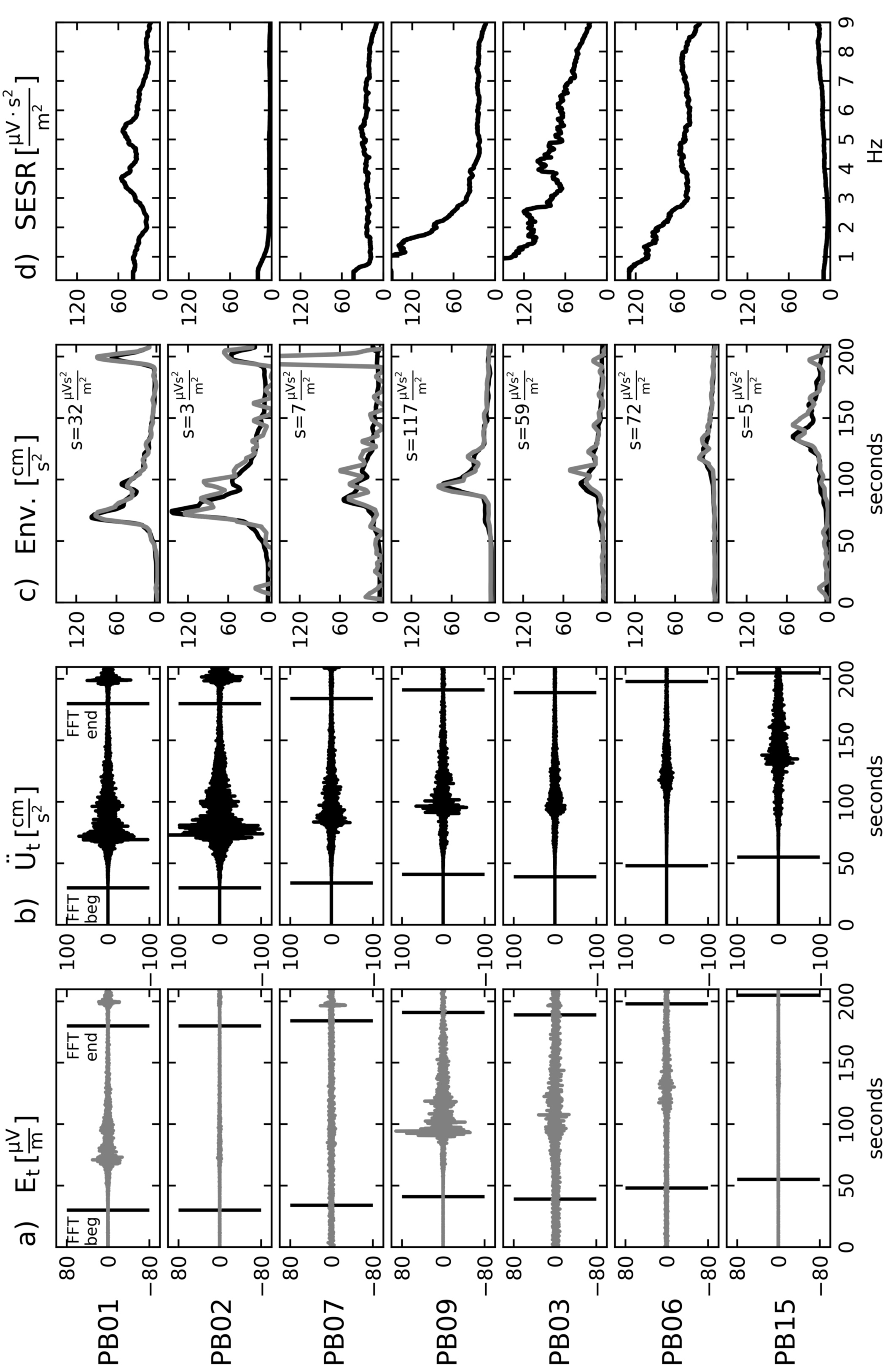

Fig. 2.5: *Transverse components of a) electric field E_t and b) ground acceleration $\ddot{U}_t$ recorded for the M_W8.1 Pisagua earthquake at stations PB01 to PB15 of the CX network of IPOC ordered by epicentral distance (locations in Tab. 2.1 and Fig. 2.2), c) corresponding envelopes and scaling factors s representing an average of $d|E_t|/d|\ddot{U}_t|$, and d) SE spectral ratios (SESRs). The envelopes and SESRs were smoothed by averaging the functions in a moving window. The SESRs were computed from the spectra of the time intervals indicated in column a).*

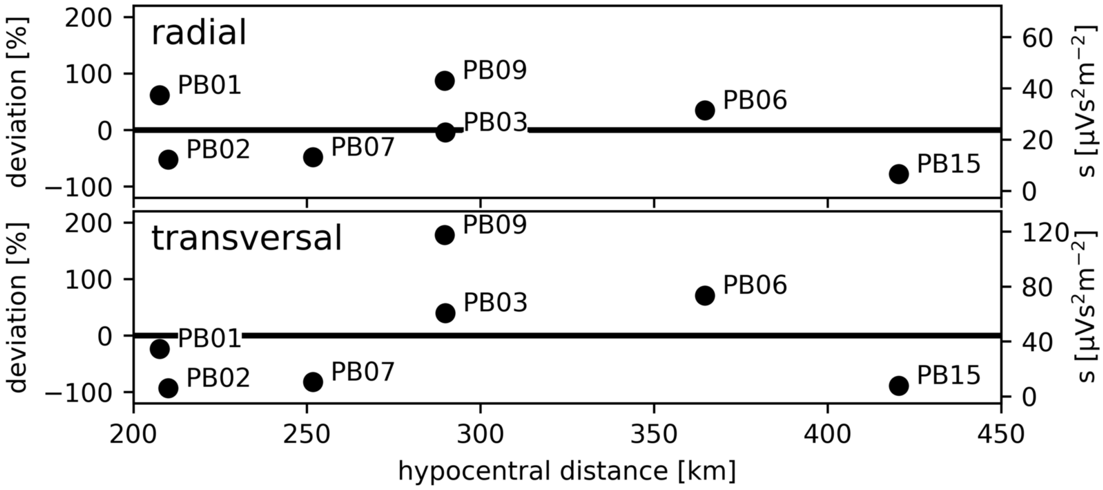

Fig. 2.6: *Scaling factors between electric and seismic envelopes of radial and transverse components (s in Figs 2.4c and 2.5c) of M_W8.1 Pisagua earthquake as a function of epicentral distance of the stations of the CX network of IPOC.*

earthquakes recorded at two stations. We chose stations PB02 and PB09 as an example for this comparison because they show the most distinguished SE signals for all displayed events.

The selected events are the M_W8.1 Pisagua earthquake (EQ1) and two of its aftershocks. The first aftershock (EQ2) occurred on April 3, 2014 at 02:43:12.71 UTC with a moment magnitude of 7.6. It is considered the biggest aftershock of the Pisagua earthquake (Schurr et al., 2014). The second aftershock (EQ3) also took place on April 3, 2014 at 01:58:27.96 UTC. It had a moment magnitude of 6.5. Further details of the earthquakes can be found in Tab. 2.2. The locations of earthquakes and recording stations are shown in Fig. 2.2. In Figs 2.7 and 2.8 the earthquakes are ordered according to their magnitude. The data was processed in the same way as described in section 2.4.1.

Comparison of the records for each station shows that the derived characteristic properties are basically the same for each earthquake but different for both stations (Figs 2.7 and 2.8). The envelopes seem to fit quite well for both stations. The scaling factors s are in the same order of magnitude for all three earthquakes but different for station and component (s in Fig. 2.7c,g and 2.8c,g). While on station PB02 the scaling factors of the radial components are larger than that of the transversal component, the opposite is true for station PB09. This indicates again vast 3D scattering. The SESRs reveal the same features for the different earthquakes. The SESRs of station PB02 are more or less constant whereas the SESRs of station PB09 reveal a similar decreasing trend towards increasing frequencies (Fig. 2.7d,h and 2.8d,h).

The fact that the scaling factor and the trend in the SESRs are similar for different earthquakes but not for different locations confirms that both the average scaling factors as well as the SESRs can be considered as expressions of a characteristic SE site effect.

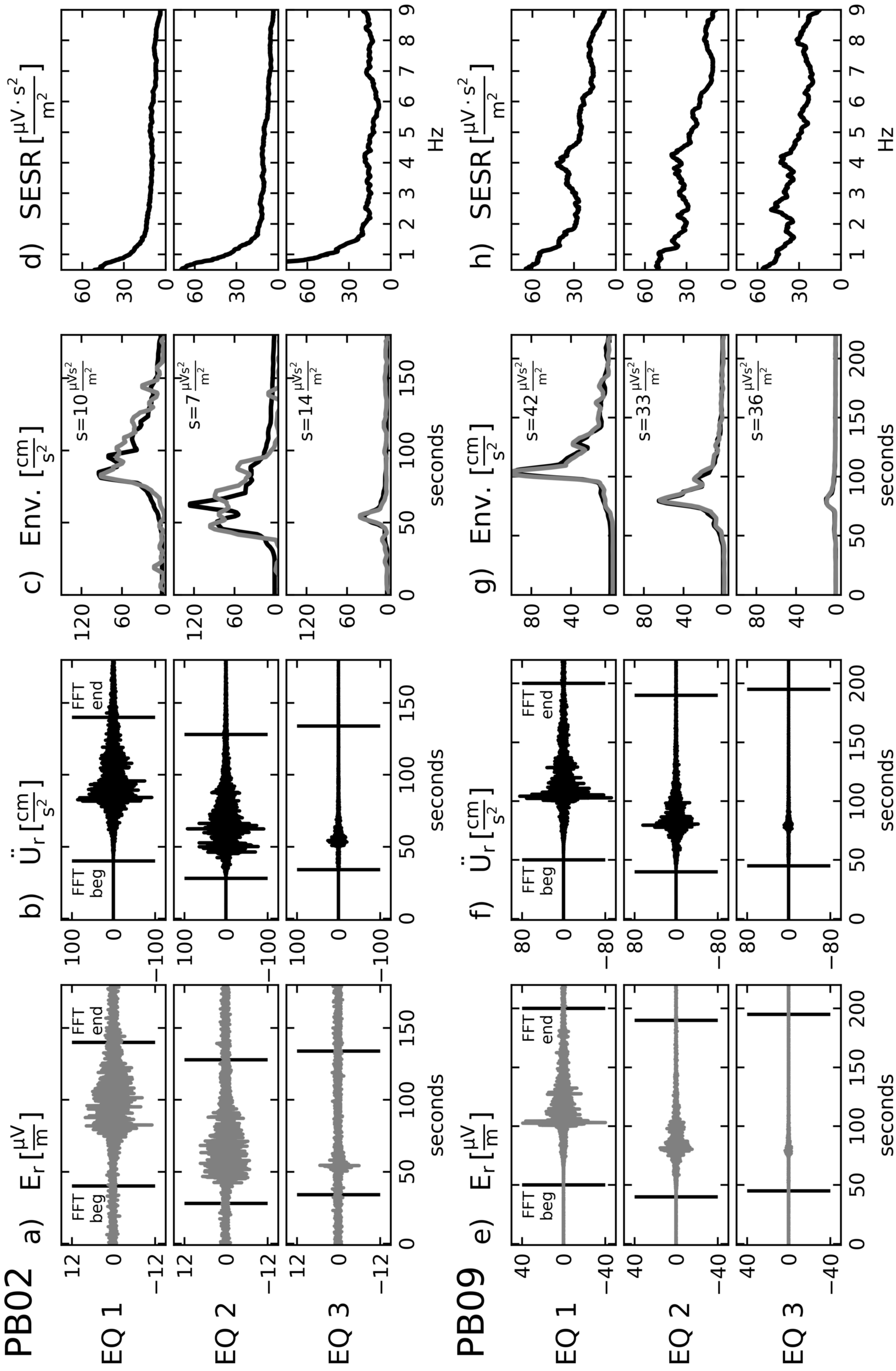

Fig. 2.7: *Radial components of electric field E_r (a, e), ground acceleration $\ddot{U}_r$ (b, f), corresponding envelopes (c,g) and SESRs (d, h) recorded for the $M_W8.1$ Pisagua earthquake (EQ 1) and two aftershocks (EQ 2 and EQ 3) at stations PB02 (a-d) and PB09 (e-h) of the CX network of IPOC. Envelopes and SESRs were smoothed by averaging the functions in a moving window. The SESRs were computed from the spectra of the time intervals indicated in columns a),b) and e),f).*

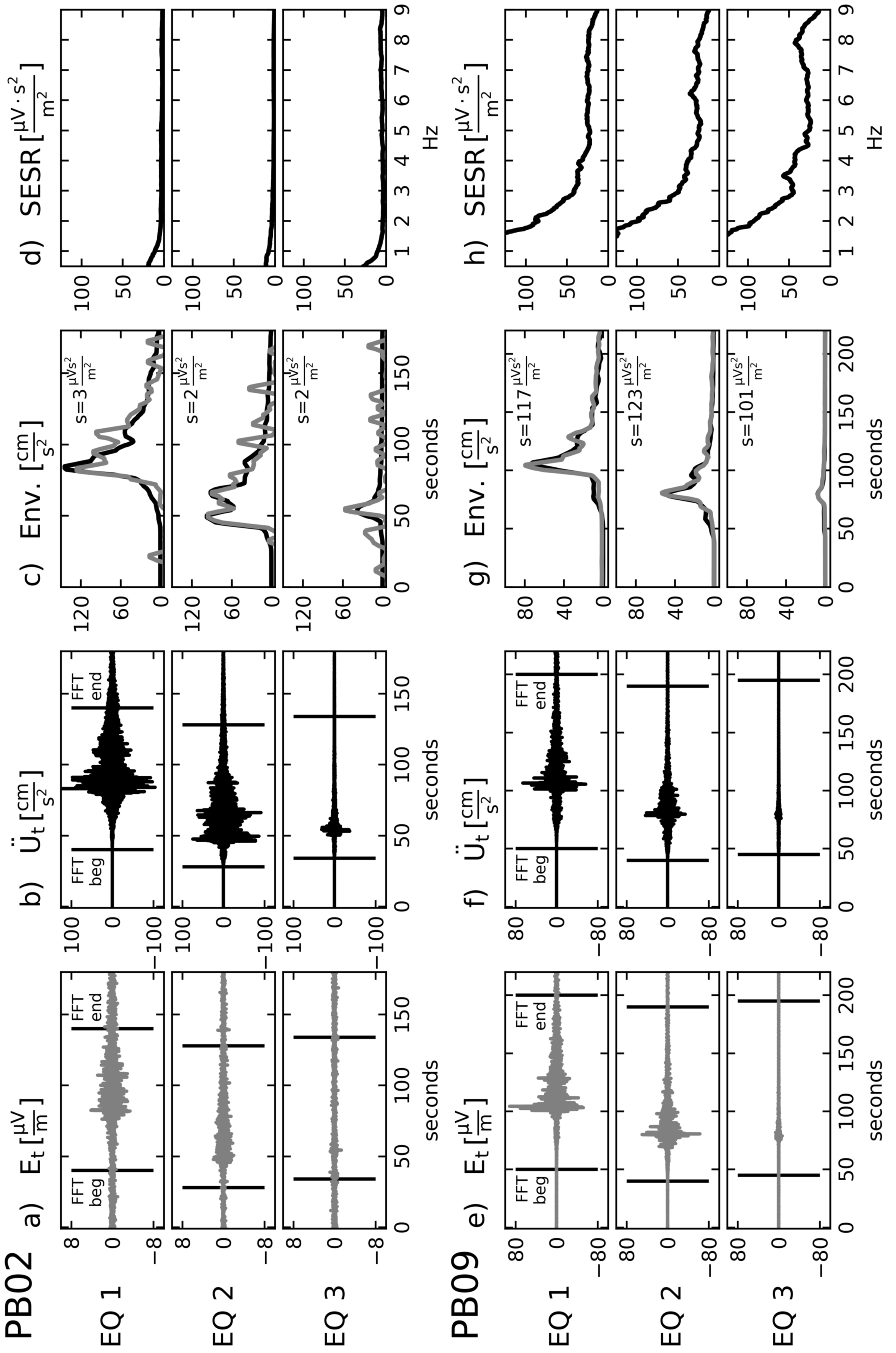

Fig. 2.8: *Transversal components of electric field E_t (a, e), ground acceleration $\ddot{U}_t$ (b, f), corresponding envelopes (c,g) and SESRs (d, h) recorded for the M_W8.1 Pisagua earthquake (EQ 1) and two aftershocks (EQ 2 and EQ 3) at stations PB02 (a-d) and PB09 (e-h) of the CX network of IPOC. Envelopes and SESRs were smoothed by averaging the functions in a moving window. The SESRs were computed from the spectra of the time intervals indicated in columns a),b) and e),f).*

2.5 Discussion

In the discussion we address the questions raised in the introduction:
First, which is the minimum earthquake magnitude required for observing SE fields at a given hypocentral distance with standard state-of-art seismic and MT field equipment under low to moderate ambient noise conditions? We have shown that it is possible to establish magnitude-distance functions to estimate a probability for detecting SE signals from earthquakes. We also showed, that these detection thresholds change in dependence of the local noise levels. The chosen logarithmic threshold functions, which basically represents seismic amplitude decay by geometrical spreading, fit our observations well. However, our recording sites represent only a small fraction of the many different near-surface geological conditions found on earth. For developing a global relationship, data from many more stations and different environments are needed. Such a global relationship can be expected to show considerable error bars, as our results indicate that SE amplitudes are highly dependent on site effects. Nevertheless, we believe that our method can be used as a first indicator to decide whether or not it is possible to detect SE signals of particular earthquakes.
Second, how do site effects influence SE signals? Based on our analysis we could show that the SE ground response to seismic waves from earthquakes is influenced by site effects in a characteristic way. This is confirmed by the wide 200% range of E-to-Ü scaling factors, which indicates different SE sensitivities for the different sites. We found it surprising that the records of the transverse components of the E and Ü fields show almost the same characteristics as the radial components. We see this as an indication that 3D scattering plays a major role in seismic and SE signal generation in our investigation areas. Therefore, P- and S-arrivals and their corresponding SE fields cannot be separated by simple rotation of the coordinate system over the backazimuth into r- and t-components.
A surprising observation is that the SE wave fields accompany both P- and S-wave trains to almost the same degree, whereas coseismic SE arrivals are expected to accompany only P-waves according to Biot's theory and electrokinetic coupling (e.g. Garambois and Dietrich, 2001). Possible explanations could include the conversion of S- to P-waves at the free surface and P- and S-waves being continuously converted into each other in scattering media. Additionally, a large amount of interface response arrivals will be created which contribute to the signal generation and influence the waveform. It can be assumed that the occurrence of IR arrivals is a local site specific effect because IRs form electric dipole fields that decay strongly with distance from the generating interface. In contrast, seismic scattering and related coseismic SE arrivals occur all along the wave paths.
The SESR functions were computed for the whole data record including P- and S-waves and coda. This was motivated by the omnipresence of SE arrivals all along the wave train, which is causing 3D scattering and S-to-P conversion at the (rough) free surface. For the same reason pure P and pure S portions of the wave field cannot be identified. Indeed, in the beginning of our studies, we considered including only the start of the wave train into the SESR computation assuming it mainly consisted of P-waves. However, the results depended on the lengths of the applied time windows and tapering functions. To avoid these effects, we chose to include the total ground response in the spectral computations,

which we find justified by the scattering nature of the media.
For low frequencies (< some 100 Hz) a transfer function can be defined relating the amplitudes of coseismic SE fields and ground acceleration (Garambois and Dietrich, 2001). The scaling factors relating our observed SE fields to ground acceleration are in the range of 5 to $\sim$ 120 $\mu Vs^2/m^2$. These values are of the same order as the values found for dry sand in the low frequency limit ($\sim$100 $\mu Vs^2/m^2$) by Garambois and Dietrich (2001), which is plausible because the stations of the CX network are located in the Atacama Desert.
Comparison of SE spectral ratios of different stations shows that basically two groups of SESRs can be distinguished: The SESRs are either flat or they decrease with increasing frequencies. Spectra of SE signals consisting mainly of coseismic arrivals should be very similar to spectra of the seismic field, because the transfer functions show only little frequency dependence in the considered frequency range of 1 to 10 Hz (Garambois and Dietrich, 2001). Therefore, we assume that the SE records of stations showing flat SESRs basically consist of coseismic arrivals. The group of SESRs showing a decay with frequency could tentatively be explained by an interference of coseismic and IR arrivals because electromagnetic waves such as IR show frequency dependent absorption: high frequency portions of the EM wave field are attenuated stronger than low frequency portions. Since the frequency dependency of the SESRs is independent of epicentral distance it has to be regarded as a site-specific effect. We assume that it is caused by IR arrivals originating from geological interfaces not too far from the stations which would interfere with the coseismic wave train instead of traveling in front of it.
Clearly the conclusion that IRs are the cause for decaying SESRs has to be regarded with some care, especially because the analyzed wave-sections are not purely P-wave. These effects will be investigated quantitatively in a future modeling study. However, at this point we can state already that the frequency dependence of the SESRs was shown to be independent of epicentral distance but variable with recording location. Therefore, we consider the frequency dependence of the SESR as an expression of a SE site effect.

2.6 Conclusions

Based on more than 16,000 earthquakes from Costa Rica, Chile and Norway we derived magnitude-distance-relationships describing under which conditions SE signals can be observed with a certain probability at given hypocentral distances, assuming standard magnetotelluric recording units. The observability swell of SE signals from earthquakes can be described by a logarithmic function according to formulae 2.1 to 2.3, which are based on the formula for geometric spreading of seismic waves. For example, events of magnitude M > 4, 5, 6 have a chance of 67% to produce fully observable SE signals at hypocentral distances $r < 50, 150, 400$ km, respectively. These results apply to an electric ambient noise level inferior to 0.1 $\mu V/m$.
However, amplitudes of the SE signals do not only depend on hypocentral distance and earthquake magnitude but also on local site effects showing a up to 200% variation of seismic to SE signal transfer functions (scaling factors) at our investigation sites. The local geologic structure directly underneath the recording station creates a frequency de-

pendent SE site effect.
To quantify these site effects we computed ratios of the spectral amplitudes of SE records and acceleration seismograms (SESR). SESRs are almost constant in the major frequency range for half of the investigated stations which suggests that the SE ground response is mainly composed of coseismic SE signals. The transfer function of SE to seismic signal strengths is of the order of values for dry sand found in previous studies. However, some stations consistently show a decrease of SESR with increasing frequency, which suggests that electromagnetic interface response arrivals may contribute significantly to the observed SE field.

Acknowledgments First of all, we would like to thank the reviewers for their constructive comments. The data from Costa Rica was acquired during the SFB 574 Project ‘Fluids and Volatiles in Subduction Zones’. The data from Chile was acquired in the frame of the Integrated Plate boundary Observatory Chile Project (IPOC). The authors would like to thank Jaime Araya Vargas for the MT-data from Chile. The equipment was provided by the Geophysical Instrument Pool of the GFZ Potsdam (GIPP). The data from Norway was provided by the Geological Survey of Norway (NGU) and recorded with equipment of Westfälische Wilhelms-Universität Münster and Uppsala Universitet. The data used in this paper can be requested from the authors. The maps were created with Generic Mapping Tools (GMT) software (Wessel et al., 2013) and the data analyzed with ObsPy (Krischer et al., 2015). The first author is grateful for funding through a scholarship of the Christian-Albrechts-Universität Kiel (‘Landesgraduiertenstipendium’)

3 Quantifying Interface Responses with Seismoelectric Spectral Ratios

This chapter is based on the paper 'Quantifying interface responses with seismoelectric spectral ratios' published in Geophysical Journal International.
Citation: Dzieran, L., M. Thorwart, W. Rabbel, and O. Ritter, 2019: 'Quantifying interface responses with seismoelectric spectral ratios'. Geophysical Journal International, 217 (1), 108–121, doi:10.1093/gji/ggz010.

Summary We investigate seismoelectric (SE) signals accompanying seismic waves radiated from earthquake sources. SE signals are mostly generated from compressional portions of seismic waves by electrokinetic coupling. They contain coseismic electric fields travelling with seismic wave velocity and interface response (IR) waves, which originate at layer interfaces and travel with EM wave speed. IR wave amplitudes are sensitive to contrasts in poroelastic and electric rock parameters. We introduce seismoelectric spectral ratios (SESRs) as a tool to evaluate the influence of IRs on the overall SE signal independently of the earthquake source time function. Based on data from Northern Chile we show that SESRs show a site specific frequency dependence with a trend of decreasing amplitudes towards increasing frequency. Modelling results reveal that the specific frequency dependence of the SESRs is caused by IRs excited at depths of some hundred meters underneath the recording stations. We analyse the SESR sensitivity towards porosity, permeability, fluid salinity and the depth of the interfaces. We verify that observed SESRs can be reproduced through forward modelling and linearised inversion based on realistic subsurface parameters.

3.1 Introduction

On multiple occasions a great resemblance has been observed between seismograms and electric signals of earthquakes (e.g., Honkura et al., 2000; Nagao et al., 2000; Matsushima et al., 2002; Huang, 2011; Gao et al., 2016; Dzieran et al., 2020). A variety of explanations for this phenomenon exist, such as piezoelectric origins (Huang, 2002) or a seismic dynamo effect, suggesting that the electric signals are induced by a conductive crust vibrating in the earth's magnetic field (e.g., Honkura et al., 2000; Matsushima et al., 2013; Gao et al., 2014). At present, the most widely accepted explanation is electrokinetic coupling caused by fluid movement relatively to pore surfaces (e.g., Gao and Hu, 2010; Gershenzon et al., 2014; Ren et al., 2014; Gao et al., 2016).

The theory of electrokinetic coupling has been investigated sporadically since the mid of the last century (e.g., Ivanov, 1939; Frenkel, 1944; Thompson and Gist, 1993). An essential step forward in the quantitative understanding of this effect was made by Pride (1994) who developed a set of macroscopic equations for the coupling between the seismic and electromagnetic (EM) waves in a fully saturated medium based on Biot's theory (Biot, 1956, 1962) and Maxwell's equations. Pride's theory provided the basis for further investigations on the electrokinetic effect (e.g. Haartsen and Pride, 1997; Jardani et al., 2010; Ren et al., 2010; Schakel et al., 2011; Grobbe and Slob, 2016). Garambois and Dietrich (2001) used Pride's theory to derive transfer functions between the seismic and the electric field in the seismic frequency range. Warden et al. (2013) extended Pride's formulas to partially saturated media. An alternative approach for partially saturated media was developed by Revil and Mahardika (2013) and Jardani and Revil (2015). In 2016 Jouniaux and Zyserman published a review on electrokinetically induced seismoelectric, electroseismic and seismomagnetic signals for Earth sciences.

During the passage of seismic waves the electrokinetic effect creates two types of EM waves forming the so-called seismoelectric (SE) field: coseismic waves and interface responses (IRs).

The electric coseismic wave is an electric signal coupled to the seismic wavefield, travelling with the same velocity. According to Garambois and Dietrich (2001) the electric field amplitudes of these waves are directly proportional to ground acceleration connected with compressional movement. Numerical studies showed that SH-waves are also accompanied by coseismic signals, however their amplitudes are expected to be much smaller than those caused by P-waves (Bordes et al., 2015; Zyserman et al., 2016). Therefore, it may appear surprising to observe large coseismic SE arrivals during the S-phase of the wavetrain (Fig. 3.1a). However, this apparent contradiction is solved by considering that SV-waves are also likely to cause volumetric changes by S-to-P conversion at the earth's surface and internal interfaces (Fig. 3.1b).

IRs, sometimes also called 'converted waves', are created when the seismic wave crosses an interface and the electric current-balance, binding the coseismic electric field to the seismic wave field, gets disturbed. The IRs travel with the speed of EM waves and can therefore be detected earlier than the seismic and coseismic signals, from which they were generated. IRs can arrive at the earth's surface before the seismic first break, but also within the seismic wavetrain depending on the depth of the interface and the type of the generating wave (Fig. 3.1b). Like coseismic arrivals, IRs are generated not only from P-waves but also from S-waves via S-to-P conversion. Furthermore, Zyserman et al. (2016) recently showed that IRs, resulting from SH-waves via induction processes between the magnetic and electric field, can reach significant amplitudes.

IRs are sensitive to porosity, permeability, fluid salinity and fluid viscosity (Garambois and Dietrich, 2002) and consequently are of great interest for a hydraulic characterisation of the subsoil. SE measurements with artificial sources have shown that IR arrivals can be identified in seismoelectrograms and used for surveying the vadose zone and near-surface aquifers (e.g., Dupuis et al., 2007; Strahser et al., 2011; Rabbel et al., 2020). In these cases, IR arrivals could be detected and digitally processed with multi-channel recording by using the very large apparent velocity of IR arrivals on seismoelectrograms as an identification criterion.

In comparison to these near-surface measurements it is much more difficult to find direct evidence of IR arrivals in earthquake records. This is mainly for two reasons: (1) the electric field is typically recorded with magnetotelluric stations at station spacings too large for array analysis, which is why the apparent slowness of IR arrivals cannot be used as an identification criterion. (2) The amplitudes of IR waves are usually small compared to the ambient noise, which makes detection of IR events difficult even if they precede the seismic first break.

Motivated by the frequent observation of clear SE arrivals from earthquakes on telluric records we have investigated a way to identify IR arrivals despite these difficulties in order to develop their information content for subsurface characterisation. The starting point of the considerations presented in the following is that coseismic SE signals and seismic ground acceleration can be expected to be proportional if the theory of Pride (1994) and the low-frequency approximation of Garambois and Dietrich (2001) hold. The factor of proportionality depends only on near-surface soil properties and – in the low-frequency limit – not on frequency. Thus, the presence of IRs in the SE record should lead to deviations from this proportionality and independence of frequency.

Seismoelectric and seismic field records of signals from natural sources (earthquakes) clearly depend on the source spectra. For making the results of the analysis of different earthquakes comparable to each other the source spectra have either to be accounted for or to be eliminated in the analysis. The latter can be realised without detailed knowledge of the source by forming the ratio of the frequency spectra of the SE and the seismic field records. We name this ratio SESR (SeismoElectric Spectral Ratio) (Dzieran et al., 2020).

The subject of the present paper is to quantify the influence of IRs on the SE signals, their spectra and on the SESRs. We have structured the paper in the following way: First, we will explain the concept of the SESRs and their physical significance (section 3.2). Next we will present SESRs calculated for three earthquakes from the subduction zone in northern Chile at three different stations (section 3.3). Last, we will present synthetic SESRs derived by forward modelling and inversion to evaluate the SESR approach and investigate the sensitivity of the SESRs with respect to parameter variations of the subsurface (section 3.4).

3.2 SeismoElectric Spectral Ratios (SESRs)

SE signals from earthquakes are a mixture of coseismic signals and IRs. To evaluate the influence of the IRs in the signal composition we use the ratio of the electric and seismic amplitude spectra.

For defining the SESR formula we make the following two assumptions:

(i) The horizontal components of the coseismic electric field and the ground acceleration, both measured at the earth's surface, are proportional to each other, according to Garambois and Dietrich (2001).

(ii) In the analysis we consider the principal components of the horizontal electric and seismic fields, $E(t)$ and $\ddot{U}(t)$, which are determined from the recorded horizontal com-

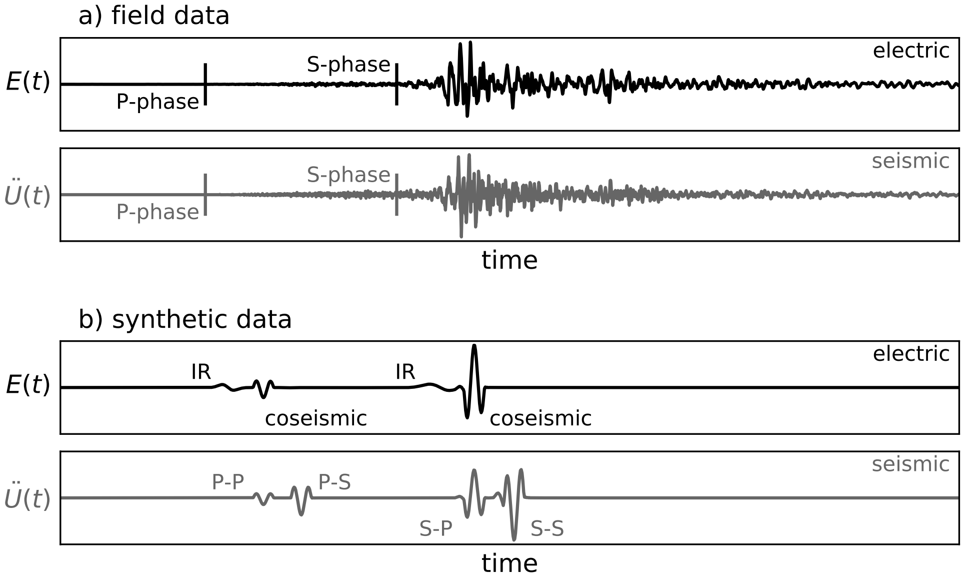

Fig. 3.1: *Examples of the main components of the seismoelectric field* $E(t)$ *and the seismic acceleration* $\ddot{U}(t)$*: a) observed waveforms from a M8.1 earthquake at 290 km distance to MT-station, b) synthetic data for a shallow layer overlying a halfspace; coseismic signals are proportional to and concurrent with seismic P-waves, IRs appear before and within the seismic wavetrain.*

ponents by polarisation analysis and corresponding rotation of sensor coordinate system. In isotropic 1D layered media the principal components of both fields would be oriented in the backazimuth direction. In more general types of media the orientations of $E(t)$ and $\ddot{U}(t)$ can disagree. A disagreement can be caused, for example, by fracture systems with a preferred orientation leading to electric and seismic anisotropy. In other words: In using $E(t)$ and $\ddot{U}(t)$ we assume that the proportionality of the horizontal components of the coseismic SE and seismic fields, which is proven for homogeneous media, holds locally for more complicated media, too.

The SE field $E(t)$ and the seismic ground acceleration $\ddot{U}(t)$, understood as the respective principal horizontal field components, are the result of the convolution of the respective Green's functions $GE(t)$ and $G\ddot{U}(t)$ with the same source function $SF(t)$. In the frequency domain the convolution equals a multiplication leading to:

$$E(\omega) = GE(\omega) \cdot SF(\omega) \tag{3.1}$$

$$\ddot{U}(\omega) = G\ddot{U}(\omega) \cdot SF(\omega) \tag{3.2}$$

The ratio of the SE and the seismic field in the frequency range thus is:

$$SESR(\omega) = \frac{E(\omega)}{\ddot{U}(\omega)} = \frac{GE(\omega)}{G\ddot{U}(\omega)} \tag{3.3}$$

With reference to the method of the standard spectral ratio (SSR) first introduced by Borcherdt (1970), we suggest calling this ratio the ‘SeismoElectric Spectral Ratio’ (SESR). Coseismic signals are proportional to seismic acceleration which is why the respective Green’s functions and their spectra should follow the same frequency trend. Consequently, if a SE event consisted purely of coseismic signals, the frequency dependency of the two Green’s functions as well as the source function should cancel each other out, resulting in a constant SESR. If on the other hand the coseismic signals were mixed with IRs, the SE spectrum would deviate from the coseismic spectrum and the corresponding seismic spectrum leading in this case to a frequency dependent SESR.

To illustrate this, we computed synthetic seismic and SE spectra for a halfspace model that includes an interface 5 km above the source. The receiver for which the spectra are calculated is situated 100 m above the interface in an epicentral distance of 50 km, which means, that the offset is ten times larger than the source depth. For simplicity only the signals related to the fast P-wave were included into the calculation. Details of the modelling can be found in Appendix 3.A.1.

The normalised seismic and SE spectra as well as the corresponding SESRs can be seen in Figs 3.2a-c. As expected, the seismic spectrum (Fig. 3.2a) and the coseismic spectrum (Fig. 3.2b, line II), are proportional to each other, while the SE spectrum including IRs (Fig. 3.2b, line I) deviates from this form. The resulting SESR of the full SE field therefore shows a decreasing trend, while the SESR from the coseismic field is frequency independent (Fig. 3.2c, lines I and II).

In the next section we present SE field data recorded at epicentral distances that are a lot larger than the corresponding earthquakes’ source depths. Therefore the question needs to be addressed whether IRs can be expected to be recorded at these offsets. Garambois and Dietrich (2002) showed that IRs are developed over a Fresnel zone that is positioned directly beneath a source located at the earth’s surface. However recent studies suggest that for incident angles larger than the critical angle $\theta_{\mathrm{c}} = \arcsin(\mathrm{v}_{\mathrm{seis}}/\mathrm{v}_{\mathrm{em}})$, so called evanescent IRs are excited (Ren et al., 2015, 2018; Butler et al., 2018). The evanescent IRs are carried along the interfaces by the seismic waves and can therefore be detected further away from the source. Fig. 3.2d and e show snapshots of the SE field as well as the IR for the same model configuration that was used to calculate the spectra and SESRs in Fig. 3.2a to c. When comparing Figs 3.2d and e, one can see that IRs are excited at the locations, where the coseismic waves cross the interface, confirming that the IRs causing the decreasing trend in the SESR is indeed evanescent. Therefore, SESRs are influenced by (evanescent) IRs even at large distances as shown in Fig. 3.2c. Furthermore we expect, that the shape of the SESRs decrease with increasing frequencies, because the amplitudes of evanescent IRs decay approximately with $exp(-\omega p \Delta z)$ (p - slowness, Δz - distance between receiver and interface) (Ren et al., 2018).

In the next section we present SESRs calculated for three earthquakes recorded on three different stations in northern Chile to investigate whether our assumptions can in fact be confirmed by field data.

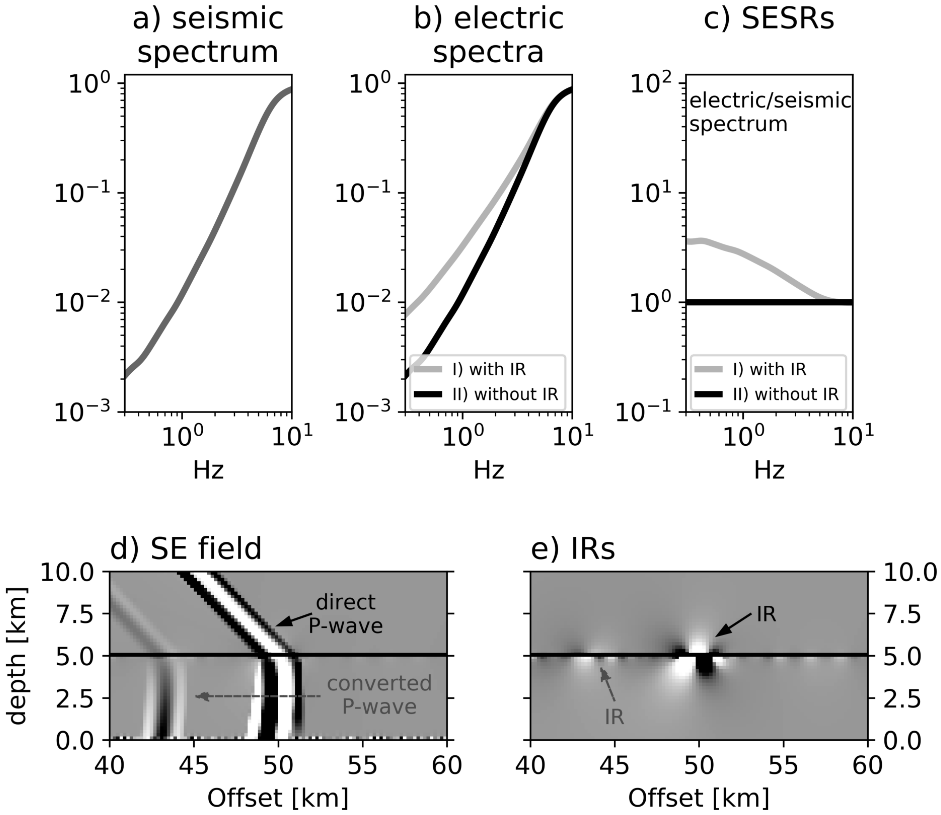

Fig. 3.2: *Synthetic calculations for a halfspace model including an interface 5 km above the source. The seismic spectrum (a), electric spectra (b), and SESRs (c) were calculated for a receiver at 50 km offset. d) and e) show the corresponding snapshots of the SE field and the IR.*

3.3 Field examples

We calculated SESRs for three earthquakes recorded by three different stations (cf. Fig. 3.3 for locations). The Mw 8.1 Pisagua-Iquique earthquake (EQ1) took place on April 1st, 2014 and ruptured the central fraction of the northern Chile-southern Peru seismic gap. A few minutes later a large aftershock of magnitude 6.5 occurred (EQ2). In the early morning of April 3rd, 2014 the largest aftershock was recorded with a magnitude of 7.6 (EQ3). The ruptures of EQ1 and EQ3 propagated downdip over several tens of seconds with co-seismic slips of 4.4 m and 1.2 m, respectively. Overall, they broke a segment of 200 km (Schurr et al., 2014). Detailed information about the analysed earthquakes can be found in Tab. 3.1.

The three earthquakes were, among others, recorded on stations PB01, PB02 and PB09 of the permanent CX-network run by the Integrated Plate Boundary Observatory Chile (IPOC) (GFZ & CNRS-INSU, 2006). The stations are equipped with FBA-EST accelerometers, which record the seismic acceleration with a sampling rate of 20 Hz. The electric field is measured by MT-stations along the north-south and east-west directions, also with a 20 Hz sampling rate. This relatively low sampling rate is an advantage as

	Time	Latitude	Longitude	Depth	Magnitude
EQ1	2014/04/01 23:46:49	-19.59°	-70.73°	34 km	8.1
EQ2	2014/04/01 23:49:27	-20.03°	-70.28°	16 km	6.5
EQ3	2014/04/03 02:43:17	-20.5°	-70.36°	37 km	7.6

Tab. 3.1: *Properties of earthquakes analysed in this paper. Details were provided by the GEOFON Data Centre (1993).*

Station	Latitude	Longitude	epicentral distances to EQ1 / EQ2 / EQ3	Electrode distances (NS/EW)
PB01	-21.0432°	-69.4874°	207 km / 139 km / 109 km	81.4 m / 80.3 m
PB02	-21.3197°	-69.8960°	210 km / 148 km / 103 km	84.8 m / 80.9 m
PB09	-21.7964°	-69.2419°	289 km / 223 km / 185 km	80.0 m / 80.8 m

Tab. 3.2: *Location, epicentral distances and electrode distances of the recording stations of the CX-network (IPOC).*

the Nyquist frequency lies at 10 Hz and therefore the SE recordings are not influenced by man made harmonic noise, such as power lines for example. The electrode dipoles of the MT-stations consist of Ag-AgCl-electrodes and have a length of approximately 80 m. Detailed information about the stations are listed in Tab. 3.2.

The following steps of data processing were applied to calculate the SESRs:
(i) Correction for instrument response and high pass filtering: After the instrument response was eliminated from the SE and seismic time series, a 0.1 Hz high pass filter was applied to minimise low frequency influences. To eliminate sporadic anthropogenic bursts the data was despiked before the high pass filter.
(ii) Determination of the principal components of horizontal electric and seismic wavefields: The orientation of the principal components was determined by hodogram analysis. The components were then computed by corresponding rotation of the sensor coordinate system.
(iii) Calculation of amplitude spectra and SESR: The amplitude spectra of the seismic and the seismoelectric traces were calculated with a Fast Fourier transformation (FFT) over a time duration of 150 s. The spectra were smoothed with the Konno-Ohmachi smoothing filter, for which the bandwidth is constant on a logarithmic scale (Konno and Ohmachi, 1998). After that, the SESR was calculated as the ratio between the smoothed SE and seismic spectrum.
For the calculation of the SESR we chose a time window of 150 s. This window includes the P- as well as the S-phase, which is problematic as the proportionality between the seismic acceleration and SE field is only valid for compressional waves. There are however several reasons why we chose to use the whole wavetrain. One of them is the low sampling rate of the measured data. If we only included the P-phase into our calcula-

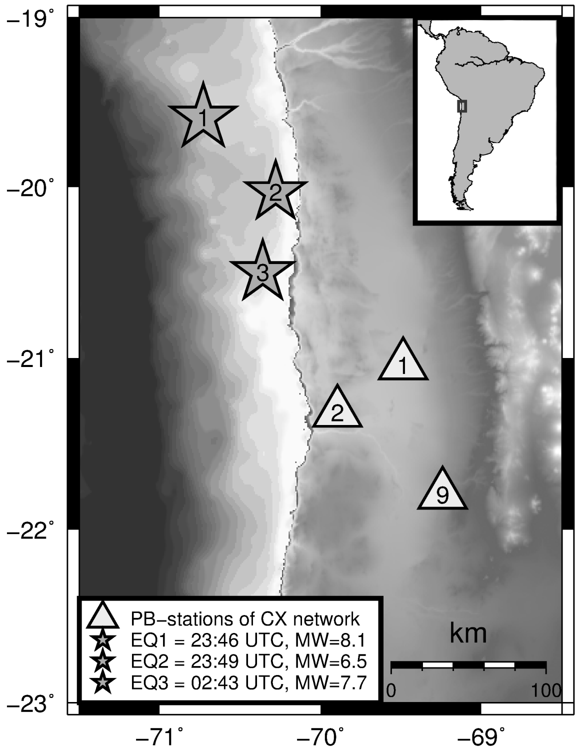

Fig. 3.3: *Location of earthquake epicentres and recording stations of the CX-network (IPOC) in Northern Chile presented in this paper.*

tions the results would become numerically unstable due to the small number of samples. Additionally, because of the small SE amplitudes in the P-phase the signal to noise ratio is very low, meaning that the noise could easily influence our results. Lastly, we expect that due to scattering, SV- and SH-waves are also present in the P-phase and would not entirely be excluded if we restricted ourselves to that part of the wavetrain.

Figs. 3.4a to 3.4c show the time series for EQ1, EQ2 and EQ3 on stations PB01, PB02 and PB09, respectively. The earthquakes are easily identified on all records. Compared to the seismic signal strength the electric signal strength is much smaller on stations PB01 and especially PB02 than on station PB09, showing that the transfer functions between the SE and electric field are site dependent.

The SESRs were calculated for all earthquakes on each station (Fig. 3.4d). They all show a decreasing trend with increasing frequencies. Additionally, a great similarity can be found between SESRs on the same station. To compare the SESRs between the stations we calculated an average SESR for each location (Fig. 3.5). This reveals, that although all SESRs share a similar tendency, the trend differs between the stations. On stations PB01 and PB09 the SESRs decrease equally up to 0.3 Hz. Above that frequency the gradients of the two slopes stay similar but the amplitude of the average SESR at station PB01 is higher than that at station PB09. At 4 Hz, the decrease of the SESR at station PB01 stops, so that the SESR appears almost flat above that frequency. Between 0.2 and 1.4 Hz the decrease of the SESR at station PB02 is slightly steeper than on stations PB01 and PB09, although above 1.4 Hz the rate of the decay is also decreasing.

The field data shows that the SESRs are consistent for different earthquakes at the same station but differ among locations. The decreasing trend of the SESRs shows that the transfer function between seismic and seismoelectric signals depends strongly on frequency, which is in contrast to the frequency independence that is expected for pure coseismic signals. The agreement of the SESRs at each station in combination with the differences of SESRs between locations shows that the SESRs are probably more influenced by site effects than by actual earthquake characteristics. This supports our idea that IRs are causing the decreasing trends of the SESRs, although other effects should not be entirely excluded.

Due to their fast attenuation, we expect that the IRs observed at the earth's surface have to be excited in close vicinity to the recording stations as otherwise they would not influence the SE signals. The example calculated for a halfspace model in section 3.2 showed that we can expect evanescent IRs to influence SESRs recorded at large offsets (Fig. 3.2). The question is, how close to a station the IRs have to be excited to influence the SESRs significantly, considering that this is a Mw 8.1 megathrust eathquake. In the next section we therefore use synthetic data to evaluate our interpretation of the field data SESRs.

3.4 Modelling

3.4.1 Modelling and SESR calculation

The numerical modelling was performed with a Fortran code developed by Garambois and Dietrich (2002) and extended by Warden et al. (2013) for unsaturated media. Based on the general reflectivity method the code models seismo-electromagnetic wave propagation in stratified media excited by point forces. We used the code to calculate the spectral Green's functions (impulse-type point source) of the seismic, seismoelectric and seismomagnetic fields in a x,y,z-Cartesian coordinate system, with z pointing downwards. To investigate the IR contributions to the total signal we used the ability of the code to manually suppress the computation of IRs at selected interfaces and the free surface.

As an example, we chose to model the average SESR of station PB09 (Fig. 3.5), which we will further refer to as observed SESR. To obtain the corresponding modelled SESR, we calculated the seismic and SE Green's functions for a point force directed in z-direction. We chose the point force orientated in the vertical direction, as we inferred from the SE traces (Figs. 3.4 a-c) that the S-phase is more prominent than the P-phase, which corresponds to the radiation pattern of the P- and S-phase from a vertical point force. The point force is located at 25 km depth and the receiver is positioned at the surface at a distance of 135 km in x-direction and -190 km in y-direction, which is roughly the epicentre of EQ1 to EQ3.

We calculated the Green's functions for a time duration of 409.6 s with a sampling rate of 20 Hz, which is similar to the sampling rate of the field data. The Green's functions were smoothed as described in section 3.3 and then divided to calculate the SESRs.

The parameters of our subsurface model are based on a seismic velocity model of Sick

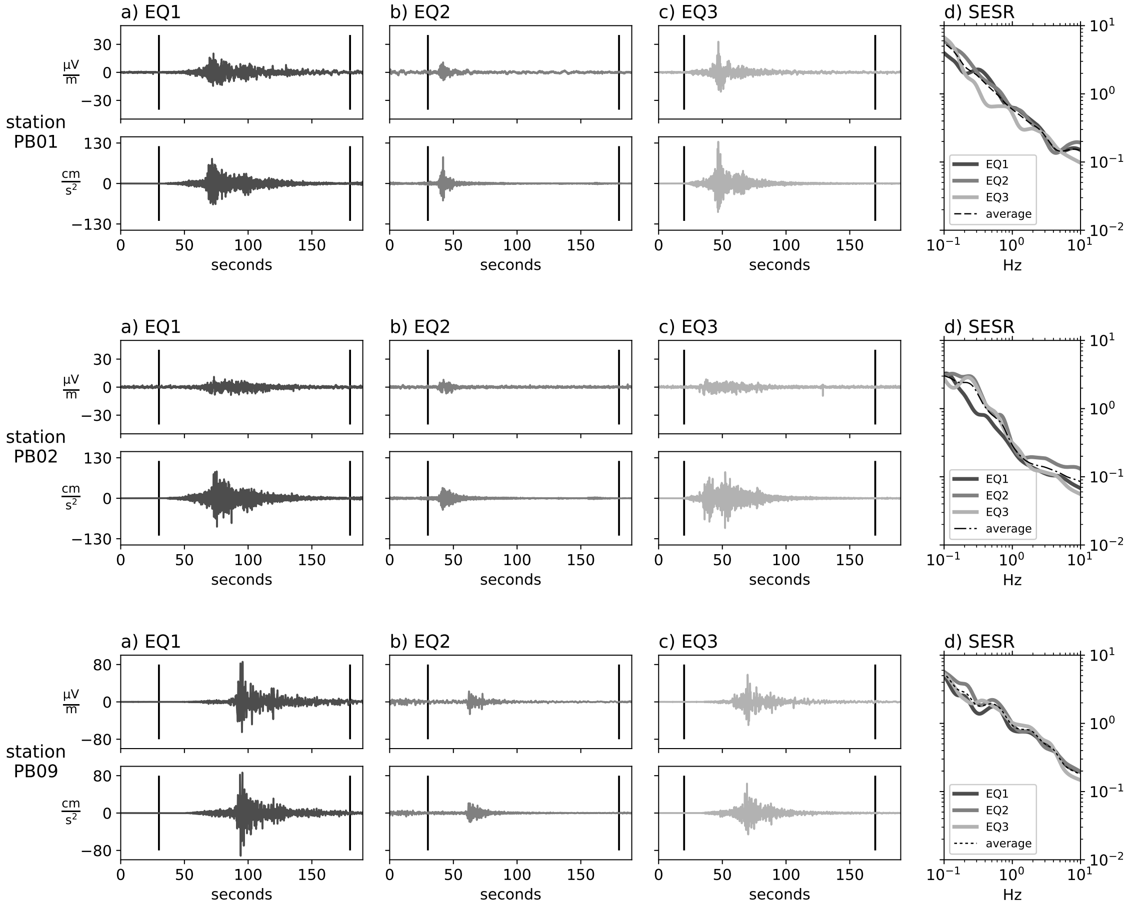

Fig. 3.4: *a)-c) Electric and seismic traces of EQ1-EQ3 recorded at stations PB01, PB02 and PB09. The SESR spectra were calculated for the data between the vertical black lines; d) Log-log plots of the SESRs of the data presented in a)-c)*

et al. (2006) and an electric resistivity model of Araya Vargas (2016), both developed for the region around station PB09. For modelling the site effect we inserted two shallow sedimentary layers at the surface. By manually modifying the depth, porosity and salinity of the upper three layers we gradually adjusted the form of the modelled SESR to that of the observed SESR. We restricted ourselves to altering the uppermost soil properties as first tests revealed that the shape of the modelled SESR was most sensitive to the parameters in this depth range. The main input-parameters of our final model as well as resulting subsurface properties are listed in Tab. 3.3 and shown in Fig. 3.6. Depth, porosity, permeability and fluid salinity values are direct input parameters, while the velocities and resistivity are calculated by the program. We assumed full saturation for all layers except the first, where we lowered the saturation to 75 %. The detailed input parameters for our calculations can be found in Tab. 3.5 in the appendix.

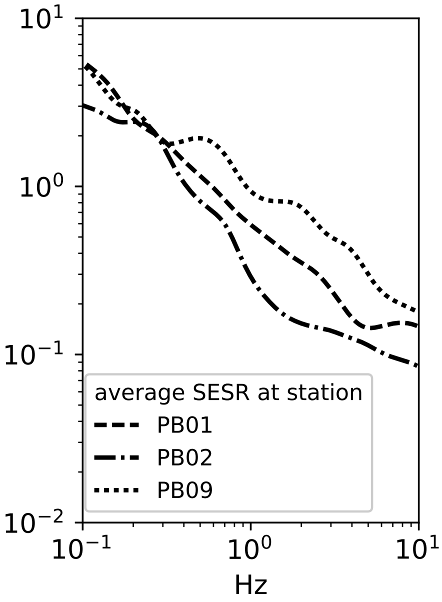

Fig. 3.5: *The average SESRs of stations PB01, PB02 and PB09, derived from the SESRs of EQ1-EQ3 (Fig. 3.4).*

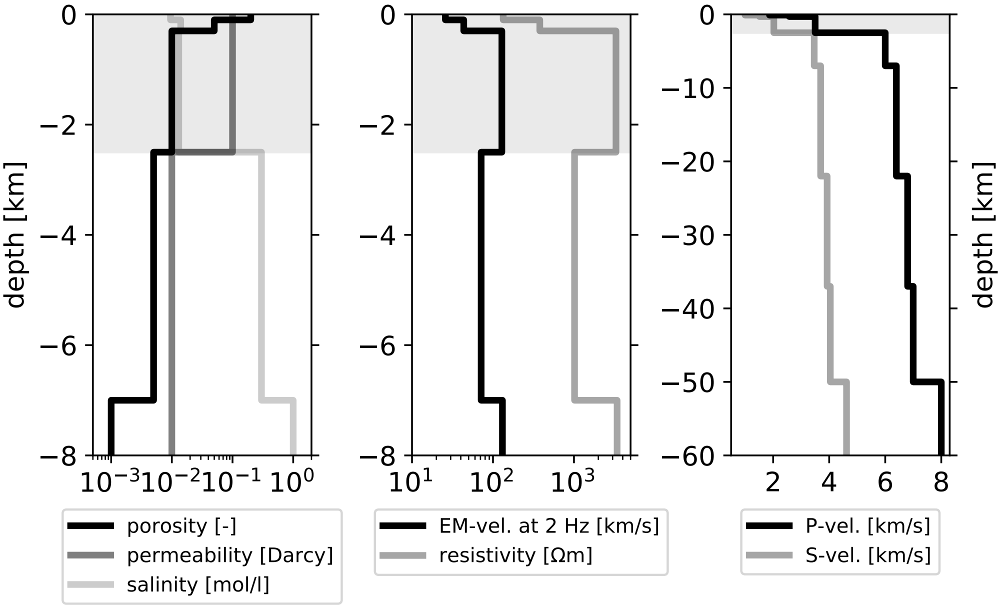

Fig. 3.6: *Layer properties used to model the SESR. The properties in the upper three layers (shaded area) were varied to adjust the behaviour of the modelled SESR to that of the observed SESR. Porosity, permeability and fluid salinity are input parameters; velocities and resistivity are calculated by the program. The values are constant outside of the displayed depth-range.*

layer	1⋆	2⋆	3⋆	4	5	6	7	8
depth [km]	0.1	0.3	2.5	7.0	22.0	37.0	50.0	>50
porosity [%]	20	5.0	1.0	0.5	0.1	0.1	0.1	0.1
permeability [Darcy]	0.1	0.1	0.1	0.01	0.01	0.01	0.01	0.01
fluid salinity [mol/l]	0.0095	0.014	0.013	0.3	1	1	1	1
*v_P [km/s]	1.87	2.57	3.5	6.0	6.4	6.8	7.0	8.0
*v_S [km/s]	1.00	1.51	2.02	3.47	3.69	3.93	4.04	4.62
*v_{EM} at 2 Hz [km/s]	25.8	43.5	128.7	71.4	130.8	130.8	130.8	130.8
*resistivity [Ωm]	134	378	3302	1016	3409	3409	3409	3409

Tab. 3.3: *Main properties of the layers used for modelling the average SESR of station PB09. The properties of the first three layers (⋆) were varied to adjust the form of the modelled SESR to that of the observed SESR. Depth, porosity, permeability and fluid salinity are input parameters; velocities and resistivity are calculated by the program (marked with *).*

3.4.2 Influence of Interface Responses

The modelled SESR agrees well with the observed SESR in the major part of the considered frequency interval (compare lines a and b in Fig. 3.7). A few deviations can be seen, especially for frequencies below 1.5 Hz, but the overall trend is well fitted. Thus we decided to use this model as a basis for further calculations.

To find out whether the shape of the SESR is influenced by IRs we calculated a comparative coseismic SESR without any IRs (Fig. 3.7 line c). As expected, the resulting SESR is flat showing no significant frequency dependency. This proves that IRs are in fact responsible for the decreasing trend of the SESR.

When thinking about possible applications, it is necessary to know at which depth the IRs that influence the shape of the SESR are excited. We therefore calculated SESRs based on the same model, successively allowing IRs to be created at deeper interfaces. When IRs are only allowed from the interface at 100 m depth the SESR deviates significantly from the SESR calculated with IRs from all interfaces (compare lines a and d in Fig. 3.8). However, when allowing IRs from interfaces at 100 m and 300 m depth, only a small deviation between that SESR and the original one can be seen in the low frequency range (compare lines b and d in Fig. 3.8). This shows that, at least for this model, the shape of the SESR is primarily influenced by the IRs created at the 100 m and 300 m deep interfaces. To verify this conclusion we calculated the SESR for a SE field, that only allows IRs created at interface deeper than 300 m (line c in Fig. 3.8). As expected, this SESR deviates from the coseismic SESR shown in Fig. 3.7 line c by a few percent only and for frequencies smaller than 0.6 Hz. This confirms that the SESR is majorly influenced by the parameters in the upper three layers.

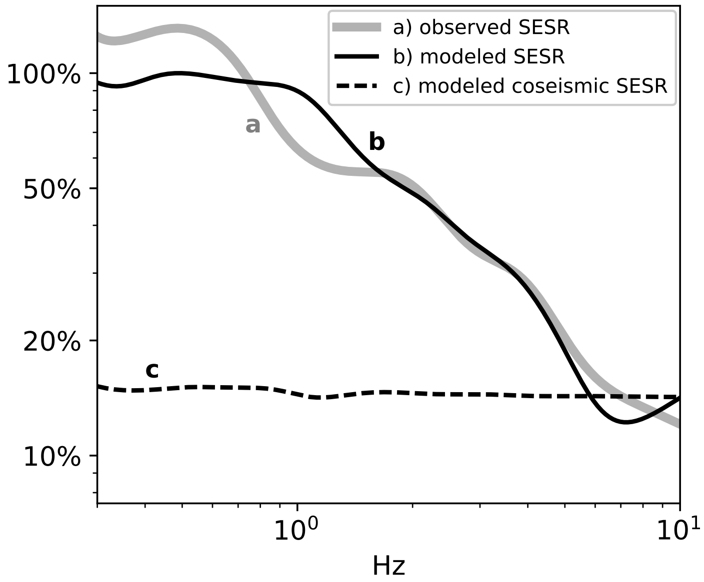

Fig. 3.7: *Comparison of the observed and modelled SESRs. a) observed SESR, b) modelled SESR including IRs at all interfaces c) modelled SESR of coseismic field (no IRs). The modelled SESRs (lines b and c) were calculated with the same input parameters. All SESRs are normalised to the maximum of the modelled SESR (line b).*

3.4.3 Influence of model parameters

Next we analyse the sensitivity of the SESR with respect to the different input parameters of the model. Garambois and Dietrich (2002) showed that porosity, permeability, fluid salinity and fluid viscosity have the strongest influence on the amplitudes of a single shallow IR. As in our model only the first three layers contribute relevantly to the IR signals, we calculated the sensitivity for these layers with respect to porosity, permeability, fluid salinity and depth, which from now on refers to the depth of the lower interface of the layer. The fluid viscosity was assumed to be constant.

Each of the parameters was varied independently by $\pm 1\%$. The relative change of the SESR at each frequency $\Delta S(\omega)$ was then calculated via:

$$\Delta S(\omega)_p = \frac{S_p^{+1\%}(\omega) - S_p^{-1\%}(\omega)}{2 \cdot S(\omega) \cdot 1\%} \tag{3.4}$$

where $S(\omega)$ is the original SESR and $S_p^{\pm 1\%}(\omega)$ the SESR resulting from the variation of parameter p.

Fig. 3.9 shows the results of the parameter variation. Although all parameter changes show a clear frequency dependency, no predominant trend can be seen. Except for the salinity in the third layer all parameter variations lead to positive as well as negative effects on the shape of the SESR regarding different frequency bands.

Overall, the SESRs do not vary more than 2% from their original form, except for the

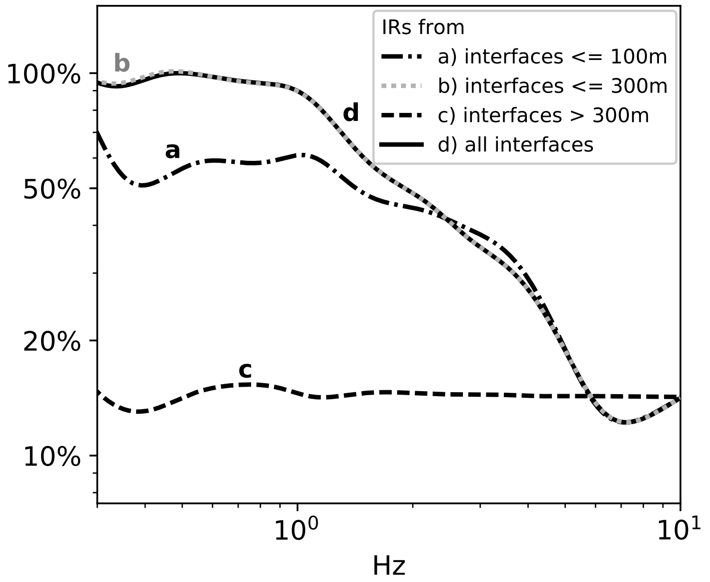

Fig. 3.8: *Comparison of SESRs with IRs being included sequentially for each interface. a) SESR including only IRs from interface at 100 m, b) SESR including only IRs from interfaces at 100 m and 300 m, c) SESRs including only IRs from interfaces at 2500 m and deeper, d) SESRs including IRs from all interfaces. All SESRs are normalised to the maximum of the modelled SESR (line d)*

depth of layer 3 (interface at 2500 m). Here the deviation of 1% leads to an SESR change of up to 5%. The permeability, with a sensitivity of less than 0.2%, has the least influence on the shape of the SESRs. This seemingly small effect can be explained by the low percentage (1%) by which the permeability is varied. Garambois and Dietrich (2002) for example varied the permeability by factor 10 in their study, which would consequently result in larger effects.

In the case of porosity and salinity the calculations show that the sensitivity decreases for deeper interfaces. Additionally, the effects of the parameter variation generally become larger for frequencies above 1 Hz. However, the sensitivity to permeability behaves differently. Not only is it stronger in the low frequency range (below 1 Hz) but the permeability in the deepest layer (considered layer 3) also seems to affect the SESR most. One explanation for the increased sensitivity in the third layer could be that contrary to the two upper layers there is already an existing permeability contrast between layer 3 and layer 4 (0.1 Darcy to 0.01 Darcy), which is enlarged even further by the parameter variation.

Another surprising result is the sensitivity of the response of the third layer with respect to depth, considering that the IRs from this interface should not influence the SESR at all (section 3.4.2). This effect can be explained by the fact that the sensitivity to the depth of the layer is, in this case, not related to the IRs themselves, but rather caused by differing travel paths of the seismic waves, resulting in wavefield variations. This shows that the absolute depth of the layer interfaces may have a relatively larger impact on the result than the material parameters themselves. This problem will be further addressed in the discussion (section 3.5).

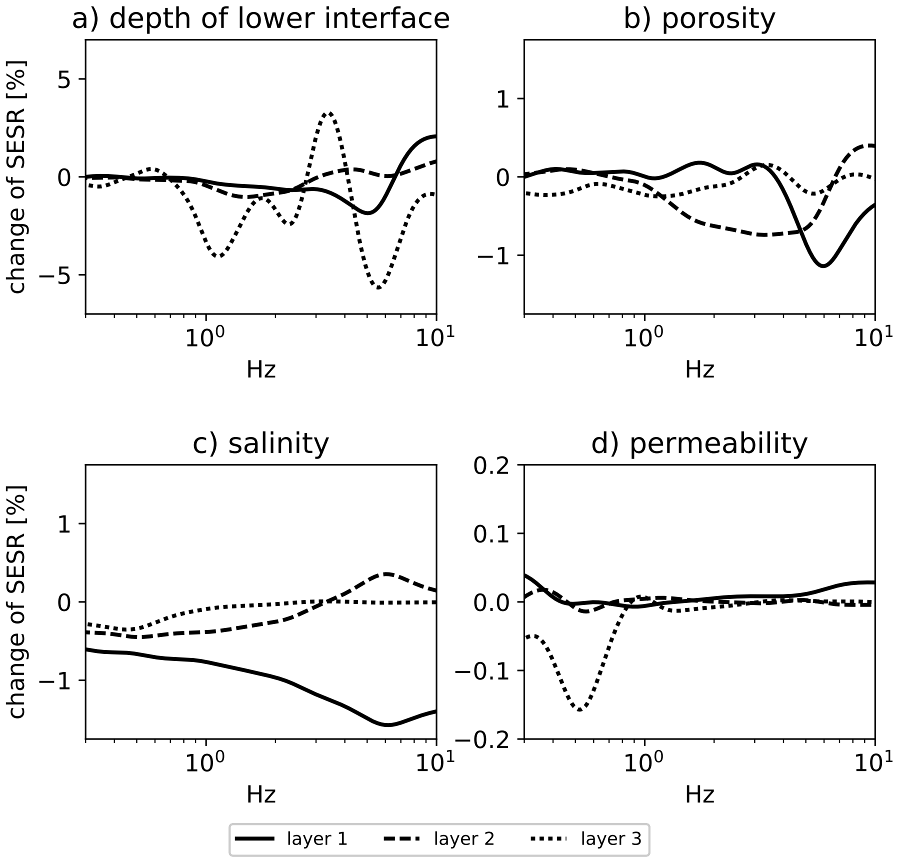

Fig. 3.9: *Sensitivity analysis: change of the SESR in % if a) depth of the lower interface, b) porosity, c) salinity and d) permeability in layers 1-3 are increased by 1 %.*

3.4.4 Inversion

Having calculated the sensitivities of the SESRs to the different parameters and layers, the next step is to implement an inversion algorithm to see whether it is possible to improve our model. For our inversion attempt we decided to use an iterative linearised inversion based on the Levenberg-Marquardt algorithm (Lines and Treitel, 1984).

The SESR S_f is a function of the rock properties m_p of the subsurface where the indices $f = 1, ..., n_f$ and $p = 1, ..., n_p$ indicate single frequencies and model parameters, respectively:

$$S_f = \mathscr{F}(m_p) \tag{3.5}$$

We assume that the observed and initially modelled SESR are similar. Then it is possible to express the observed SESR S_f^{obs} by a Taylor series expansion of $\mathscr{F}(m_p)$ around the modelled SESR S_f^{mod} and neglect the higher order terms.

$$S_f^{obs} \approx S_f^{mod} + \left.\frac{\partial S_f^{mod}}{\partial m_p}\right|_{m_p^{mod}} \Delta m_p \tag{3.6}$$

Since we linearise the Taylor series expansion we are using an iterative approach to gradually adjust the subsurface parameters:

$$S_f^{obs} \approx S_f^{i-1} + \left.\frac{\partial S_f^{i-1}}{\partial m_p}\right|_{m_p^{i-1}} \Delta m_p^i \qquad for\; i = 1, ..., n_i \tag{3.7}$$

where m_p^{i-1} are the subsurface parameters at the (i-1)-th iteration and S_f^{i-1} is the corresponding SESR. Following that, $m_p^i = m_p^{i-1} + \Delta m_p^i$ are the adjusted parameters after the i-th iteration resulting in the SESR S_f^i. The series of the modelled S_f^i is supposed to converge towards the observed S_f^{obs}. The subsurface parameters for the starting model m_p^0 are listed in Tab. 3.5 and the corresponding SESR S_f^0 can be seen in Fig. 3.7 (line b).
$(S_f^{obs} - S_f^{i-1})$ and Δm_p^i are normalised to express equation (3.7) in fraction:

$$\frac{S_f^{obs} - S_f^{i-1}}{S_f^{i-1}} \approx \left(\left.\frac{\partial S_f^{i-1}}{\partial m_p}\right|_{m_p^{i-1}} \frac{m_p^{i-1}}{S_f^{i-1}} \right) \left(\frac{m_p^i - m_p^{i-1}}{m_p^{i-1}} \right) \tag{3.8}$$

Eq. 3.8 is then expressed in terms of the data vector d_f^i, the kernel $G_{f,p}^i$ and the model vector $\Delta\tilde{m}_p^i$:

$$d_f^i = \frac{S_f^{obs} - S_f^{i-1}}{S_f^{i-1}} \tag{3.9}$$

$$G_{f,p}^i = \left(\left.\frac{\partial S_f^{i-1}}{\partial m_p}\right|_{m_p^{i-1}} \frac{m_p^{i-1}}{S_f^{i-1}} \right) = \Delta S_{f,p} \tag{3.10}$$

$$\Delta\tilde{m}_p^i = \left(\frac{m_p^i - m_p^{i-1}}{m_p^{i-1}} \right) \tag{3.11}$$

d_f^i can easily be calculated. $\Delta S_{f,p}$ is the change in the SESR at frequency f with respect to parameter p as defined in Eq. (3.4). With this, the components of the model vector $\Delta\tilde{m}_p^i$ can be determined in a least-squares sense solving Eq. (3.8) via the Levenberg-Marquardt-algorithm:

$$\Delta\tilde{m}_p^i = ((G_{f,p}^i)^T G_{f,p}^i - \beta I_{f,p}^i)^{-1} (G_{f,p}^i)^T d_f^i \tag{3.12}$$

where β is the Levenberg-Marquardt damping parameter, and $I^i_{f,p}$ the unit matrix.
Following this, the subsurface parameters can be updated via:

$$\begin{aligned} m_p^i &= m_p^{i-1} + \frac{m_p^i - m_p^{i-1}}{m_p^{i-1}} m_p^{i-1} && (3.13) \\ &= m_p^{i-1}\left(1 + \Delta\tilde{m}_p^i\right) && (3.14) \end{aligned}$$

from which we can compute the new SESR via $S^i_f = \mathscr{F}(m^i_p)$.
The new residuals of the data can then be calculated as:

$$\tilde{d}_f = \frac{S_f^{obs} - S_f^i}{S_f^{i-1}} \tag{3.15}$$

where the quality of the fit is measured by the *rms*-value:

$$\Delta d_{rms} = \sqrt{\frac{\sum_f (\tilde{d}_f)^2}{n_f}} \tag{3.16}$$

We tried different damping factors for our inversion. We finally chose a damping factor of β=5 as this led to the smallest possible Δd_{rms} without resulting in unreasonable subsurface parameters. With β=5 the inversion was terminated after six cycles during which the *rms*-value Δd_{rms} decreased by 43%.
Fig. 3.10 shows the resolution-matrix for the first inversion. It reflects the result of the sensitivity analysis (section 3.4.3). Together with the salinity of the first layer the depth of the interfaces influence the SESR the most. While the sensitivity with respect to porosity and salinity decreases with depth, changes in the permeability seem to be insignificant. A lower β-value could enhance the influence of the permeability. Unfortunately, in our test run, this led to negative salinity values which are not realistic. We therefore decided not to further decrease β.
Tab. 3.4 lists the adjusted depths, porosities, permeabilities and fluid salinities of the inverted model as well as the resulting velocities and resistivities. All other input parameters remained constant and can be found in Tab. 3.5. The depth of the layers were changed by less than 6%. This is surprising as the sensitivity-analysis as well as the resolution-matrix suggested a high influence of the interface positions. Larger variations can be found for porosity, permeability and salinity. The largest adjustments to the porosity were made in the uppermost layer (-50%), while the permeability and salinity were changed most in the third layer (-39% and -78%). This is plausible, as the sensitivity analysis suggests that variations of permeability and salinity in the third layer affect mostly lower frequencies, which is where the biggest discrepancy between the observed and modelled SESR were found. When looking at the subsurface parameters that are not direct model inputs but calculated by the program one can see that the seismic velocities are mostly affected in the first layer (+22%), possibly due to the large porosity change. The highest variations can be found in the resistivity (over 100%). This is reasonable as the resistivity of the

layers has a direct impact not only on the creation of the IRs but also on the propagation of the electromagnetic waves due to damping- and velocity- effects.
Fig. 3.11 compares the observed SESR (line a) to the originally modelled SESR (line b) and the modelled SESR after the inversion (line c). Above 2 Hz the inverted SESR now represents the observed SESR very well. Below 2 Hz the model was also improved but deviations are still visible. These could possibly be minimised by adding another layer or using a more advanced inversion algorithm, which we leave to a future study.
In summary, we were able to show that in principle it is possible to fit modelled and measured SESRs via forward modelling and linearised inversion using simplifying subsurface models and assumptions. One has to consider though that IRs and therefore SESRs are influenced by different parameters in a variety of ways, which complicates the validation of the solution. However, if additional geophysical measurements can provide prior subsurface information (as for example seismic velocities, densities and interface depths), SESRs could be a suitable method to derive information about parameters like porosity or permeability in the upper subsurface.

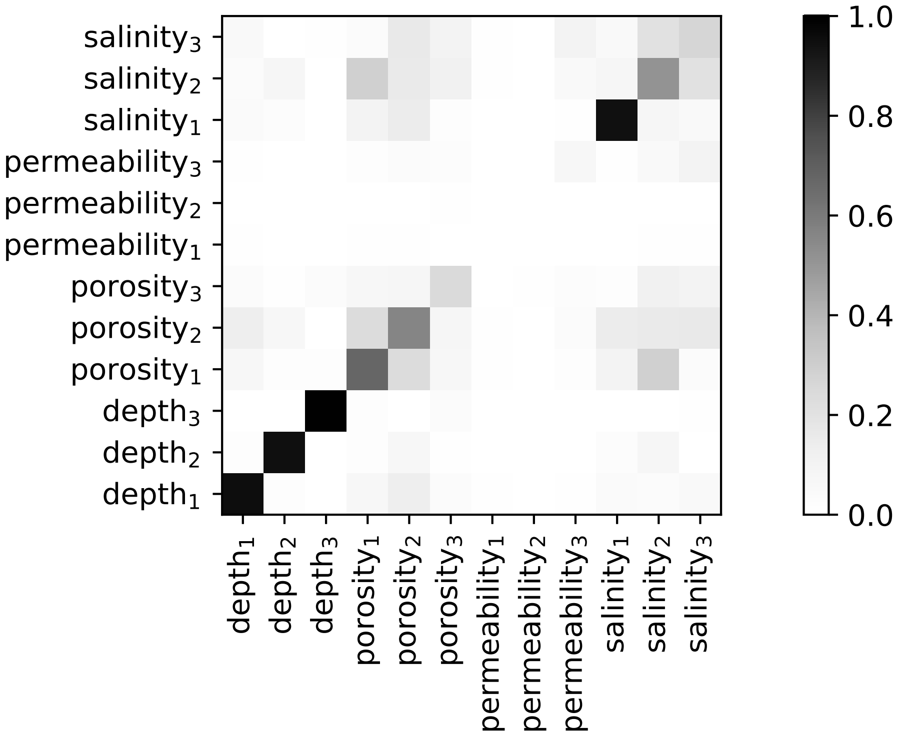

Fig. 3.10: *Resolution-matrix for β=5; The parameters' subscript number corresponds to the respective layer*

layer	1	2	3
depth [km]	0.096 (-4%)	0.297 (-1%)	2.64 (+6%)
porosity [%]	10 (-50%)	3.1 (-39%)	1.28 (-28%)
permeability [Darcy]	0.087 (-13%)	0.098 (-2%)	0.061 (-39%)
fluid salinity [mol/l]	0.012 (+26%)	0.010 (-26%)	0.003 (-78%)
*v_P [km/s]	2.18 (+16%)	2.62 (+2%)	3.49 (-0.3%)
*v_S [km/s]	1.22 (+22%)	1.56 (+3%)	2.01 (-0.5%)
*v_{EM} at 2 Hz [km/s]	36.2 (+40%)	70.1 (61%)	232.8 (81%)
*resistivity [Ωm]	263 (+97%)	979 (159%)	10835 (+228%)

Tab. 3.4: *Major properties and the change in % of the upper three layers after the inversion compared to the original model. Depth, porosity, permeability and fluid salinity are input parameters; velocities and resistivity are calculated by the program (marked with *).*

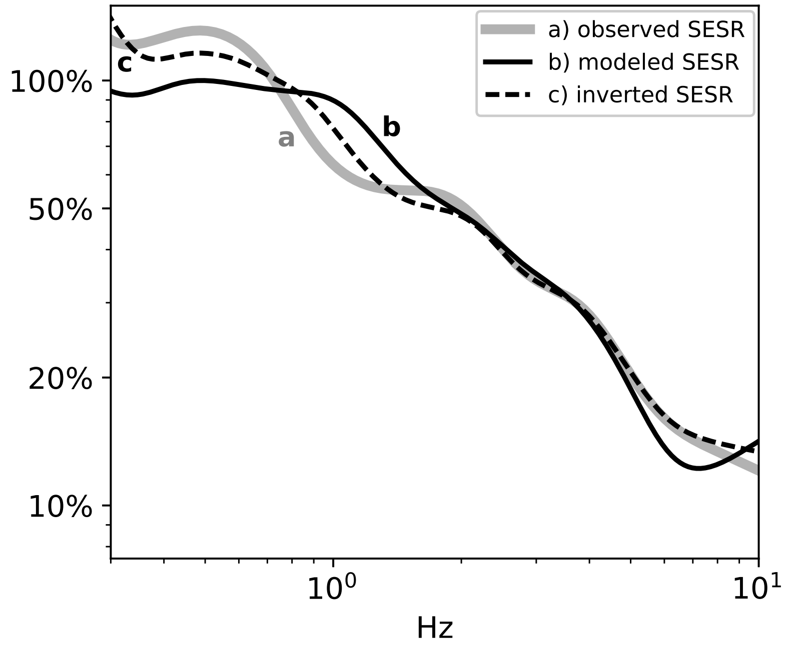

Fig. 3.11: *Comparison of the observed SESR (a) with the modelled SESR before (b) and after the inversion (c). The SESRs are normalised to the maximum of the modelled SESR (line b).*

3.5 Discussion

3.5.1 Importance of model geometry

In this paper we introduced SESRs as a concept to quantify the influence of IRs on SE signals and their spectra independently of the earthquake source spectrum. For the synthetic studies we decided to focus on the subsurface parameters of the shallow layers rather than the geometry of the model including for example layer depths or the source position. Nevertheless, these characteristics should not be neglected in a thorough investigation.

The sensitivity analysis (section 3.4.3) as well as the resolution-matrix of the inversion (Fig. 3.10) show that the depth of the third layer has a large influence on the SESRs even though the IRs that are excited at this interface do not (section 3.4.2). We therefore calculated the sensitivities of the SESR towards all layer depths as well as the depth of the source and found that each of these parameters can influence the resulting SESR. We suspect differing wavepaths to be a reason for this as they result in varying reflection and transmission angles in the upper layers. It is therefore important to have a realistic estimate of the subsurface layer structure or to include these parameters into the inversion.

Beside the layer and source depth we evaluated the importance of choosing the appropriate source orientation. For this we recalculated our model with a point force orientated in the y- instead of the z-direction. For both source orientations we then calculated the SESRs once including only the P-phase and once the whole wavetrain, resulting in four different SESRs (Fig. 3.12). When comparing the SESRs calculated from the P-phase only, no large differences can be seen between the SESRs computed from the vertical and the horizontal point force (compare lines a and b). Yet, when the whole wavetrain is included into the calculation, the deviation becomes obvious (compare lines c and d). We therefore infer from Fig. 3.12 that if one restricts oneself to the P-phase for the SESR calculation, the source orientation can be neglected. If on the other hand, the whole wavetrain is used, the source model has to be taken into account.

Lastly we verified whether the source strength has an influence on the SESRs. At least for our calculations this did not seem to be the case. It seems as if the IRs, the coseismic and the seismic field all depend on the source strength equally, which means that the difference gets cancelled out when the ratio is calculated.

3.5.2 SESRs as a monitoring tool?

A possible application of SESRs derived from earthquake data may be the attempt to observe changes of subsurface parameters over time. This raises the question of the accuracy, with which SESRs can be expected to be determined, in relation to the magnitude of possible changes of the SESR by variation of relevant subsurface parameters. A general answer clearly requires an extensive numerical investigation. However, a first guess may be derived already from the results of the present study. The SESRs calculated from the field data recorded at station PB09 (Fig. 3.4d) deviate from the average SESR about roughly 15%. This value may be seen as an order of magnitude of what may be expected under favourable noise conditions (cf. Dzieran et al. (2019) regarding the influence of noise on the detectability of SESRs). It defines the order of magnitude which needs to be exceeded by SESR variations caused by varying subsurface parameters. From the sensitivity analysis (Fig. 3.9) we can conclude that the porosity or salinity would have to change by more than 15% to be reliably identifiable and the permeability should undergo changes of at least two decades. While these values appear rather large, some scenarios can be thought of that might lead to said changes, as for example crack openings or sudden fluid intrusions in tectonically or volcanically active environments. Clearly, it may be difficult to distinguish whether one single parameter or a combination of parameters is responsible for possibly observed changes in the SESR.

3.5.3 Limitations of SESR concept

The SESR concept is based on the assumption that the coseismic SE field and the ground acceleration are proportional (section 3.2). In that case the spectra of the coseismic field and the seismic acceleration should also be proportional and a frequency dependency should only be caused by IRs. During our computations however we found that for small epicentral distances this assumption might not hold. For epicentral distances smaller than the source depth a frequency dependent behaviour could be observed in the SESRs even in the case of a purely coseismic field. We believe that conversions from P- to S-energy (and the other way round) at the free surface might be a possible reason, but further investigation is definitely necessary.

An additional problem might be the noise level on the data. The noise could influence the seismic and electric spectra differently which can then lead to an additional frequency dependent disturbance of the SESR that is not caused by IRs. A further factor that influences the SESRs could be the sensor coupling with the subsurface. We therefore highly recommend to check (for example through modelling) whether a proportionality between the seismic and electric noise fields can be assumed before evaluating SESRs towards the influence of IRs.

3.5.4 Future prospects

In this paper we introduced SESRs as a new concept. We are aware that before being able to reliably use SESRs to study the subsurface a lot more research needs to be conducted in both numerical studies and field applications. Data quality and the influence of noise for example needs to be investigated as well as possible model ambiguities.

By rotating the data into their principal component we have reduced the problem to one dimension. One could however also consider a vectorial approach to calculate an SESR tensor for considering 3D effects and anisotropy.

Furthermore one could think about applying SESRs not only to earthquake studies but investigate whether the method can be transferred to active source seismoelectric exploration applications as well.

In any case, we are confident that SESRs can be used to help to determine hydrologically relevant subsurface parameters in situ.

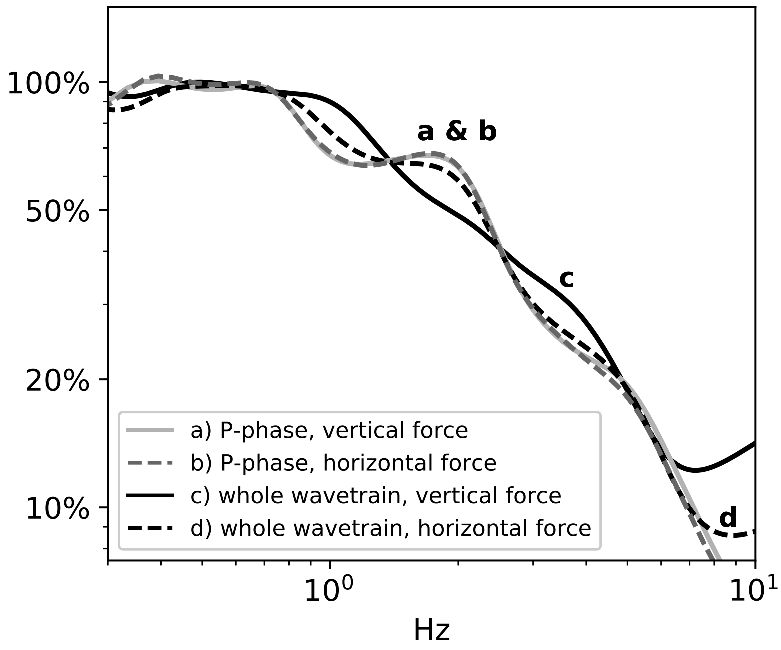

Fig. 3.12: *SESRs calculated from the P-phase (lines a and b) and the whole wavefield (lines c and d) for a vertical and a horizontally orientated force (lines a and c and lines b and d).*

3.6 Conclusion

To quantify the influence of IRs on SE signals caused by earthquakes and their spectra we introduced the concept of SESRs. Analysis of both numerical and field data showed that the presence of IRs causes a frequency dependency of the ratio of the electric and seismic spectra. In particular, the field data analysis showed that the form of frequency dependence of the SESRs is site specific: It depends mainly on the hydrogeophysical structure underneath the recording station. Numerical modelling showed that the IRs influencing the SESR are created in the upper few hundred meters of the subsurface. Considering a geologically realistic range of parameter variation, we found that changes in salinity and porosity may influence SESRs more than the hydraulic permeability. The variation of the SESRs caused by the variation of different subsurface parameters is frequency dependent, too, in a complicated way. Therefore, inversion algorithms need to be applied for recovering subsurface parameter variations from SESRs. Based on a given regional seismic crustal model and realistic hydrogeophysical parameters we showed the observed SESRs can be reproduced by forward modelling and linearised inversion.

Acknowledgements First of all, we would like to thank the reviewers for their constructive comments. The field data were acquired in the framework of the Integrated Plate boundary Observatory Chile Project (IPOC). The authors would like to thank Jaime Araya Vargas for making the MT-data available. The data used in this paper can be requested from the authors. The station map (Fig. 3.3) was created with Generic Mapping Tools (GMT) software (Wessel et al., 2013) and the data analysed with ObsPy (Krischer et al., 2015). The first author is grateful for funding through a scholarship of the Christian-Albrechts-Universität zu Kiel ('Landesgraduiertenstipendium').

3.A Appendix

3.A.1 Halfspace model specifications

In this section we provide the computational settings used to calculate the spectra and snapshots illustrated in section 3.2, Fig. 3.2.

For the calculations we used the code provided by Garambois and Dietrich (2002), that is described in section 3.4.1. The subsurface model consists of two layers. The upper and lower layer have the properties of layers 1 and 2, respectively, that are described in Tabs 3.3 and 3.5. The source is a vertical point force that is located 5 km beneath the layers' interface.

The spectra shown in Figs. 3.2a and b were calculated for a receiver at 50 km epicentral distance from the source. The receiver was placed at a free surface 100 m above the interface. Only the fast P-wave, coseismic field and IRs were considered in the calculation. The seismic and SE spectra were calculated for a timelength of 204.8 seconds over 4096 samples, resulting in a sampling rate of 20 Hz. The spectra were then smoothed with the Konno-Ohmachi smoothing filter and divided to calculate the SESRs in Fig. 3.2c.

The snapshots shown in Figs. 3.2d and e were calculated for a timelength of 40.96 seconds over 2048 samples, resulting in a sampling rate of 50 Hz. 101 receiver were evenly distributed in the horizontal direction between 40 km and 60 km offset, resulting in a spacing of 200 m. In the vertical direction 51 receiver were placed between 0 km (source depth) and 10 km, resulting also in a spacing of 200 m. For clarity, the free surface reflections were omitted. A source-wavelet in the form of

$$w(t) = sin(\pi \frac{t}{T_0}) - \frac{1}{3} sin(3\pi \frac{t}{T_0}) \tag{3.17}$$

was applied to the data in the time domain, with T_0 = 1 sec. The results presented in Fig. 3.2d and e correspond to the time of 20 seconds after nucleation.

3.A.2 Model parameters

Table 3.5 lists the input parameters used to calculate the modelled SESRs. Parameters marked with (*) were calculated by the program. The corresponding equations can be

found in Garambois and Dietrich (2002) and Warden et al. (2013).
The modelling code is mainly intended for near surface applications. To be able to model the resistivities suggested by Araya Vargas (2016), high salinity values had to be chosen for greater depths. Using the Zeta-potential formula $\zeta = 0.008 \cdot 0.026 \cdot log_{10}(Salinity)$ of Pride and Morgan (1991), that is implemented in the modelling code, leads to an unrealistically high zeta potential value. Jaafar et al. (2009) suggested that for high salinities (above 0.2 mol/l) the zeta-potential remains constant at around -0.02 V. We therefore used this value for the zeta potential of layers 4 to 8.

layer	1	2	3	4	5	6	7	8
depth [km]	**0.1**	**0.3**	**2.5**	7	22	37	50	500
porosity [%]	**20**	**5**	**1**	0.5	0.1	0.1	0.1	0.1
saturation [-]	0.75	1.0	1.0	1.0	1.0	1.0	1.0	1.0
permeability [Darcy]	**0.1**	**0.1**	**0.1**	0.01	0.01	0.01	0.01	0.01
solid bulk modulus [GPa]	8.2	8.2	15.9	54.7	63.0	72.8	78.1	116.0
solid shear modulus [GPa]	5.9	5.9	9.8	33.1	37.9	43.8	46.9	69.7
fluid bulk modulus [GPa]	2.27	2.27	2.27	2.27	2.27	2.27	2.27	2.27
air bulk modulus [kPa]	100	100	100	100	100	100	100	100
consolidation parameter [-]	5	2	2	2	2	2	2	2
fluid viscosity [$Pa \cdot s$]	0.001	0.001	0.001	0.001	0.001	0.001	0.001	0.001
air viscosity [$Pa \cdot s$]	1.80E-05	1.8E-05	1.8E-05	1.8E-05	1.8E-05	1.8E-05	1.8E-05	1.8E-05
solid density [kg/m^3]	2194	2194	2312	2710	2767	2831	2864	3256
fluid density [kg/m^3]	1000	1000	1000	1000	1000	1000	1000	1000
air density [kg/m^3]	1	1	1	1	1	1	1	1
salinity [mol/l]	**0.0095**	**0.014**	**0.013**	0.3	1.0	1.0	1.0	1.0
temperature [K]	300	300	300	320	450	450	600	1000
fluid permittivity [-]	80	80	80	80	80	80	80	80
solid permittivity [-]	4	4	4	4	4	4	4	4
cementation exponent [-]	1.3	1.3	1.3	1.5	1.5	1.5	1.5	1.5
*v_P [km/s]	1.87	2.57	3.5	6.0	6.4	6.8	7.0	8.0
*v_S [km/s]	1.00	1.51	2.02	3.47	3.69	3.93	4.04	4.62
*v_{EM} at 2 Hz [km/s]	25.8	43.5	128.7	71.4	130.8	130.8	130.8	130.8
*density [kg/m^3]	1905	2134	2299	2701	2765	2829	2862	3254
*zeta potential [V]	-0.045	-0.04	-0.041	-0.02	-0.02	-0.02	-0.02	-0.02
*fluid conductivity [S/m]	0.088	0.13	0.12	2.78	9.28	9.28	9.28	9.28
* bulk resistivity [Ωm]	134	378	3302	1016	3409	3409	3409	3409

Tab. 3.5: *Input parameters to calculate SESRs in section 3.4. Parameters marked with (*) were computed by the program. The **bold parameters** were changed to adjust the modeled SESR to the measured SESR and altered in the inversion.*

4 Seismoelectric monitoring of aquifers using local seismicity – a feasibility study

This chapter is based on the paper 'Seismoelectric monitoring of aquifers using local seismicity – a feasibility study' published in Geophysical Journal International.
Citation: Dzieran, L., M. Thorwart, and W. Rabbel, 2020: 'Seismoelectric monitoring of aquifers using local seismicity — a feasibility study'. Geophysical Journal International, 222 (2), 874-892, doi:10.1093/gji/ggaa206.

Summary Seismoelectric (SE) signals, accompanying seismic wave fields radiated from earthquakes, can be observed on records of magnetotelluric stations. Assuming that these SE signals are generated by electrokinetic coupling we investigate whether they can be used as a 'pore-space monitoring'-tool. Regarding future field experiments we analyse synthetic SE waveforms calculated for a fully saturated base model consisting of five layers overlying a half-space, resembling the conditions of the Armutlu Peninsula (Turkey). This example site stands for a location with near-surface thermal aquifers exposed to tectonic stress and significant micro-seismicity. As expected, coseismic SE waves arrive simultaneously with the seismic onsets whereas interface response SE waves (IRs) arrive (shortly) before the generating seismic onsets. Therein, so-called evanescent IRs show a similar moveout as seismic phases and so-called radiation IRs travel with zero slowness. We found that the influence of IRs on the overall SE signal can be identified by envelope analysis of SE time series and by seismoelectric spectral ratios (SESRs) in the frequency domain. For a sensitivity analysis we added an extra layer to the base model with differing porosity, porefluid salinity and permeability values. At near-epicentral distances both trace-envelopes and SESRs are sensitive to the porosity and porefluid salinity changes in the simulated near-surface aquifer. The SESRs' and SE envelopes' amplitudes vary in the order of up to some 10% in response to porosity and salinity increases of factor 2 and 100, respectively. In contrast, a decrease of the permeability value by the factor 100 leads to an SESR amplitude variation of less than 1 to 10% percent. In the Armutlu model the largest relative changes of SE signals occur near the epicentre where the ratio between coseismic and IR amplitudes is close to 1. For 1 to 6 km deep source depth the SE detection swell at the earth surface is in the order of magnitude 2 to 3, depending on the ambient electromagnetic noise and hypocentral distance. This estimate assumes that SE signals are recorded with standard magnetotelluric stations. It can improve if array methods are applied.

4.1 Introduction

When seismic waves propagate through the subsurface they can generate electromagnetic (EM) waves by electrokinetic coupling. This phenomenon, commonly known as the electrokinetic effect, has periodically been investigated since the mid of the last century (e.g. Ivanov, 1939; Frenkel, 1944; Thompson and Gist, 1993). In 1994 Pride established a set of macroscopic equations for the coupling between the seismic and EM waves in a fully saturated medium based on Biot's theory. This provided the basis for further investigations on the electrokinetic effect (e.g. Haartsen and Pride, 1997; Jardani et al., 2010; Ren et al., 2010; Schakel et al., 2011; Grobbe and Slob, 2016). An overview on the history of SE investigations can be found, for example, in Revil (2015), chapter 1.6. A review on electrokinetically induced seismoelectrics, electroseismics and seismomagnetics for Earth sciences was published by Jouniaux and Zyserman (2016).
Since Thompson and Gist (1993) recorded a seismoelectric (SE) interface response (IR) from a 300 m deep gas-water interface many more field experiments have been conducted where IRs were successfully identified (e.g. Russell et al., 1997; Garambois and Dietrich, 2001; Dupuis et al., 2007; Strahser et al., 2011; Rabbel et al., 2020). In analogy to the P-to-S and S-to-P wave conversion occurring at seismic interfaces these IRs are sometimes called SE conversions. SE signals have also been observed during earthquakes (e.g. Matsushima et al., 2002; Huang, 2011; Dzieran et al., 2020), although a direct identification of IRs has not been reported, yet.

Interrelations of ambient stress, fluid pressure and the formation of fractures and microfractures have been conceptually established since the 1980s (e.g. Sibson, 1981; Scholz, 2019, and the references therein). Since then many hydrogeological studies reporting on changes of the level, flow and chemistry of ground water were published for different tectonically active regions (see e.g. Hartmann and Levy (2005) for a general overview, Süer et al. (2008) for an overview of the North Anatolian Fault or Skelton et al. (2014) on Iceland). Changes of the level and radon content of groundwater have even been confirmed as earthquake precursors (Wyss, 1997; Wyss and Booth, 1997; Woith, 2015). Since the early 1990s an increasing number of field, laboratory and theoretical studies have stated the induction of permeability changes by oscillatory and permanent stress changes (see Manga et al. (2012) for a review; other examples are Rojstaczer and Wolf (1992), Rojstaczer et al. (1995), Charmoille et al. (2005), Elkhoury et al. (2006) or Shi and Wang (2014)). Recently, Zhang et al. (2019) succeeded in estimating hydraulic permeability changes of aquifers caused by the great Tohoku earthquake. Still, concretizing and monitoring changes in the pore space on-site has remained a challenge.

Results from theoretical and applied SE field studies suggest that recordable SE signals are at least in principle sensitive to hydrological parameters, especially to porosity, hydraulic permeability and the salinity of pore water (e.g. Garambois and Dietrich, 2001, 2002). Jardani et al. (2010), for example, presented a stochastic joint inversion approach of seismic and SE data, which was able to recover the permeability of a synthetic formation with an accuracy of one order of magnitude. Zyserman et al. (2016) numerically investigated the sensitivity of SE signals excited by SH-waves towards different soil compositions and Monachesi et al. (2018) analysed the same signals' sensitivity towards porosity, fluid viscosity and density. Whereas porosity and salinity could also be assessed indirectly by combining geoelectric and seismic sounding, for example, the principle attractiveness of SE surveying lies in that it combines ab initio a sensitivity to hydraulic subsurface parameters with seismic resolution.

In this study we focus on passive SE measurements. Especially for tectonically active regions the question can be asked if these measurements might be sensible enough to record temporal changes of subsurface hydrologic parameters. If so, SE sounding could develop into a monitoring tool to improve the understanding of hydraulic effects in tectonic deformation.

Various numerical studies have been published regarding SE sounding (e.g. Garambois and Dietrich, 2002; Warden et al., 2013; Ren et al., 2015; Gao et al., 2016; Ren et al., 2018). However, most of these studies are based on full or half-space models with a single interface, designed to investigate basic concepts of SE wave propagation. Moreover, they address mainly artificial-source field and laboratory acquisition settings. Whereas artificial-source SE soundings rely on a reflection-type response, a 'passive' SE monitoring will primarily record transmitted wave fields from earthquake sources at depth.

By analysing field and synthetic SE data Dzieran et al. (2019, 2020) have shown that the SE field recorded at MT stations from local seismic events can be understood as a site-specific response function. In the present study, with regard to evaluating SE sounding as a possible 'pore-space monitoring tool', we investigate the SE responses of multi-layer models resembling the subsurface conditions of a concrete site, to which SE monitoring might be applicable. For the background setting of our modelling study we chose the Armutlu Peninsula in Turkey, but the results of our calculations can easily be transferred to other locations on earth.

The objectives of our study are to obtain estimates on

- which traveltimes and amplitude strengths can be expected for different sorts of SE arrivals in the time and frequency domain for frequently occurring local seismic events?
- which parts of the SE signals carry information on which structural and hydrological parameters?
- at which epicentral distances would monitoring stations need to be placed to obtain optimum results?
- which event magnitudes would be required in order to record SE events of a signal/noise-ratio allowing a reliable monitoring, and how frequently do events exceed this threshold?

To obtain these estimates this paper is divided into six sections: First we will give a brief introduction to the main observables of SE wave propagation (section 4.2) and the seismo-tectonic setting of the Armutlu Peninsula (section 4.3). Then, we provide details of the modelling process and describe the main features of a base-model that is used for all calculations in this paper (section 4.4). We analyse the synthetic signals obtained from this model in section 4.5. In section 4.6 we present different scenarios simulating changes of hydrologic parameters by modifications of the base-model and in section 4.7 we investigate whether the computed amplitudes could be identified in real field data. Last, we discuss the above raised objectives with regards to potential field experiment (section 4.8) and draw a final conclusion (section 4.9).

4.2 Observables of seismoelectric wave propagation

4.2.1 SE wave types

In the SE field three different types of EM waves can be found: coseismic waves, interface responses (IRs) and an EM wave that is directly radiated from the source.

Coseismic waves are coupled to the seismic wavefield and therefore travel with the same velocity. Their amplitudes are proportional to compressional portions of ground acceleration (Garambois and Dietrich, 2001). SE records of earthquakes show also signals that apparently accompany S-wave arrivals. However, they are not caused by the shear movement as such but rather by volumetric deformation resulting from S-to-P conversion especially at the free surface. As coseismic waves are directly linked to their seismic counterparts, they only carry information related to the immediate vicinity of the recording station.

IRs are excited when the electric current-balance binding the coseismic EM wave to the seismic compressional field gets disturbed. This is the case at layer interfaces across which hydraulic, electrical or seismic rock properties change. Sometimes IRs are also called ‘converted signals’ as in general, all heterogeneities larger than about 1/5 of the seismic wavelength could generate electromagnetic disturbances.

Once generated, IR waves do not depend on the seismic field any more. They travel with the speed of EM waves and can therefore be detected earlier than the seismic and coseismic signals they were generated from. IRs are of great interest for the hydraulic characterisation of the subsoil, since they are sensitive to porosity, permeability, fluid salinity and fluid viscosity (Garambois and Dietrich, 2002) and can, contrary to coseismic signals, provide information about deeper layers. However, due to their small amplitudes IRs are hard to identify in the SE wave field.

Following the terminology of Ren et al. (2018) we distinguish between two types of IRs in this paper. Depending on the seismic wave’s incident angle θ, either a radiation IR (rIR) or an evanescent IR (eIR) can be created at an interface. If $\theta \leq \theta_c$ an rIR is excited, with $\theta_c = arcsin(v_{seis}/v_{em})$ being the critical angle and v_{seis} and v_{em} the respective velocities of the seismic and the EM wave. If $\theta > \theta_c$, the resulting EM wave is an eIR. Since usually $v_{em} >> v_{seis}$, θ_c is very small in most cases. Therefore rIRs are only created at points directly above the earthquake’s source. Waves with a larger incident angle give rise to eIRs. They are characterised by a moveout similar to that of the seismic waves, which is why they are also known as ‘quasi-coseismic’ signals (Butler et al., 2018). According to simulations by Ren et al. (2018), eIRs are able to exceed rIR- and coseismic amplitudes in the low frequency range around 10 Hz. As this frequency range is not unusual for passive measurements, eIRs could have a significant effect on the overall earthquake generated SE wavetrain.

Last but not least, a comparably weak EM wave is generated at the origin time of the earthquake due to nucleation processes (Mahardika et al., 2012; Gao et al., 2013). However, the amplitudes of this wave are so small that its detection appears to be very difficult in passive SE field surveys. We will therefore not further discuss this type of EM wave in this paper.

4.2.2 Seismoelectric spectral ratios (SESRs)

Besides analysing SE traces in the time domain we calculate seismoelectric spectral ratios (SESRs) in our study as they enable the analysis of time-lapse SE records independent of the varying seismic source time functions (Dzieran et al., 2019).

SESRs are the ratio of the SE spectrum $E(\omega)$ and the spectrum of the seismic acceleration $\ddot{U}(\omega)$. Since $E(\omega)$ and $\ddot{U}(\omega)$ are both obtained from the same earthquake, they are the result of a multiplication of the respective Green's functions $GE(t)$ and $G\ddot{U}(t)$ with a common source time function $SF(t)$. Forming the ratio, the source function is cancelled out leading to:

$$SESR(\omega) = \frac{E(\omega)}{\ddot{U}(\omega)} = \frac{GE(\omega)\cdot SF(\omega)}{G\ddot{U}(\omega)\cdot SF(\omega)} = \frac{GE(\omega)}{G\ddot{U}(\omega)} \tag{4.1}$$

Since coseismic signals are proportional to seismic acceleration, the respective Green's functions and their spectra should follow the same frequency trend. Consequently, a SESR that is calculated from a purely coseismic spectrum should be frequency independent. Vice versa, any frequency dependency that is seen in the SESR should result from IRs.

It is important to notice that this conclusion is only valid if the coseismic signals are truly proportional to the seismic acceleration. This is only the case for compressional signals, which, in case of field data, are hard if not impossible to separate from other signal-parts. Nevertheless, IRs can still be expected to influence the shape of the SESRs in a significant way, which is worth investigating. For further details on SESRs see Dzieran et al. (2019).

4.3 An example location for a hypothetical SE experiment

4.3.1 Seismo-tectonic setting of the Armutlu Peninsula (Marmara Region, Turkey)

We chose the Armutlu Peninsula in Turkey as a location for a hypothetical field experiment. The peninsula is an east-west trending mountain range that is located on the eastern Marmara Sea between the northern and southern branches of the North Anatolian Fault (Yılmaz et al., 1995). The Marmara Region is considered to be one of the most seismic active areas in Turkey. It was struck among others by the Mw 7.4 Izmit (Koaceli) earthquake in 1999 (Barka et al., 2002), the rupture of which terminated offshore the northeastern coast of Armutlu in the Marmara Sea (Baris, 2002; Çakir et al., 2003). The Armutlu Peninsula is considered a horst zone in an active pull-apart environment under NNE-SSW extension (e.g., Kinscher et al., 2013). It shows clustered local seismicity and

several geothermal areas spread out across the island. The hottest thermal sources can be found in the northern and western parts of the Peninsula with surface temperatures of up to 70° C (Tunc et al., 2011). In 2014 intense seismic swarm activity started close to the Yalova hydrothermal area (Yavuz et al., 2015). Also seismically induced pore pressure variation were detected at geothermal areas of the region (Woith et al., 2014).
The abundance of earthquakes shallower than 15 km in connection with tectonically affected hydrothermal springs located in a not too densely populated area were the reason to select the Armutlu Peninsula as an example site to investigate the applicability of SE monitoring based on earthquake signals.

4.3.2 Seismicity of Armutlu Peninsula

To get a quantitative overview on the seismicity on the Armutlu Peninsula, we evaluated data entries from the ISC catalogue (International Seismological Centre, 2015) of the years 2001 to 2016. For this time range about 2450 events are listed in the catalogue with epicenters between 28.7° to 29.32° East and 40.4° to 40.69° North. Fig. 4.1 shows the location of these epicenters. The cumulative magnitude distribution calculated from this data shows that on average about 60 events can be expected each year with a magnitude of 2.5 or greater (Fig. 4.2a). This accounts for a repetition rate of ca. 5 earthquakes with a magnitude greater than 2.5 per month. The depth distribution shows that the hypocenters of the events rarely lie deeper than 20 km and the majority of hypocenters can be found between 5 and 10 km (Fig. 4.2b).
Based on this background information, we decided to numerically investigate the SE response to an earthquake located in 6 km depth, which is in the seismically active zone. According to the magnitude-distance-threshold developed by Dzieran et al. (2020), there is a good chance to observe SE signals on MT-stations from earthquakes with magnitude 2 if the station is not located further than 7 km away from the earthquakes hypocenters. We therefore limited the epicentral range of the synthetic seismoelectrograms to 10 km. Further information on the modelling process is provided in the next section.

4.4 Numerical modelling of seismic and seismoelectric waves

The synthetic data shown in this paper were calculated with a Fortran code developed by Garambois and Dietrich (2002). The code, which is based on Biot's Theory and the general reflectivity method, was extended by Warden et al. (2013) for unsaturated media. It calculates the wave propagation of the seismic, seismoelectric and seismomagnetic fields for a stratified subsurface model. The coordinate system is Cartesian (x,y,z) with z pointing downwards. The source is located at (0,0,z) and can either be a point force in a single direction or an explosion. As the code calculates the reflection and transmission coefficients for all wave-types and interfaces individually, it is possible to suppress selected wave-types as, for example, IRs or S-waves.
We used the code to calculate the Green's functions of the seismic and SE field from a

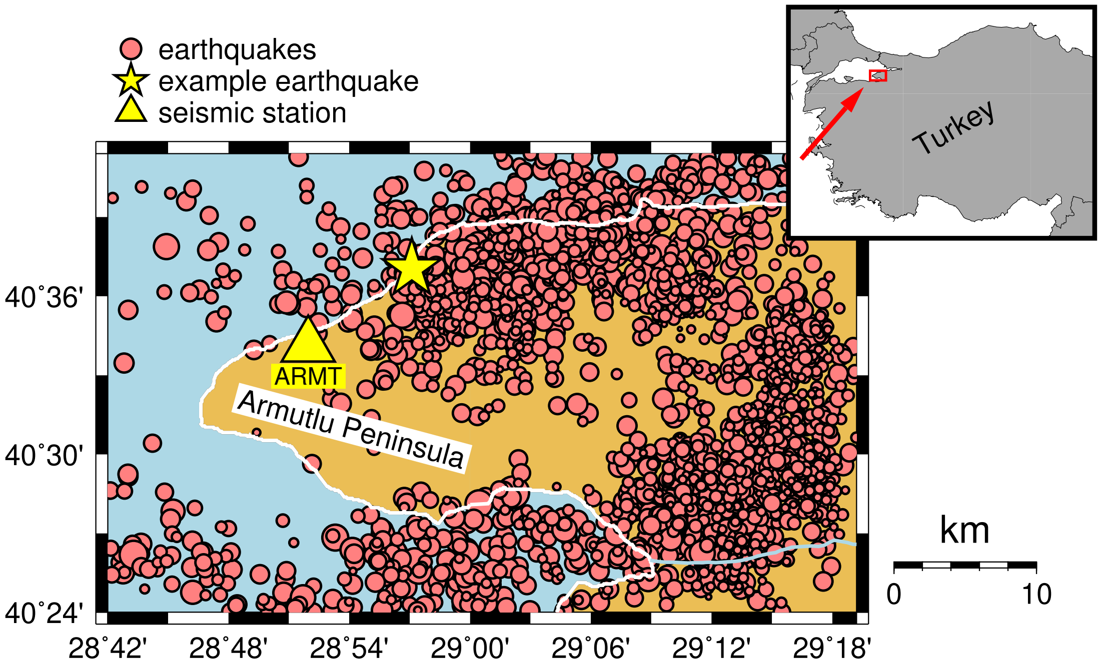

Fig. 4.1: *Location of seismic events on the Armutlu Peninsula (Turkey) listed in the ISC catalogue (International Seismological Centre, 2015) for the years 2001 to 2016. The size of the circles is proportional to the events' magnitudes. The location of the earthquake (star) and seismic station (triangle) discussed in section 4.7.1 are shown.*

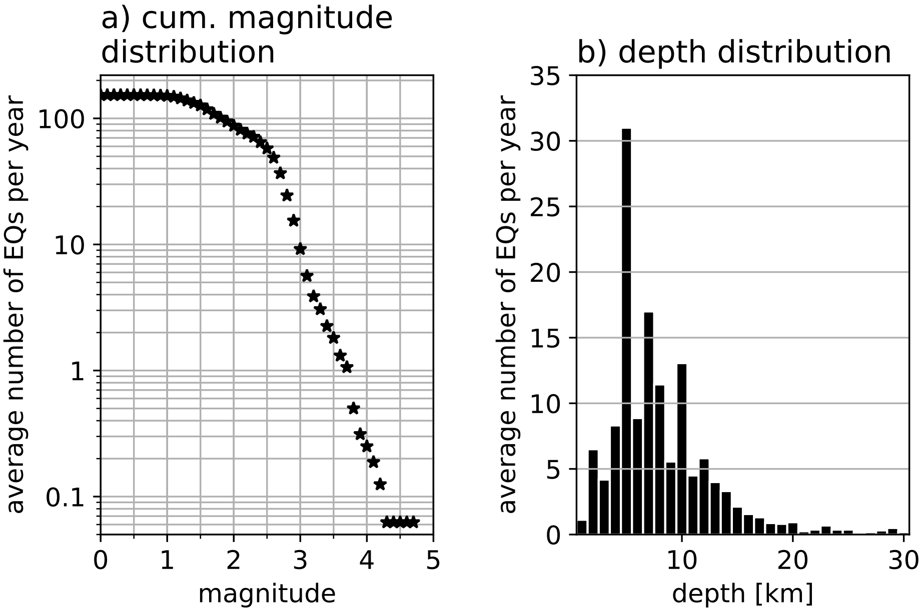

Fig. 4.2: *(a) Cumulative magnitude distribution and (b) depth distribution of earthquakes per year around the Armutlu Peninsula derived from events listed in the ISC catalogue for the years 2001 to 2016 (International Seismological Centre, 2015).*

vertical point force placed in 6 km depth. The results were computed for 51 receivers that were, starting from the epicenter, evenly spaced over 10 km in x-direction, leading to a minimum spacing of 200 m. The depth of the receivers was set to 10 cm, which corresponds to a typical electrode depth.

The responses were calculated for a recording time-length of 20.48 s after origin time resulting in 2048 samples per trace at a sampling rate of 100 Hz.

Our basic subsurface model consists of 5 layers reaching down to 10 km depth with a following half space. The seismic properties were chosen after velocity models derived by Karabulut et al. (2003) and Bekler and Gurbuz (2008) for the Armutlu Peninsula. They consist of typical crustal velocity values, with a low velocity zone between 5 and 10 km depth. The electric resistivity structure is based on results obtained by magnetotelluric sounding of Tank et al. (2003) for the same area. The values lie between 1000 and 3500 Ωm. The major properties of the subsurface model are listed in Tab. 4.1. The complete list of input parameters can be found in the Appendix.

The synthetic SE records of the base-model are analysed in section 4.5. For the sensitivity analysis in section 4.6 the base-model was slightly modified. Further information will be given in that section.

From the code of Garambois and Dietrich (2002) we obtained the Green's functions of the SE field and the corresponding seismic displacement. To receive the seismic acceleration, the spectrum of the seismic Green's function was multiplied twice with $2\pi\omega i$. The seismic and SE waveforms were then computed by transforming the Green's functions into the time domain via an inverse Fast-Fourier-Transformation (FFT). A wavelet in the form of

$$w(t) = sin(\frac{\pi t}{T_0}) - \frac{1}{3}sin(\frac{3\pi t}{T_0}) \tag{4.2}$$

for $0 \leq t \leq T_0$ was applied to the data, with a peak frequency of T_0 = 15 Hz. Finally a lowpass-filter of 42.5 Hz (85% of the Nyquist-frequency) was used to suppress numerical noise at the end of the trace.

To obtain the SESRs, the Green's functions of the SE field and seismic acceleration were smoothed with the Konno-Ohmachi smoothing filter, for which the bandwidth is constant on a logarithmic scale (Konno and Ohmachi, 1998). After that, the ratio of the SE and the seismic spectrum was calculated.

4.5 Waveform and amplitude of IR arrivals for the base-model

4.5.1 IRs in the time domain

In this section we analyse the SE response to the base-model in the time and frequency domain. Fig. 4.3 shows seismic and SE trace-gathers computed for the base-model described in section 4.4. Figs 4.3a to c show the seismic acceleration, the SE field and IRs that are excited at subsurface interfaces only (that is excluding the free surface on top of the model). The gathers consist of 10 traces each with a spacing of 1 km resulting in a maximum epicentral distance of 10 km. In the gathers the onset times of rIRs and eIRs

layer	1	2	3	4	5	6
depth [km]	0.5	1.0	2.0	5.0	10.0	>10
porosity [%]	5.0	1.0	0.1	0.1	0.1	0.1
permeability [Darcy]	0.1	0.1	0.1	0.1	0.1	0.1
fluid salinity [mol/l]	0.005	0.04	1.0	1.0	1.0	1.0
*v_P [km/s]	3.32	3.96	5.29	5.99	5.49	6.39
*v_S [km/s]	1.85	2.27	3.05	3.45	3.17	3.69
*v_{EM} at 15 Hz [km/s]	200	201	359	359	359	359
*resistivity [Ωm]	1060	1070	3410	3410	3410	3410

Tab. 4.1: *Main properties of the layers in the base-model. Depth, porosity, permeability and fluid salinity are input parameters; velocities and resistivity are calculated by the program (marked with *).*

excited by the arrival of the direct P- and S-waves at the uppermost interface in 500 m depth are marked. Additionally the arrival time of the direct P- and S-wave at the surface are highlighted. All traces are normalised to the maximum amplitude of the gather they are belonging to.

In the seismic gather (Fig. 4.3a) we can clearly identify the direct P- and S-arrivals as well as multiple reflected and converted phases. In the SE gather (Fig. 4.3b), we can recognise phases arriving at the same time as the seismic onsets. We therefore conclude that these are coseismic signals. That we cannot identify these arrivals in the IR-gather confirms this conclusion (Fig. 4.3c). Instead signals appear a few milliseconds before the arrival times of the (co)seismic signals. These signals show a moveout similar to the (co)seismic signals, which is why we identify them as eIRs. The peak frequency of the eIRs decreases with increasing distance, which fits the decay behaviour predicted by Ren et al. (2018). The rIR should be recorded on all traces at the same time. We cannot identify this signal in the data-gather. However, if we zoom in on the expected arrival time and normalise each trace to its individual maximum, peaks become visible (Box ci in Fig. 4.3c). This shows that a rIR is excited and recorded, but its amplitudes are too small to be visible next to eIRs without special amplification.

It is generally hard to identify IRs in the SE-gather (Fig. 4.3b). We can only observe coseismic signals, whose amplitudes seem to increase with distance. As the amplitudes of the eIRs (Fig. 4.3c) decrease with distance, we conclude that the chance to observe IRs next to coseismic signals should be best in close proximity to the epicenter. Figs 4.3d to f therefore show the same trace-gathers as Figs 4.3a to c, but instead of 10 km the furthest trace is now located only 2 km away from the epicenter, leading to a spacing of 0.2 km.

In the seismic gather (Fig. 4.3d) we can again identify P- and S-phase arrivals, but in the SE gather we now observe eIRs before the coseismic arrivals of the direct P-phase (Fig. 4.3e). rIRs cannot clearly be identified, as their amplitudes overlap with the eIRs' amplitudes. We can also identify arrivals before the coseismic S-phase. However it is hard to distinguish whether these amplitudes are caused by IRs or by coseismic waves belonging to reflected and refracted seismic waves.

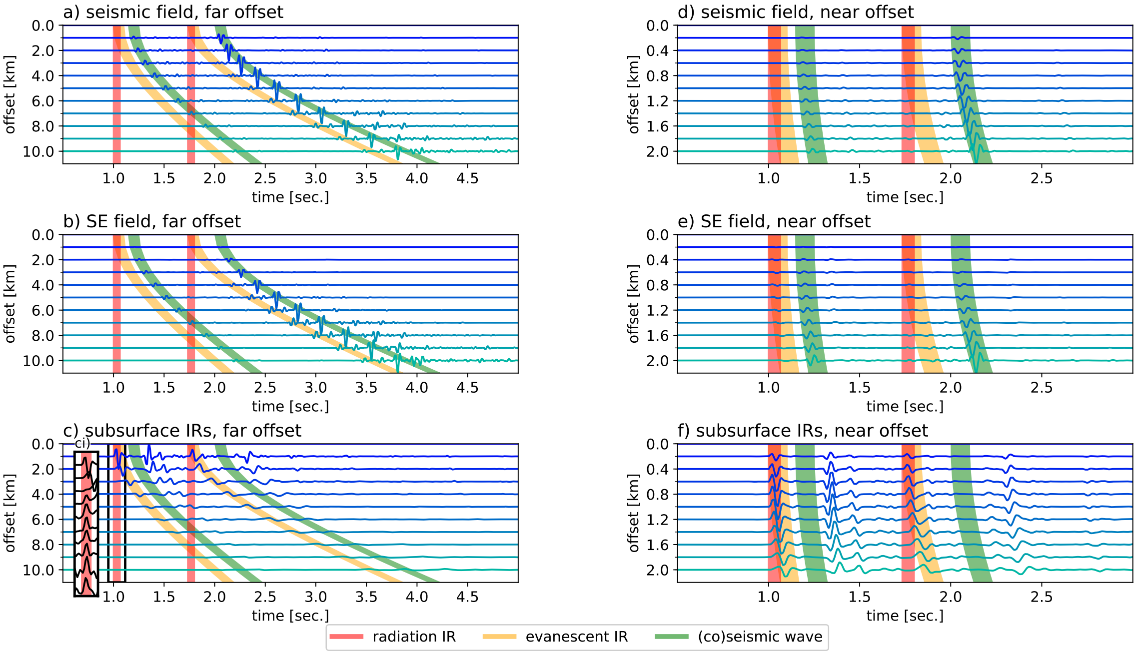

Fig. 4.3: *Seismic and SE traces generated by the base-model over increasing epicentral distances ('offset'). a) - c) show signals observed between 1 and 10 km epicentral distance with 1 km spacing while d) - f) show signals between 0.2 and 2 km epicentral distance with a spacing of 0.2 km. a) & d) show seismic acceleration, b) & e) SE traces including IRs and coseismic signals while c) & f) only show IR amplitudes excited at subsurface interfaces. The onset times of the direct P- and S-waves are marked as well as the onset times of the rIRs and eIRs generated by the direct P- and S-waves at the uppermost interface in 500 m depth. The traces are coloured according to epicentral distance (compare Fig. 4.5).*

To quantify the amplitude behaviour of the first arrivals with epicentral distance, we determined the maximum amplitudes of the IRs created by the direct P-phase at the first interface as well as the maximum of the first coseismic arrival over increasing epicentral distance (Fig. 4.4). While in Fig. 4.4a the amplitudes are normalised to the overall maximum value of the coseismic signals, the amplitudes in Fig. 4.4b are normalised to the individual coseismic values.

Analysing the maximum values in Fig. 4.4a shows that the coseismic amplitudes increase with increasing distance up to approximately 5 km. After that, the amplitudes decay slowly to about 60% of their maximum value at 10 km distance. The IRs reach their maximum amplitudes at approximately 1 km epicentral distance. Up to this length the amplitudes of the coseismic signals and IRs are in the same order of magnitude. This agrees with the findings of Ren et al. (2018) that at low frequencies (in our case 15 Hz, see section 4.4) eIRs are able to exceed coseismic amplitudes. After 1 km the amplitudes of the IRs start to decay rapidly, so that at 2 km distance their amplitudes equal less than 10% of the coseismic amplitudes' size (Fig. 4.4b). While the eIRs' amplitudes seem to stabilise after 4 km at around 2% of the coseismic amplitudes' size, the rIRs amplitudes fall to less than 0.1% at increasing distances. They become so small that for epicentral distances larger than 4 km they are not recognisable among the other SE signals anymore. This explains the large dispersion of rIR amplitudes visible in Fig. 4.4.

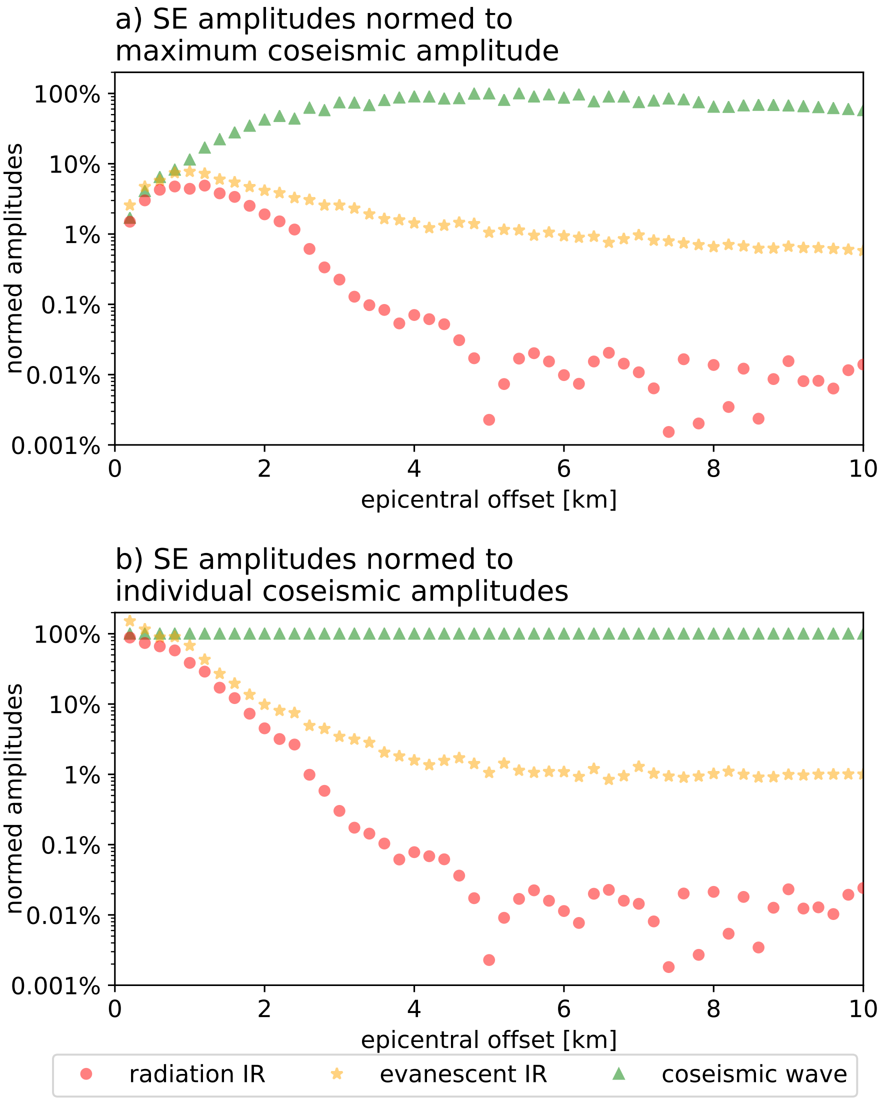

Fig. 4.4: *Maximum amplitudes of the observed rIR and eIR excited at the uppermost interface in 500 m depth as well as the coseismic signal belonging to the direct P-wave. The signals were calculated for up to 10 km epicentral distance with a spacing of 0.2 km. a) amplitudes are normalised to the global maximum coseismic amplitude over all distances; b) amplitudes are normalised to the individual maximum coseismic amplitudes of each epicentral distance.*

4.5.2 IRs in the frequency domain (SESRs)

To analyse the effect of IRs in the frequency domain, we calculated the SESRs corresponding to the traces depicted in Fig. 4.3. Fig. 4.5a shows the SESRs calculated for receivers with increasing epicentral distances between 1 and 10 km. Close to the epicenter the SESRs reveal a decreasing trend towards higher frequencies, while SESRs further away show singular peaks but an overall decreasing trend is no longer visible. A first guess is that the decreasing trend is caused by IRs, which affect SESRs at small epicentral distances stronger, similar to what can be observed in the time domain. However, if we calculate the SESRs for the same epicentral distances using only the coseismic field, the same trend is visible even though IRs are not present (Fig. 4.5b). We therefore suspect that the decreasing trend is a result of the insufficient proportionality between the seismic and the coseismic field – due to the existence of shear-movement – rather than the influence of the IRs.

Nonetheless, the influence of the IRs on the SESRs is still visible in that the SESRs calculated from the full SE field (Fig. 4.5a) show more distinct peaks than the SESRs calculated from the coseismic field only (Fig. 4.5b). The question is, in which depth the IRs that lead to these peaks are excited. Fig. 4.5c shows SESRs calculated from a SE field, where the generation of IRs was only allowed at the surface and not at the interfaces. If we compare these results with the SESRs from the full SE field (Figs 4.5a,c), we can see small deviations for close epicentral differences (1 and 2 km) but not further away. We therefore conclude that SESRs recorded at larger distances are mostly influenced by IRs excited at the free surface whereas SESRs at close distances can be influenced by IRs excited at subsurface interfaces as well.

To further investigate this behaviour we computed SESRs for the same fields as in Figs 4.5a to c, this time for offsets up to 2 km (Fig. 4.5d-f). Similar to before, the decreasing trend of the SESRs becomes smaller with increasing distances. Again, as this behaviour can also be observed for SESRs calculated by the coseismic field only (Fig. 4.5e), it is most likely not caused by the IRs themselves but rather the influence of signals related to shear movement.

If we compare the near-offset-SESRs calculated from the whole SE field (Fig. 4.5d) to those calculated from the field where IRs are only excited at the surface (Fig. 4.5f), clear differences can be seen. As these differences are most distinct for low frequencies, we suggest that they results from eIRs, which have frequency dependent amplitudes (cf. Ren et al. (2018)).

Summing up the main results of this section, we can conclude that in the time as well as the frequency domain the effect of IRs excited in the subsurface is best investigated close to the epicenter. At larger distances coseismic signals dominate the SE observations. In case the influence of IRs is noticeable, it is more likely caused by eIRs than rIRs.

4.6 SE response to changes in hydrological parameters

In the previous section we showed how IRs influence SE waveforms as well as SESRs depending on the station's distance to the epicenter. Now we analyse how parameter variations in the subsurface influence the recordings. As described in the introduction, tectonically induced changes in ground water level, transport and chemistry occur in the

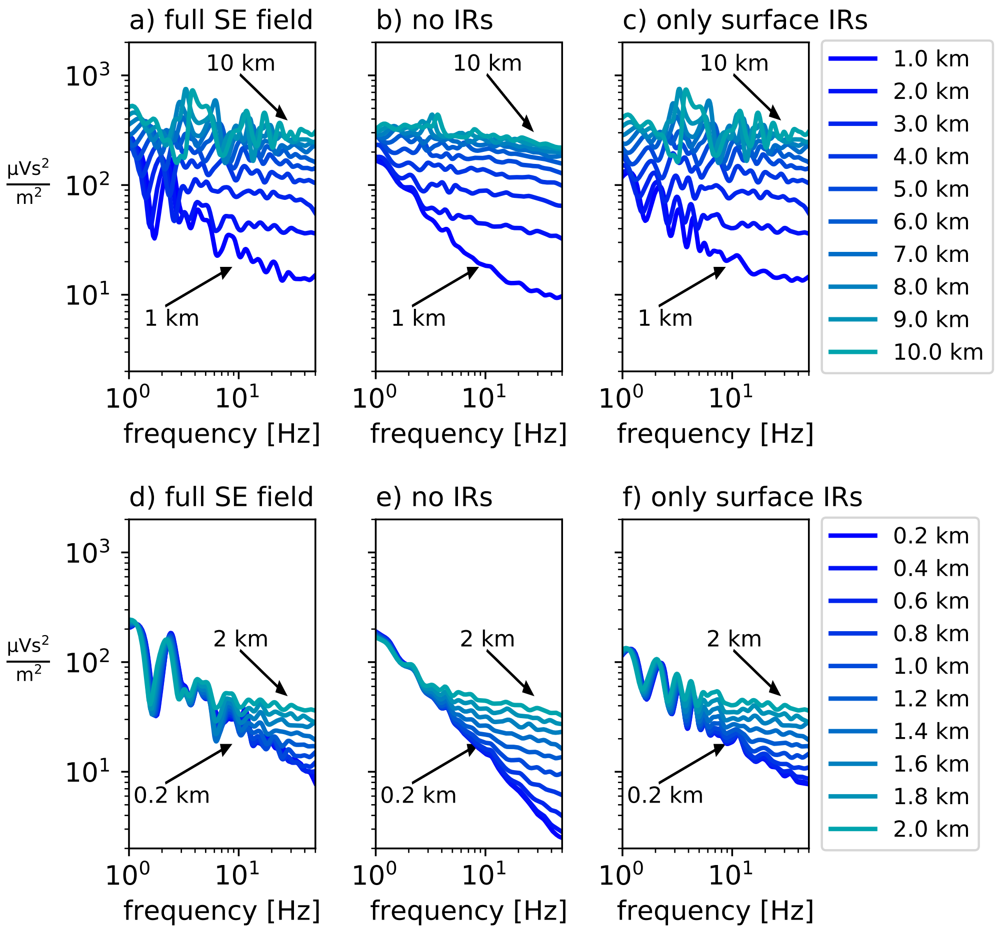

Fig. 4.5: *SESRs calculated for increasing epicentral distances. a) - c) show SESRs calculated from signals between 1 and 10 km epicentral distance with 1 km spacing while d) - f) show SESRs calculated from signals generated between 0.2 and 2 km distance with a spacing of 0.2 km. a) & d) show SESRs calculated from the full SE field, including IRs and coseismic signals, b) & e) show SESRs calculated from the coseismic field only (no IRs) while c) & f) show SESRs calculated from signals that only include IRs excited at the free surface.*

uppermost geological layers, which is where SE has its highest sensitivity (Dzieran et al., 2019). To concretise this for the Armutlu location, we vary the relevant parameters of near surface layers in different ways.

First, we alter the base-model described in section 4.4 by dividing the uppermost layer into two parts with equal parameters (see Tab. 4.1, layer 1). Then we compose three different scenarios corresponding to different reactions of the subsurface to tectonic stress changes. In the first scenario we change the porosity of the new second layer from 5% to 10%. In the second scenario we alter the permeability by two decades from 0.1 Darcy to 0.001 Darcy while the porosity is set back to 5%. In the third scenario the only parameter that deviates in the additional layer is the salinity, which we rise from 0.005 mol/l to 0.5

scenario	parameter change	layer top	layer thickness	layer bottom
I	porosity from 5% to 10%	20 m	10 m	30 m
II	porosity from 5% to 10%	20 m	100 m	120 m
III	porosity from 5% to 10%	200 m	10 m	210 m
IV	porosity from 5% to 10%	200 m	100 m	300 m
V	permeability from 0.1 to 0.001 Darcy	20 m	10 m	30 m
VI	permeability from 0.1 to 0.001 Darcy	20 m	100 m	120 m
VII	permeability from 0.1 to 0.001 Darcy	200 m	10 m	210 m
VIII	permeability from 0.1 to 0.001 Darcy	200 m	100 m	300 m
IX	salinity from 0.005 to 0.5 mol/l	20 m	10 m	30 m
X	salinity from 0.005 to 0.5 mol/l	20 m	100 m	120 m
XII	salinity from 0.005 to 0.5 mol/l	200 m	10 m	210 m
XII	salinity from 0.005 to 0.5 mol/l	200 m	100 m	300 m

Tab. 4.2: *Scenarios of parameter variations analysed in section 4.6: The first layer of the base model (see Tab. 4.1) is split into two parts after which the lower part is altered according to the described scenarios.*

mol/l. The first two scenarios are intended to simulate an opening of microcracks in a sub-volume of the subsurface as a reaction to changes in tectonic stresses. The third scenario intends to simulate the effect of an intrusion of salt water into fresh ground water, corresponding to mass movement caused by volumetric strains or pressure changes such as reported by Woith et al. (2013) for the Adana region (Turkey).

We calculate the response to the scenarios in four different ways. In the first two cases the altered layer begins in 20 m depth with thicknesses of 10 and 100 m, respectively. In the third and fourth case we apply the same layer thicknesses, but place the top of the layer in a depth of 200 m. Overall, this leads to 12 different scenarios for us to compare. Please note that in all scenarios the uppermost layer remains unaltered. Therefore, the coseismic field should not change unless the seismic waves change as well. For an overview, the details of each scenario are listed in Tab. 4.2.

4.6.1 SE response near the epicentre

First we analyse how the above described scenarios affect SE waveforms in the time domain. As an example we choose the traces in 1 km epicentral distance, as here the IR amplitudes are largest (see section 4.5, Fig. 4.4). Since we are mainly interested in amplitude strengths, we plot and analyse the envelopes of the traces. These show two main peaks corresponding to the direct P- and S-arrivals. To be able to compare the responses of the different models, the envelopes were normalised to the maximum of the base-model's envelope.

The comparison of the response to the different scenarios in Fig. 4.6 shows that the changes induced by the model variations are much stronger in the SE envelopes than in the seismic envelopes, where differences are barely visible. We therefore conclude that the observed changes are caused by varying IRs in the SE signal rather than variations of the coseismic field. The overall SE envelope is affected most by the porosity variation, for which a rise of amplitudes between factor 2 and 4 can be observed for the S-phase (scenarios I-IV). The permeability variation on the other hand, does not influence the amplitudes visibly, which could be explained by the chosen parameter range (scenarios V-VIII). The salinity variation affects mostly the P-phase of the SE field with amplitude amplifications between factor 2 and 3 (scenarios IX-XII). These findings agree in general with the sensitivity analyses from Garambois and Dietrich (2002) and Monachesi et al. (2018).

For all scenarios, the amplitude effects of the parameter variations are greater for the 100 m thick layer than for the 10 m thick layer. While for the porosity variation a larger response is evoked if the top of the layer is in 20 m instead of 200 m depth (factor 1.6 to 2, scenarios I & II vs. III & IV), the response to the salinity variation is roughly in the same order of magnitude for layers in 200 m and 20 m depth (scenarios IX & X vs. XI & XII).

Fig. 4.7 shows the SESRs resulting from the different scenarios together with the SESR of the base-model at 1 km epicentral distance. Similar to the envelope response, large differences can be seen for changes in porosity (scenarios I-IV) and salinity (scenarios IX-XII) whereas the SESRs are not significantly affected by the permeability variation (scenarios V-VIII).

The response of the SESRs to the porosity variation cannot be described as ‘uniform’. If the top of the layer is placed in 20 m depth, the 10 m thick layer leads to an increase of amplitudes of more than factor 5 at frequencies above 25 Hz (scenario I), whereas the 100 m thick layer alters the SESR over all frequencies (scenario II). In the case of the 200 m deep layer, 10 m thickness leads only to small variations (scenario III, maximum increase of factor 1.5) whereas 100 m of thickness influences the SESR mainly at frequencies between 2 and 12 Hz (scenario IV, maximum increase of factor 4). Additionally the positions of peaks and troughs of the SESRs seem to change rather randomly between all four scenarios characterised by a porosity change.

Contrary to this behaviour, we see comparable SESR responses towards salinity variations (scenarios IX-XII). For the 20 m as well as the 200 m deep layer, 10 m thickness leads to a slightly smaller impact than 100 m thickness. Additionally the position of peaks and troughs does not change significantly depending on the layer thicknesses. Last but not least, in all four cases can the largest effect be found for frequencies above 10 Hz (increases between factors 2 and 5).

We explain the impression that the SESRs are affected more randomly by the porosity than the salinity alteration by that a change of the salinity only affects electric properties, whereas a porosity variation impacts both electric and seismic properties, leading to more complicated response patterns.

4.6.2 SE responses at increasing epicentral distances

Our analysis showed that the variation of hydrogeophysical subsurface parameters is capable to induce first-order changes in SE envelopes as well as SESRs near the epicentre.

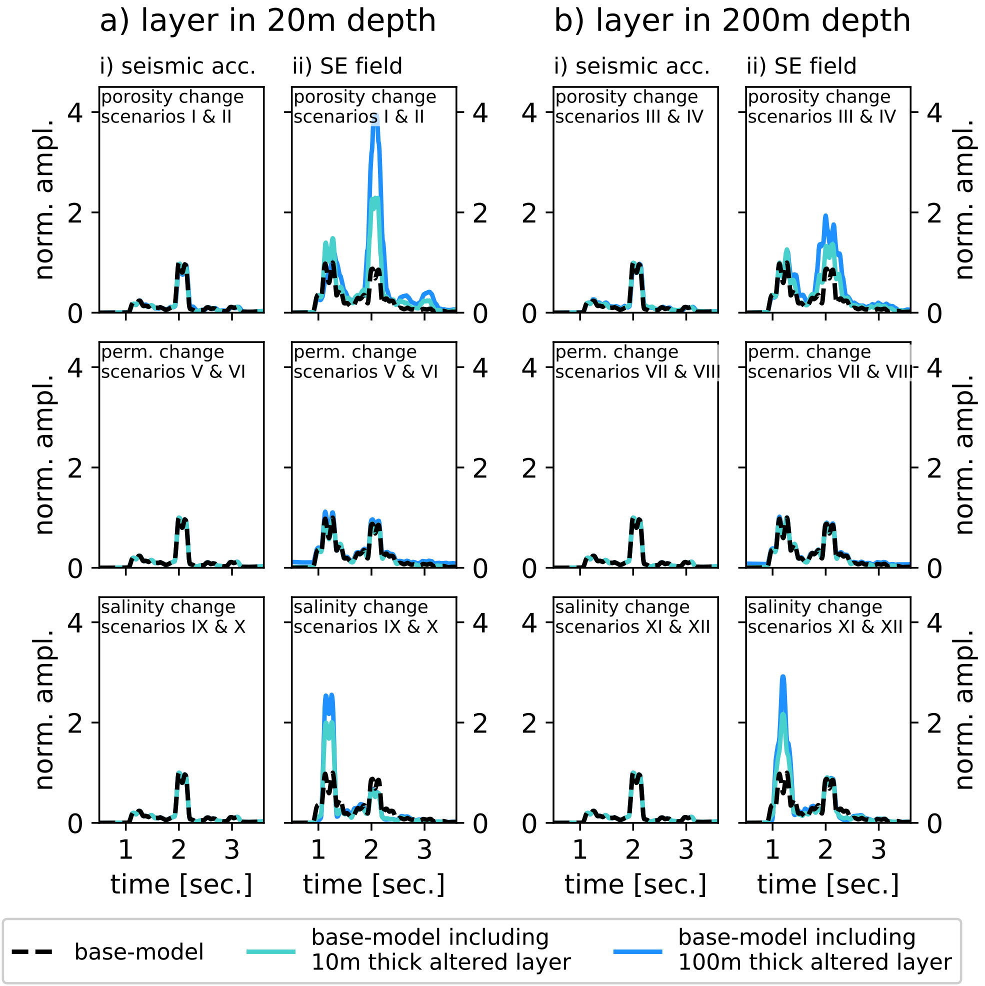

Fig. 4.6: *Envelopes of seismic and SE traces corresponding to scenarios described in Tab. 4.2 calculated for 1 km epicentral distance. The envelopes were smoothed over 10 samples and normalised to the maximum of the base-model's envelope.*

We now investigate how these responses change for increasing epicentral distances up to 10 km.

We start again by analysing SE amplitudes in the time domain. For the base-model as well as each scenario 51 envelopes were computed equally spaced over 10 km epicentral distance. We then calculated the difference between the scenario envelopes and the corresponding base-model envelopes and determined the maximum differences for each epicentral distance differentiating between the P- and S-phase peaks (Fig. 4.8).

The distance analysis shows similar effects for all scenarios. The largest differences between the scenario and base-model envelopes is found in 1 km distance (differences up to value 4, permeability 10 times less) after which the value strongly decreases until approximately 3 km distance. At further distances the differences become insignificantly small (less than 0.1). This agrees with our observation that IRs can best be identified if the stations are located close to the epicenter of the earthquakes. Exceptions from this be-

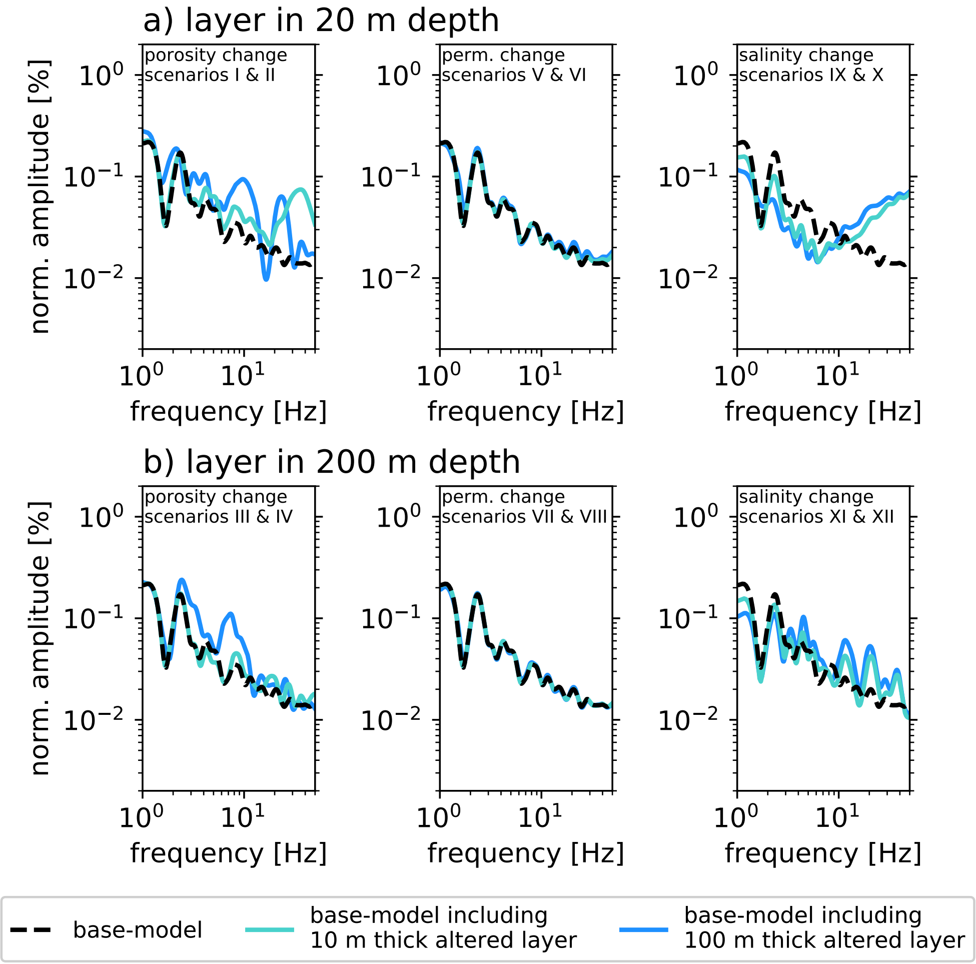

Fig. 4.7: *SESRs corresponding to scenarios described in Tab. 4.2 calculated for 1 km epicentral distance.*

haviour can be seen in the S-phase of scenarios II, IX and X. In the S-Phase of scenario II (porosity change for 100 m thick layer in 20 m depth) a second smaller maximum can be found at a distance of about 4 km (0.8 as opposed to 3.3), after which the value decreases to a constant difference of about 0.5. For the S-phases of scenarios IX and X (salinity change for 10 m and 100 m thick layer in 20 m depth) no decreasing trend can be seen, but the difference remains rather constant at 0.2 over the whole distance range.

Overall, the distance analysis confirms the conclusions drawn from the computations for 1 km epicentral distance (see section 4.6.1). If the porosity is altered, the S-phase of the envelopes is about 4 times more affected than the P-phase and the layer in 20 m depth results in a higher response than the layer in 200 m depth (about factor 2 for the S-Phase). Contrary to that, the salinity alteration leads to a greater response in the P-phase (about 1.8 times greater than in the S-phase), and the layer in 200 m depth results in an about 1.5 times higher response than in 20 m depth. Lastly, the response to the permeability variation is more than 10 times smaller compared to the variation of the porosity or salinity, although the same general response distribution can be seen in the data.

For the SESRs we did not calculate differences but formed the ratios between the base-model's and scenarios' SESRs. We then determined the mean value of these ratios and plotted it in percentage over increasing epicentral distances (Fig. 4.9).
We can generally identify similar effects as for the envelopes, although a few differences are noticeable. In the case of the SESRs, the 20 m deep layer leads to a larger response than the 200 m deep layer for all parameter variations (difference of up to factor 10). The thinner layer thereby always excites a lower response, except for scenarios I and II (porosity change for 10 m and 100 m thick layers in 20 m depth), where the response of the 10 m thick layer is about twice as high as that of the 100 m thick layer for epicentral distances below 2 km. For distances further than 4 km, the ratio gets very small (below 5%), except for the porosity and salinity variations in 20 m depth (scenarios I,II,IX and X). Here a constant value of about 30% is reached. This suggests that subsurface parameter changes of shallow layers can be observable in SESRs also at somewhat larger distances from the epicenter even though the uppermost layer remains unchanged. This is confirmed by the field data and inversion results of Dzieran et al. (2019).

Summarising the sensitivity analysis of SE signals towards parameter variations, we conclude that porosity and salinity changes are visible in envelope as well as SESR analysis. Whether the effect is observable in field data, depends highly on the local noise level. This will be discussed in section 4.7. Furthermore, envelope analysis may be a tool to distinguish between changes in salinity and porosity due to the different effects on the P- and S-Phase of the signals. The response of the signals to permeability changes is rather small, at least if the variation is limited to two decades, as it is in this case. The chance to observe signal variations is best if the station is positioned close to the epicenter of the earthquake, although SESR analysis can detect changes in porosity and salinity at further distances, too, as was shown by Dzieran et al. (2019).

4.7 Are SE signals detectable under realistic noise conditions?

4.7.1 SE amplitudes for an exemplary microseismic event

In sections 4.5 and 4.6 we came to the conclusion that IRs form a considerable fraction of SE signals generated by earthquakes and that they respond visibly to subsurface changes. As these conclusions are based on synthetic data with normalised amplitudes, the foremost question is, whether these signals would actually be identifiable in a field experiment exposed to anthropogenic and natural noise.
To investigate what amplitude sizes we can expect for the SE signals, we used the seismic waveforms of a randomly chosen earthquake that was recorded on the ARMT station of the KO network, operated by the Kandilli Observatory and Earthquake Research Institute (KOERI), Bosphorus University (Bogazici University Kandilli Observatory And Earthquake Research Institute, 2001). According to the ISC catalog, the selected event that

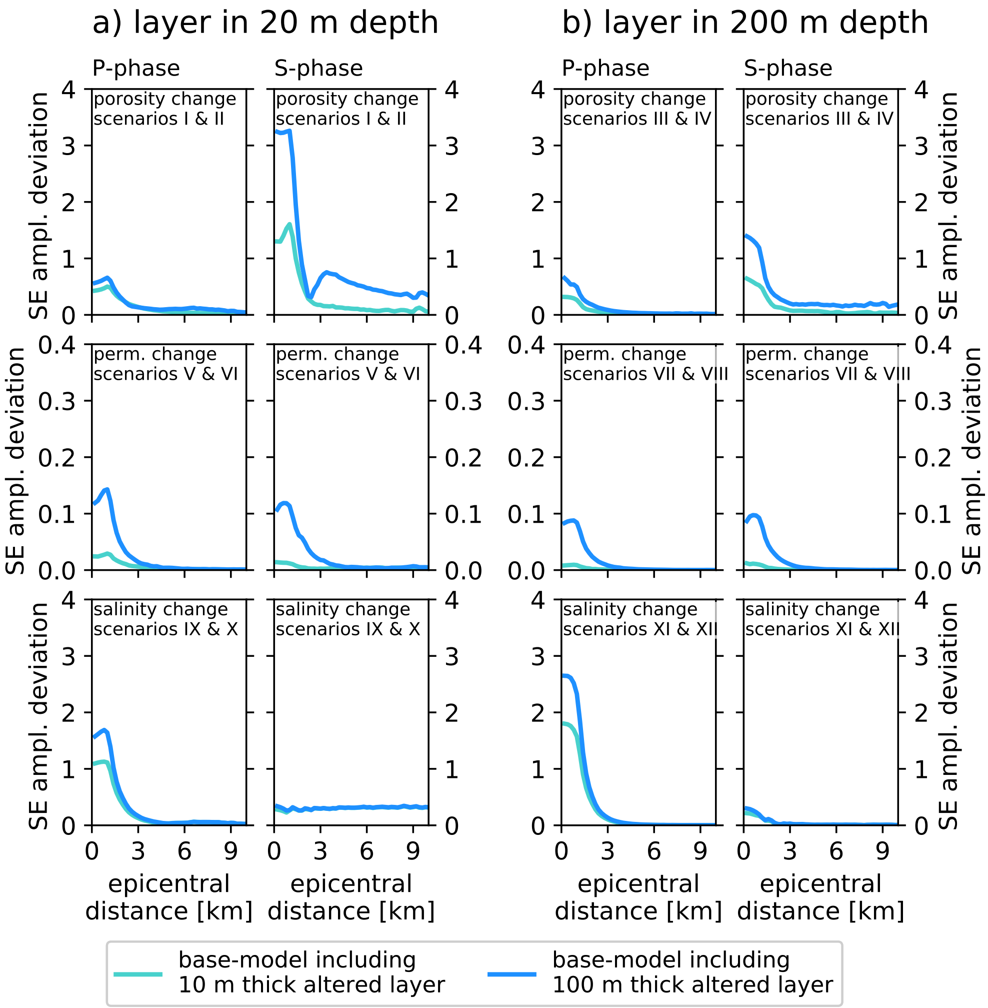

Fig. 4.8: *Maximum difference between the normalised envelopes resulting from the scenarios described in Tab. 4.2 and the base-model envelope over increasing epicentral distances. The maximum values were determined for the P-and S-Phase individually.*

happened on October 11th, 2016 at 23:44:18.90 UTC had a local magnitude of 2.0 (International Seismological Centre, 2015). The source was located at 40.6173° North and 28.9517° East in a depth of 6 km, 9 km North-East of the recording station. The location of the earthquake as well as the recording station are shown in Fig. 4.1.

The seismic waves were recorded with a sampling rate of 100 Hz. To obtain the radial component, the recording coordinate system was rotated in the backazimuth of 53.1°.

Fig 4.10a shows the observed seismic acceleration. The corresponding synthetic traces shown in Fig. 4.10b were calculated with the according parameters and the base-model described in section 4.4. The maximum calculated amplitude was then scaled to the maximum observed amplitude of about $2\,\mathrm{mm/s^2}$ (Fig. 4.10a). With this value for the maximum seismic acceleration, the corresponding SE amplitudes would reach about $0.6\,\mu\mathrm{V/m}$ (Fig. 4.10b). The coseismic signals in the 'P-phase' are about ten time smaller ($0.05\,\mu\mathrm{V/m}$) and an IR amplitude cannot be identified. Fig. 4.10c shows the corresponding seismic and

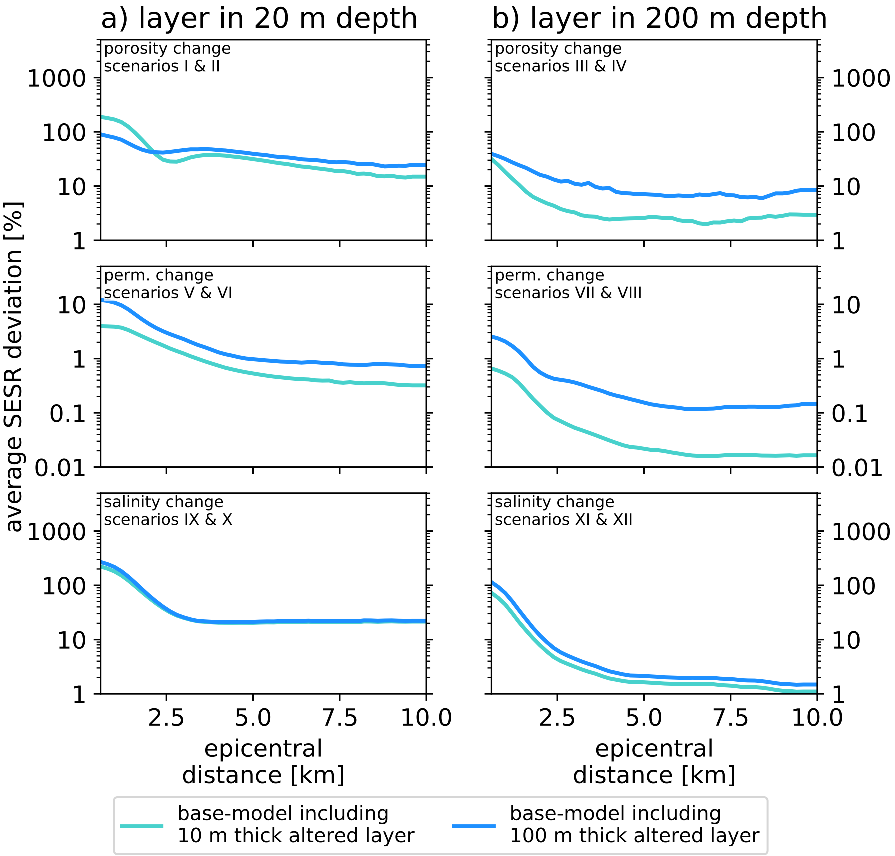

Fig. 4.9: *Mean values of ratio between SESRs resulting from the scenarios described in Tab. 4.2 and the base-model's SESR over increasing epicentral distances.*

SE traces for 1 km epicentral distance. Contrary to the SE signals in 9 km distance a clear IR signal can now be identified before the P-onset. However, with 0.0065 μV/m, this SE amplitude is very small. Still, the result can be used for establishing a relation between the local earthquake magnitude and expected SE amplitudes as we demonstrate in the next section.

The amplitude sizes of the IR as well as the first seismic and coseismic onsets can be found in Tab. 4.3. When comparing the amplitudes in 1 and 9 km distance it stands out that the amplitudes of the seismic acceleration rise by factor 1.2 whereas the corresponding coseismic amplitudes rise by a factor of 5. This shows that a direct proportionality between the seismic and coseismic field is not given. This indicates that what we identify as 'coseismic' is not purely coseismic, but a mixture of coseismic and IR amplitudes that are excited at the free surface. This agrees with the observation described in section 4.5.2 that at larger epicentral distances the influence of the 'free surface IRs' can be detected in the shape of the SESRs. As we are not able to distinguish between the pure coseismic amplitudes and the amplitudes of the IRs excited at the free surface, we continue to call the onsets 'coseismic'.

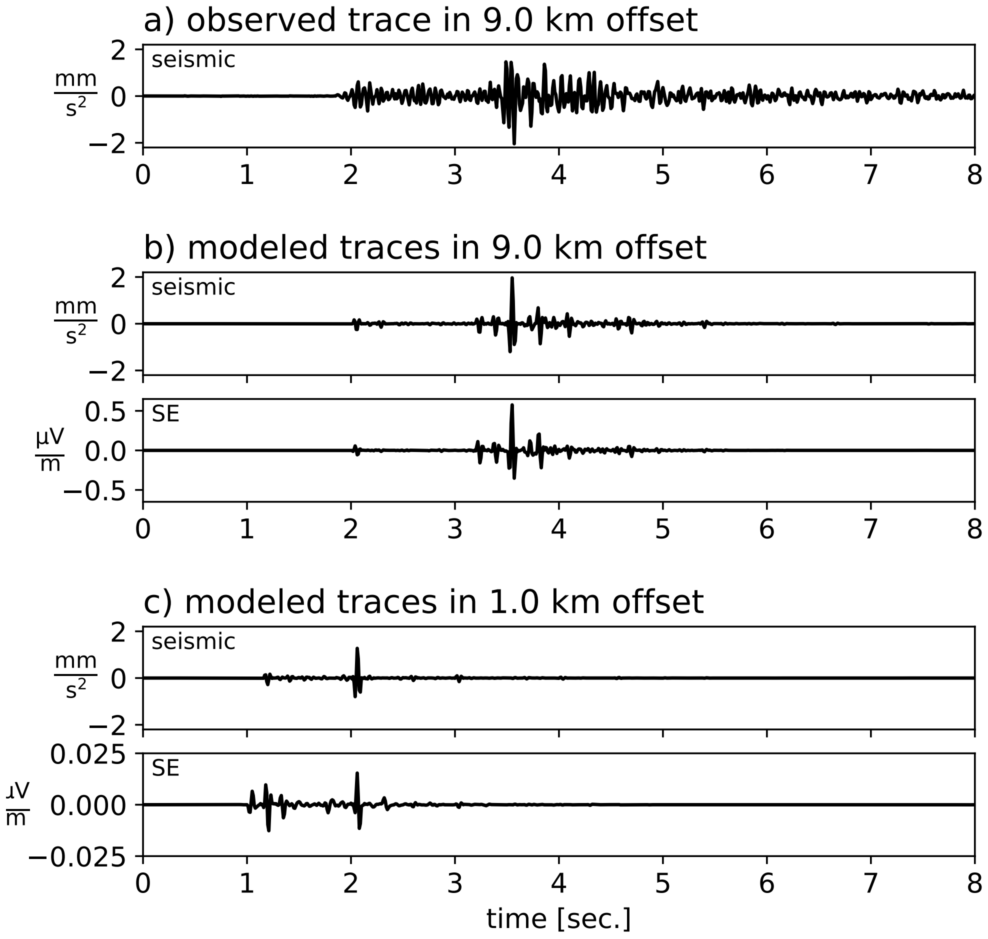

Fig. 4.10: *a) Seismic amplitudes of a magnitude 2 earthquake recorded in 9 km epicentral distance on the Armutlu Peninsula. The location of the earthquake and the recording station are shown in Fig. 4.1; b) synthetic seismic and SE amplitudes computed with the base-model for an epicentral distance of 9 km. The amplitudes were scaled to the observed seismic amplitudes shown in a); c) synthetic seismic and SE amplitudes computed with the base-model for 1 km epicentral distance, applying the same source strength as used for amplitudes in b).*

4.7.2 Generalisation of results

To investigate which seismic event can be expected to generate SE arrivals that are identifiable in field records two steps need to be performed: 1) the numerical results of section 7.1 have to be generalised with respect to event magnitude, event depth and hypocentral distance, and 2) the resulting SE signal strengths have to be compared with typical levels of electromagnetic background noise. The result of the waveform computation in section 7.1 can be reduced to the statement that an event of local magnitude M_0 at a depth of z_0 will create a seismic ground acceleration $\ddot{u}_0$, an IR field strength i_0 and coseismic SE field strength c_0 at a hypocentral distance r_0. For the generalisation we use the definition equation of the local magnitude M as a function of seismic amplitude $\ddot{u}$ and hypocentral distance r (e.g., Bormann et al., 2013):

$$M = log(\ddot{u}) + 1.11 \cdot log(r) + 0.00189 \cdot r - 2.09 \tag{4.3}$$

where log is the decadic logarithm. For a given amplitude $\ddot{u}_0$ caused by an earthquake with the magnitude M_0 in a hypocentral distance r_0 one can calculate the seismic amplitude $\ddot{u}$ for any given magnitude M and hypocentral distance r by forming the ratio of $M(\ddot{u}, r)$ and $M_0(\ddot{u}_0, r_0)$, leading to:

$$\ddot{u}(M,r) = \ddot{u}_0 \cdot 10^{(M - M_0 - 1.1(log(r/r_0)) - 0.00189(r - r_0))} \tag{4.4}$$

The relation between strengths of the SE and seismic amplitudes is linear with respect to the initial source amplitude. Therefore, the SE field strength for variable M and r can be estimated from the modelling result by applying

$$i(M,r) = i_0 \cdot \ddot{u}(M,r)/\ddot{u}_0 \tag{4.5}$$

and

$$c(M,r) = c_0 \cdot \ddot{u}(M,r)/\ddot{u}_0 \tag{4.6}$$

When applying these equations one has to be aware that their results are just an estimate based on the assumptions that the influence of changes of radiation and incidence angles can be neglected while r is being varied. Still they will provide a correct order of magnitude, if the variations in z and r are not over-stressed.

Based on these considerations we estimated the SE amplitude to be expected for earthquakes with magnitudes between 0.1 and 5 for recording stations located 1 and 9 km away from the epicenter (Fig. 4.11). The chosen values for the variables can be found in Tab. 4.3. They are based on the amplitude values of the first 'coseismic' and IR arrivals depicted in Fig. 4.10.

For 9 km epicentral distance (Fig. 4.11a) we only calculated the expected amplitude of the coseismic P-Phase, as an IR could not be identified in the synthetic wavetrain shown in Fig. 4.10b. For 1 km epicentral distance (Fig. 4.11b) we calculated the expected coseismic as well as IR amplitudes. In this case, the ratio between the IRs and coseismic amplitudes is approximately 1.5 (see values for i_0 and c_0 in Tab. 4.3). The amplitudes were estimated for hypocenters in 1, 6 and 10 km depth.

For determining detectability thresholds the estimated SE field strengths have to be compared to realistic levels of ambient electromagnetic noise. For this purpose we used field data recorded by magnetotelluric stations in sparsely populated areas of Chile, Costa Rica and Norway (Dzieran et al., 2020). Depending on the station location the noise levels varied between 0.1 and 2.6 μV/m. Therefore, we defined 0.1 μV/m as the low-noise-threshold, and 10 μV/m as the high-noise-threshold.

The graphs in Fig. 4.11a show that a M2.5 earthquake would be able to generate a coseismic P-phase signal at 9 km epicentral distance that exceeds the low-noise-threshold of 0.1 μV/m (expected amplitudes: 0.2-0.1 μV/m for 1-10 km hypocentral depth). For

parameter	1 km	9 km epicentral distance
depth z_0	6 km	6 km
hypocentral distance r_0	6.1 km	10.8 km
magnitude M_0	2	2
amplitudes of seismic P-phase $\ddot{u}_0$	$0.14\,\mathrm{mm/s^2}$	$0.17\,\mathrm{mm/s^2}$
amplitudes of IRs i_0	$0.0065\,\mu\mathrm{V/m}$	-
amplitudes of 'coseismic P-phase' c_0	$0.01\,\mu\mathrm{V/m}$	$0.05\,\mu\mathrm{V/m}$

Tab. 4.3: *Parameters for estimating SE amplitudes for given magnitudes and hypocentral distances in section 4.7.2.*

the signals to exceed the high-noise-threshold of $10\,\mu\mathrm{V/m}$, the events would have to be larger than M4.5 (exp. amp.: 20-13 $\mu\mathrm{V/m}$ for 1-10 km depth). At 1 km epicentral distance a M2.5 earthquake would excite an IR amplitude as large as the low-noise-threshold (0.1 $\mu\mathrm{V/m}$), but only if the hypocenter is located in 1 km depth (Fig. 4.11b). At the Armutlu Peninsula, however, the majority of hypocenters lie around 6 km depth (Fig. 4.2). In this case IRs from a M2.5 earthquake in 1 km distance could probably only be observed in a low-noise environment (exp. amp.: 0.02 $\mu\mathrm{V/m}$). For the IRs to exceed the low-noise-threshold, the magnitude would have to rise to 3.2. For the amplitudes to become larger than the high-noise-threshold ($> 10\,\mu\mathrm{V/m}$), the events would have to exceed M4.5 for hypocentral depth of 1 km and M5 for hypocenters deeper than 6 km.

4.8 Discussion

The goal of this study is to numerically investigate SE signals generated by local earthquakes and their ability to provide information about hydrogeophysical changes in the local subsurface. As a possible scenario we chose a potential field study on the Armutlu Peninsula in Turkey, focusing on presumed changes of porosity, permeability and ground water salinity and the corresponding changes of the SE response as a function of epicentral distance. Based on the results from sections 4.5 to 4.7 we now discuss the objectives raised in the introduction with regards to a possible field experiment.

4.8.1 Which traveltimes and amplitude strengths can be expected for different sorts of SE arrivals in the time and frequency domain for frequently occurring local seismic events?

Coseismic SE signals appear simultaneously with the onset of the seismic P-wave. They generally have larger amplitudes than the IRs, which is most obvious in the time domain. In 9 km epicentral distance a M2.5 earthquake can generate a coseismic P-phase signal with amplitudes around 0.15 $\mu\mathrm{V/m}$, which would be observable under low to moderate noise conditions (Fig. 4.11a).

eIRs appear shortly before the onset of the coseismic signals. For epicentral distances larger than 4 km their amplitudes will reach 1% of the coseismic signals' amplitudes

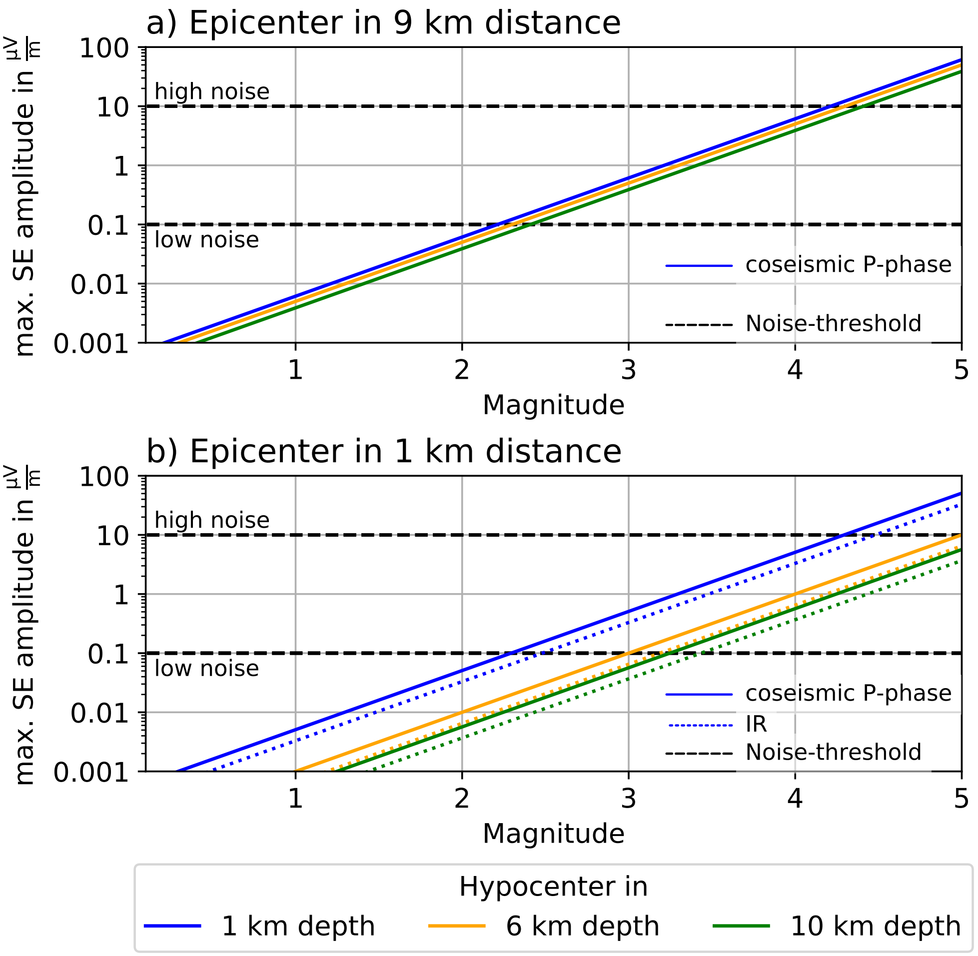

Fig. 4.11: *Expected SE amplitudes for earthquakes in a) 9 km and b) 1 km epicentral distance depending on hypocentral depth based on the amplitudes derived in Fig. 4.10b and c. In an epicentral distance of 1 km the IR amplitude is estimated to be about 1.5 times smaller that the coseismic amplitude.*

(Fig. 4.4a). They are more likely to be detected when the recording station is positioned close to the epicenter of the earthquake. In that case, earthquakes with an average depth of 6 km would have to exceed at least magnitude 3.2 to create signals with amplitudes in the order of 0.1 μV/m, which corresponds to the low-noise-threshold (Fig. 4.11b).
rIRs could theoretically be recognised through their simultaneous onset on spatially distributed stations (arrays). However, their amplitudes decay even faster than eIR's. Therefore, especially for microseismic events, they can only be recognised close to the epicenter in which case their amplitudes overlap with amplitudes from eIRs (Fig. 4.3).

In the frequency domain we analysed SESRs. They are characterised by a decreasing trend over increasing frequencies, although the amount of this decrease lessens with increasing epicentral distance. Our analysis implies that this behaviour is most likely not based on the influence of IRs but rather on the varying proportionality between the coseismic and seismic field due to shear movement. However, the influence of the IRs is still visible in the distinct peaks of the SESRs. As this behaviour is most prominent at low frequencies, we expect eIRs to be the main cause.

From the comparison of the SESRs in Fig. 4.5 we conclude that the influence of subsurface IRs can best be observed near the epicenter whereas the frequency variations at larger distances are caused by IRs excited at the free surface (section 4.5.2). Nonetheless, Dzieran et al. (2019) were able to identify the influence of subsurface IRs in a SESR recorded in Chile at an epicentral distance of over 230 km. Apart from differing subsurface parameters, this can be explained by that in the synthetic model of the Chilean SESR the interfaces were set at 100 and 300 m depth, whereas in the base-model of the Armutlu Peninsula the first interface can be found at 500 m. We therefore suspect that IRs from shallow layers can also influence SESRs at larger epicentral distances. This is confirmed by the scenario-analysis in section 4.6.2 that suggests that variations of porosity and salinity in 20 m depth can be detected by SESRs at increasing epicentral distances, too.

Regarding a possible field experiment, we believe that in the time domain eIRs will most likely be identified if the recording station is located close to the epicenter, whereas coseismic signals can be observed over greater distances, too. In the frequency domain the influence of the eIRs is also largest near the epicenter but IRs from shallow layers can influence SESRs also at larger distances. When analysing SESRs one has to be careful to distinguish between effects caused by IRs and by possible shear movement as both can influence the shape of the SESR.

4.8.2 Which parts of the SE signals carry information on which structural and hydrological parameters?

To test the capability of SE signals to reveal information about subsurface variations, we analysed envelopes as well as SESRs (section 4.6). We now discuss similarities and differences between the two methods.

The comparison shows that the responses of the envelopes and SESRs towards varying subsurface parameters are rather similar in most aspects. In both cases, the largest response difference between the base-model and the modified scenarios can be found in the epicentral distance of 1 km. This difference decays quickly until it is barely noticeable in 4 km distance. Only a porosity and a salinity variation in 20 m depth can still be identified at a larger radius. Furthermore, the 100 m thick layer leads to a more prominent response than the 10 m thick layer for almost all scenarios. This behaviour can probably be attributed to interfering effects (for more information on how thin bedding can influence SE amplitudes confer Grobbe and Slob (2016)). Last but not least, neither envelopes nor SESRs seem to be able to identify changes in permeability sufficiently.

A difference between envelope and SESR analysis can be found in their distinct responses towards porosity and salinity variations. Through envelope analysis one might be able

to differentiate between effects caused by the two parameters as the P- and S-Phase respond differently to their variation. For SESRs, this separation appears more complicated, because even though the response to a salinity variation seems more uniform than to a porosity variation, such kind of comparison is hard to quantify. To identify what causes differences in SESRs iterative inversion computations could be considered (cf. Dzieran et al. (2019)).
In summary, we conclude that envelope as well as SESR analysis are able to identify subsurface changes regarding porosity and salinity. So far, we cannot declare one method to be better suited in detecting subsurface variations than the other. We therefore recommend applying both methods on real field data and compare the results.

4.8.3 At which epicentral distances would monitoring stations need to be placed to obtain optimum results?

The calculations show that for our model the best epicentral distance to place a monitoring station would be close to the epicenter. From Fig. 4.3 we can conclude that about 1 km is the distance at which coseismic and IR amplitudes are largest while still being in the same order of magnitude. Fig. 4.11 shows that for this epicentral distance the magnitude of the earthquakes would have to be rather high for the signals to be visible above the noise-level ($>$ M3.2). One will therefore probably have to compromise between a satisfying ratio of coseismic to IR amplitudes and the overall signal/noise ratio.

A main difficulty in designing a field experiment will be to position the recording stations as closely to the earthquakes' epicentres as possible. One way to overcome this problem would be installing a wide spread array with a large number of recording stations covering the relevant area. A second option would be to prepare a kind of 'task-force' that can quickly install mobile recording stations after the location of an earthquake cluster has been identified.
Additionally to the geometrical aspects other influences such as the local noise level have to be considered when choosing an appropriate station location. Therefore, as much previous knowledge as possible about station locations should be gathered to optimise the outcome of a SE field experiment.

4.8.4 Which event magnitudes would be required in order to record SE events of a signal/noise-ratio allowing a reliable monitoring, and how frequently do events exceed this threshold?

Fig. 4.11a shows that at 9 km epicentral distance, a 1 to 10 km deep M2.5 earthquake should be able to excite coseismic signals that exceed the low-noise-threshold of $0.1\,\mu\mathrm{V/m}$. Yet, in order to record IRs with similar amplitude sizes as their coseismic counterparts, smaller epicentral distances are necessary, for example 1 km. Considering the expected SE amplitudes for this epicentral distance, earthquakes with a typical depth of 6 km would have to exceed magnitude 3.2 to generate IRs larger than the low-noise-threshold

(Fig. 4.11b).
We now want to compare these estimates to a magnitude-distance-threshold derived by Dzieran et al. (2020) from observed data. The authors concluded that for a general noise-level lower than $10\,\mu\mathrm{V/m}$ there is a 67% chance to observe SE signals from earthquakes with magnitudes M higher than:

$$M = 2.7 \cdot log_{10}(r) \tag{4.7}$$

where r is the hypocentral distance. Following this threshold, an earthquake in 6 km depth could excite observable SE signals in 9 km distance under moderate noise conditions if its magnitude exceeds 2.8. An earthquake with the same depth but recorded in 1 km epicentral distance would have to exceed magnitude 2.1 to excite observable SE amplitudes. These magnitudes only partly match magnitude levels estimated in the present study. At 9 km epicentral distance and 6 km depth, events with magnitudes between 2.5 and 4.3 would excite amplitudes between 0.1 and $10\,\mu\mathrm{V/m}$. The magnitude of 2.8 calculated from equation 4.7 lies within these boundaries. For an epicentral distance of 1 km and a hypocentral depth of 6 km, magnitudes between 3 and 5 would be needed to excite amplitudes of the same order. At the same time, the magnitude-distance-threshold suggests a magnitude of 2.1 to be sufficient to excite observable signals with a chance of 67%. This discrepancy of magnitude-values implies that our numerical model may underestimate SE amplitudes. We will therefore discuss the limitations of our modelling, with special regard to the amplitude estimation, in the next section.

4.8.4.1 Limitations of the amplitude estimation

In section 4.7 we estimated the sizes of SE amplitudes that could be excited by earthquakes on the Armutlu-Peninsula in Turkey. We will now discuss how reliable these estimations are regarding certain limitations of our modelling:
1) Pride's theory: In the past, the application of Pride's formulations has been criticised (Revil, 2017), especially as it appears to not correctly represent the frequency dependency of the electrical conductivity. However, when the SE amplitudes calculated on the basis of Pride's theory were compared to SE amplitudes calculated with a conductivity approach suggested by Revil and Mahardika (2013), similar results were obtained (Zyserman et al., 2017). Furthermore, Gao et al. (2016) were able to simulate coseismic signals in the same order of magnitude as SE signals excited by the M_W 6 Parkfield-earthquake in Southern California using Pride's formulations. We see this as a confirmation that the order of magnitude of the computed SE amplitude is still realistic, even though the applied modelling code of Warden et al. (2013) is based on Pride's theory and its restrictions.
2) Model simplifications: We are aware that our modelling code does not and cannot include every factor that contributes to the actual size of the seismic and SE amplitudes. The intrinsic attenuation of the seismic amplitudes, for example, is simplified, and scattering due to lateral heterogeneity is ignored. These factors clearly need further investigation, especially regarding the interpretation of field data. Therefore, the presented results have to be regarded as order of magnitude estimates as stated above.

One more example of simplification is the assumption of a vertical point source. This reflects the reality of complicated source mechanisms only partially. To evaluate the amplitudes generated by the vertical point source, we additionally calculated the expected SE amplitudes caused by a horizontal point source. With the horizontal point source the coseismic amplitudes became four times larger while the IR amplitudes became four times smaller compared to the amplitudes generated by a vertical point source. This shows that even though the amplitudes depend on the applied source mechanism, they stay in the same range of magnitude, which justifies the simplification a posteriori. In the interpretation of field data a more ‘realistic’ modelling of the source mechanism would clearly be necessary.

3) Influence of the subsurface model: The choice of realistic subsurface parameters is the most important aspect of retrieving reliable SE amplitude sizes. The electric structure of the upper layer, for example, influences the damping factor of EM waves, which is inversely proportional to the subsurface resistivity, as well as the coseismic amplitudes, which are inversely proportional to the conductivity of the pore fluid (Garambois and Dietrich, 2001). The resistivity-depth distribution of the magnetotelluric model of the Armutlu Peninsula (Tank et al. (2003)) that we based our model-parameters upon shows only little resolution in the upper 500 m. Therefore, it is possible that observed SE amplitudes could actually be higher than expected and that the detection-threshold in terms of magnitude could be lower.

It is known that SE amplitudes are also influenced by the water saturation of the subsurface (e.g. Strahser et al., 2011; Warden et al., 2013). For the modelling we assumed full saturation of all layers. However, electrodes of MT-stations are usually placed in the vadose zone. Jardani and Revil (2015) found out that IRs can best be detected in relatively dry vadose zone. Similarly, Monachesi et al. (2018) stated that while coseismic amplitudes decrease with decreasing saturation, IR amplitudes increase.

The discussion in this section showed that there is a number of additional effects that will have to be considered in the interpretation of field measurements. Therefore, the presented results have to be considered as order-of-magnitude estimates enabling to assess the chance of success of a passive SE survey in a specific region.

4.8.4.2 Suggestions to improve passive SE recordings

In our case the amplitude estimations suggest that on the Armutlu Peninsula identifiable SE signals can be expected from large micro-seismicity events with magnitudes larger than 2 or 3, depending on hypocentral depth. The cumulative magnitude distribution shows that events with magnitudes between 2.5 and 3.2 occur 60 to 4 times a year, respectively (Fig. 4.2a). In this context, the question arises, if alternative techniques of data acquisition and processing could be applied to enable also SE recordings from smaller events. In this regard, we suggest the following approaches:

1) Stacking of single-event data recorded by arrays: One way to enhance IR signals may

be the stacking (summation) of signal amplitudes recorded over increasing distances following sets of predefined planes of arrival times. This could especially be used to enhance rIRs close to the epicenter as they travel with zero slowness. This will, however, only be helpful if the noise signals radiated from anthropogenic sources decay over even shorter distances than the rIRs amplitudes. Otherwise the noise signals will also occur on all traces of the array at the same time thus annihilating the stacking effort.
For eIRs the temporal moveout has to be considered in a potential array analysis. In this case a special difficulty lies in the spatial change of the signal frequencies. As seen in Figs 4.3c and f, the period of the eIRs becomes larger with increasing epicentral distance. Therefore a spectral balancing and phase adjustment will be required to generate coherency before stacking.
2) Stacking of single station data: Over time, microseismic events repeatedly occur in the same volume elements of the subsurface. If the monitoring array is capable to locate hypocenters with a high enough accuracy, it will be possible to stack repeated time-lapse events from the same subsurface volume elements at single MT stations to enhance SE signals. This may be suitable especially in case of repeatedly active seismicity clusters and swarms, which are frequently found in seismically active areas. This procedure may not only be applied to signals in the time domain, but it could be suitable for SESRs, too. Previous investigations have shown that SESRs are site specific (Dzieran et al., 2019, 2020). Due to the cancellation of the source spectrum it can be expected that the stacking of SESRs may be even more robust than that of time series.
3) Filtering of noise and coseismic signals: As mentioned before, anthropogenic noise is probably the biggest challenge for recording SE signals. Butler and Russell (1993) and Butler and Russell (2003) have proposed filtering techniques to remove powerline harmonics from SE records. These include the estimation and subtraction of harmonic frequencies to improve the signal-to-noise ratio of SE records. Furthermore Warden et al. (2012) suggested different filtering techniques to separate coseismic signals from IRs, to enhance the chance to identify IRs. The filtering techniques were demonstrated on a SE dataset acquired with an active seismic source and recorded by 24 closely-spaced dipoles. It therefore remains to be seen, whether this approach can be transferred to passively recorded SE signals, which usually are recorded with larger receiver distances.
4) Improving SE data acquisition: SE earthquake signals are usually recorded by MT-stations. This means that the horizontal electric field components are recorded via two electrodes that are spaced several to tens of meters apart from each other. Dietrich et al. (2018) and Devi et al. (2018) recently showed in two follow-up papers that this form of recording leads to a weakening of rIR amplitudes, as their wavefronts arrive nearly parallel to the earth's surface. They therefore suggest the use of multi-electrode patterns, such as chains of three or five electrodes per sensor to enhance IR amplitudes from the beginning. The authors have based their suggestions on numerical investigations and laboratory measurements aiming at exploration applications. It would be interesting and necessary to investigate, whether this method could lead to improved recordings of SE signals from earthquakes, too.

In summary, our synthetic site study of the Armutlu Peninsula implies that recording SE signals with standard MT stations requires seismic events of magnitudes $\geq$2 or $\geq$3 depending on hypocentral depths. When deploying the stations it should be taken care that they are placed close enough to the epicenter to enable the identification of IR-phases. The comparison with the empirical magnitude-distance-threshold (eq. 4.7) and the discussion of the model limitations (section 4.8.4.1) suggest that the computed SE amplitudes might underestimate the expected field data amplitudes. Therefore, the presented results can be regarded as a minimum estimate. Improved acquisition techniques as well as array stacking algorithms can improve the signal-to-noise ratio and lower the SE detection swell. Because of the noise- and distance sensitivity of the SE signals a thorough pre-examination of the possible investigation sites, including test measurements, will be necessary in field experiments.

4.9 Conclusion

In this study we investigated the SE responses to a multi-layer model resembling the subsurface conditions of the Armutlu Peninsula. The goal was to exemplarily investigate the detection swell of coseismic and IR amplitudes to assess whether SE measurements can be used to monitor temporal variations of hydro-geological parameters of near-surface aquifers in seismically active regions.

We found out that 1-10 km deep M2.5 earthquakes can excite coseismic P-phase signals that exceed a noise-threshold of 0.1 μV/m in 9 km epicentral distance. The coseismic signals arrive simultaneously to seismic P-waves. Due to their fast decreasing amplitudes, eIRs, which have a similar moveout as the seismic P-waves, and rIRs, which travel with zero slowness, can best be identified at epicentral distances around 1 km (expected amplitudes 0.02 μV/m for M2.5 in 6 km depth). At further distances, their amplitudes decrease to less than 2% of the coseismic amplitudes. In the frequency domain response behaviour caused by IRs can also best be observed at small epicentral distances.

To monitor subsurface changes, envelope analysis as well as SESRs can be used. Both methods are sensitive to porosity and salinity variations in up to 200 m depth. For realistic parameter variations the variation of SE signals is of the order of up to some 10%. Largest changes were obtained near the epicentre where the ratio between coseismic and IR amplitudes is close to 1. Permeability variations led to responses about 10 times smaller than those caused by porosity or salinity variation. The response of the envelopes was affected differently by porosity and salinity variations. While a porosity variation led to a larger response in the S-Phase, the P-phase response seemed to be more affected by salinity variations. For the SESRs the porosity variation resulted in a more randomly response than the salinity variation.

About 60 of the earthquakes that occur on the Armutlu Peninsula every year have magnitudes greater than 2.5. In order to identify SE signals in 1 km epicentral distance the earthquakes would have to exceed at least magnitude 3.2, which happens around 4 times per year. This means that repeat measurements may be possible if the observational time intervals are long enough. However, to enlarge the success rate, it will be necessary to develop more sophisticated data acquisition techniques including array and multi-electrode techniques.

Acknowledgments First of all, we would like to thank Dr. A. Revil and a second anonymous reviewer for their constructive comments. The Armutlu seismicity map (Fig. 4.1) was created with Generic Mapping Tools (GMT) software (Wessel et al., 2013). All other figures were created with Python (www.python.org) and the data was analysed with ObsPy (Krischer et al., 2015). The data used in this paper can be requested from the authors.

4.A Appendix

4.A.1 Model parameters

Tab. 4.4 lists the input parameters that describe the base-model used to calculate the SE responses analysed in sections 4.5 and 4.6. Parameters marked with (*) were calculated by the program. The corresponding equations can be found in Garambois and Dietrich (2002) and Warden et al. (2013).

The modelling code is mainly intended for near surface applications. To be able to model the resistivities suggested by Tank et al. (2003), high salinity values had to be chosen for greater depths. Using the Zeta-potential formula $\zeta = 0.008 \cdot 0.026 \cdot log_{10}(Salinity)$ of Pride and Morgan (1991) that is implemented in the modelling code leads to an unrealistically high zeta potential value. Jaafar et al. (2009) suggested that for high salinities (above 0.2 mol/l) the zeta-potential remains constant at around -0.02 V. We therefore used this value for the zeta potential of layers 3 to 6.

layer	1	2	3	4	5	6
depth [km]	0.5	1.0	2.0	5	10	>10
porosity [%]	5	1	0.1	0.1	0.1	0.1
saturation [-]	1.0	1.0	1.0	1.0	1.0	1.0
permeability [Darcy]	0.1	0.1	0.1	0.1	0.1	0.1
solid bulk modulus [GPa]	17.3	21.6	40.4	54.1	44.1	63.0
solid shear modulus [GPa]	11.4	13.2	24.3	32.5	26.5	37.9
fluid bulk modulus [GPa]	2.27	2.27	2.27	2.27	2.27	2.27
air bulk modulus [kPa]	100	100	100	100	100	100
consolidation parameter [-]	5	5	5	5	5	5
fluid viscosity [Pa $\cdot$ s]	0.001	0.001	0.001	0.001	0.001	0.001
air viscosity [Pa $\cdot$ s]	1.80E-05	1.8E-05	1.8E-05	1.8E-05	1.8E-05	1.8E-05
solid density [kg/m^3]	2367	2379	2590	2703	2622	2767
fluid density [kg/m^3]	1000	1000	1000	1000	1000	1000
air density [kg/m^3]	1	1	1	1	1	1
salinity [mol/l]	0.005	0.04	1.0	1.0	1.0	1.0
temperature [K]	300	300	300	300	300	300
fluid permittivity [-]	80	80	80	80	80	80
solid permittivity [-]	4	4	4	4	4	4
cementation exponent [-]	1.3	1.3	1.3	1.3	1.3	1.3
*v_P [km/s]	3.32	3.96	5.29	5.99	5.49	6.39
*v_S [km/s]	1.85	2.27	3.05	3.45	3.17	3.69
*v_{EM} at 15 Hz [km/s]	200	201	359	359	359	359
*density [kg/m^3]	2298	2365	2588	2701	2620	2765
*zeta potential [V]	-0.05	-0.03	-0.02	-0.02	-0.02	-0.02
*fluid conductivity [S/m]	0.046	0.37	9.28	9.28	9.28	9.28
* bulk resistivity [Ωm]	1059	1073	3409	3409	3409	3409

Tab. 4.4: *Input parameters of the base-model described in section 4.4 used to calculate SE responses analysed in sections 4.5 and 4.6. Parameters marked with (*) were computed by the program.*

5 Summary and Conclusion

When seismic waves propagate through the subsurface they can be accompanied by seismoelectric (SE) signals. A possible explanation for the generation of these signals are electrokinetic coupling effects in the electric double layer between the rock matrix and the fluid in the pore-space. SE signals are sensitive towards poroelastic and electrical properties while also providing the resolution of seismic waves. They are therefore an interesting but still not much explored investigation target.

In general, SE signals can be divided intro three categories: coseismic waves, interface responses (IRs) and signals associated to source-processes. IRs and coseismic signals have successfully been identified in SE exploration studies using an active source (e.g. Dupuis et al., 2007; Strahser et al., 2011; Butler et al., 2018), but SE signals can also be observed during earthquakes (e.g. Johnston, 2006; Huang, 2011; Sun et al., 2019). However, while numerous reports about coseismic signals during earthquakes exist, IRs and signals associated to source processes have not been observed in field data, yet.

The goal of this thesis is to broaden the knowledge about SE signals generated by earthquakes. The focus thereby lies on the possibility to detect coseismic signals and IRs during earthquakes, new approaches to analyse said signals and the opportunities that lie in their interpretation. The main results of this thesis will now be summarised by answering the questions stated in the introduction (chapter 1). Following that, a short outlook on possible future investigations is provided before presenting a final conclusion.

5.1 Under which conditions can seismoelectric signals from earthquakes best be detected?

The most likely SE wavetype to be detected during an earthquake are coseismic signals. In the SE wavetrain they usually have the largest amplitudes and are easy to identify due to their simultaneous onset with the seismic waves (see section 4.5.1).

In chapter 2 we established logarithmic distance-magnitude thresholds from over 16,000 earthquakes recorded mainly in Northern Chile and Costa Rica. The thresholds quantify the chance to observe (coseismic) SE signals from earthquakes with a given magnitude at a distinct radius. For an average noise level below 0.1 µV/m, events of magnitude 4, 5 or 6 have a 67 % chance of being identified if their hypocentres are not further than 50, 150 or 400 km away from the registration unit (equation 2.3). For a maximum noise level of 10 µV/m the largest distances to at least partly identify SE signals with a chance of 67 % decreases to approximately 30, 70 and 170 km for earthquakes of the same magnitudes (equation 2.1, see section 2.3).

IRs are harder to detect in the SE wavetrain than coseismic waves. In general they have smaller amplitudes and decay fast. Radiant IRs (rIRs) can theoretically be identified through their simultaneously onset in different locations, whereas evanescent IRs (eIRs) have a similar move-out as the coseismic waves. However, as IRs are usually superimposed by (larger) coseismic signals their identification in the SE wavetrain is difficult. The IRs easiest to identify would therefore be those, arriving shortly before the first coseismic onsets (see section 4.5.1).

On the example of the Armutlu Peninsula in Turkey we showed that IRs can best be observed when the recording station is located close to the epicenter of the earthquake (< 10 km, depending on hypocentral depth and magnitude). In that case IRs and coseismic amplitudes are expected to be small but of similar size. Assuming the estimated amplitudes for the Armutlu Peninsula (see section 4.8), earthquakes with magnitudes of at least 3.2 would be needed to excite identifiable signals that exceed a general noise-level of 0.1 μV/m, depending on hypocentral distance.

Although the studies of the distance-magnitude thresholds (chapter 2) and the IR amplitude estimations (chapter 4) were conducted for two different continents (Northern Chile and Costa Rica vs. Turkey) with different investigation targets (coseismic field data vs. synthetic IR estimates), their general results are helpful when looking for a suitable location to conduct successful passive SE field measurements. The main conclusion of both studies is that the radius in which SE signals from earthquakes can be observed is limited. The size of the radius thereby depends on the observation-target (IRs or coseismic signals), the magnitude of the expected earthquakes and the anthropogenic noise-level.

SE signals can in general be recorded with customary electrode configurations. SE signals generated by earthquakes are usually observed with standard state-of-the-art magnetotelluric stations (MT). As MT stations are meant to record signals over a longer period of time, they provide the perfect conditions for passive SE experiments. One could however also try to record SE signals with multi-electrode configurations as suggested by Devi et al. (2018) and Dietrich et al. (2018). According to them, multi-electrode configurations could enhance the amplitudes of rIRs, which would increase the detection radius of IR signals and decrease the dependability on the anthropogenic noise level.

All in all, one can conclude that SE signals can best be detected in secluded areas where earthquakes with large magnitudes happen in a confined space at moderate to high repetition rates. These areas could for example be locations with on-going swarm-activities or regions of aftershocks. Unconventional electrode configurations could thereby help to improve the measuring results. However, if one wants to record SE signals from earthquakes, test measurements should be conducted beforehand in order to estimate the local noise-level.

5.2 How can seismoelectric signals from earthquakes be analysed?

As stated before, single IRs are difficult to identify in the time domain. We therefore developed the concept of seismoelectric spectral ratios (SESRs) to analyse SE signals in the frequency domain. We proposed that if the electric coseismic field and the seismic acceleration are proportional to each other, the ratio of the respective spectra should be frequency independent. Hence, any deviation from this frequency independence should be directly related to IRs (see section 3.2).

In this thesis we presented SESRs calculated from field data in Northern Chile (chapters 2 and 3). We successfully remodelled an average SESR for an exemplary location before applying an inversion algorithm on the subsurface model to iteratively improve the results. This showed that if enough preliminary knowledge is available to constrain the calculations, subsurface parameters can possibly be approximated through analysing SESRs (chapter 3). Nevertheless, the assumption that coseismic and seismic signals are proportional to each other must be treated with caution. Within near epicentral distances a proportionality might not be given, especially when shear movement is predominant in the signal's composition. In that case the appearing frequency dependency of the SESRs is not caused by IRs (see section 4.5.2). However, as this circumstance can most likely be verified by modelling, it does not disqualify SESRs from being used as an analysing tool.

An alternative approach to investigating SE signals is envelope-analysis in the time domain. When envelopes are analysed the focus is shifted from single (IR) amplitudes to the whole wavetrain. This is especially useful when data-sets from different earthquakes are compared as alterations can easily be recognised. In this thesis we used envelopes to calculate scaling factors between the seismic and SE records, for example, revealing varying site responses (chapter 2). Additionally the comparison of SE envelopes enabled us to detect subsurface variations in up to 200 m depth (chapter 4).

All in all, we were able to show that although the direct identification of IRs is difficult, the analysis of the complete SE wavetrain can reveal valuable subsurface information. SESRs thereby provide a new approach to investigate SE signals in the frequency domain whereas in the time domain envelope-analysis is a useful way to compare SE records.

5.3 How can seismoelectric signals from earthquakes be interpreted?

The comparison of SESRs and envelopes from earthquakes recorded in the Atacama Desert of Northern Chile revealed that SE signals are site dependent (see section 2.4). The frequency-dependent decreasing trends of the SESRs were similar on the same stations for different earthquakes whereas they differed for the same earthquake recorded at different stations. Similarly, the scaling factors between the seismic and coseismic envelopes were in the same order of magnitude in one location but showed a variation between different recording stations of up to 200 %. This confirms that SE signals do indeed reflect local subsurface conditions (chapter 2).

In this thesis we conducted different sensitivity analyses to find out which subsurface parameters could be a possible target for SE investigations. The computations revealed that SESRs as well as SE envelopes are sensitive towards changes of porosity and the pore-fluid's salinity in the first few hundred metres of the subsurface. These are parameters that cannot be evaluated by seismic measurements alone. While the P- and S-phase of the SE envelopes were affected differently by synthetic porosity and salinity changes, such an obvious distinction could not be made for SESRs. These were however affected

by changing depths of the IR-generating interfaces. A strong sensitivity towards permeability as suggested by Garambois and Dietrich (2002) could neither be confirmed for SESRs nor for envelopes, although one reason for that could be the chosen range of the investigated permeability (see chapters 3 and 4).
Summing up, our investigations showed that SE signals from earthquakes are site-dependent and primarily sensitive to local porosity and pore-fluid's salinity values as well as the depth of the IR generating interfaces. Depending on the magnitude of the earthquake and the hypocentral distance to the recording station, effects from parameter changes in the first few hundred meters of the subsurface can be detected through SESRs and envelope-analysis. The biggest challenge when interpreting SE signals is probably the distinction between the effects caused by different parameter variations. Preliminary knowledge from other sources will therefore most likely be necessary to constrain possible interpretations.

5.4 Outlook

The studies presented in this thesis show that if a sufficient data quality is given, SESRs and envelope-analysis of SE signals might be able to provide information about local subsurface parameters. However, as these conclusion were mostly obtained through numerical computations, the consequent next step will have to be an actual SE field campaign to validate these assumptions. Said field experiment is most likely to be successful if the recording stations are located within small epicentral distances towards large magnitude earthquakes in areas with little anthropogenic noise. Such locations could for example be found near active faults, subduction zones or in areas with volcanic activity. The Armutlu Peninsula in Turkey could become a possible investigation site considering the regular appearance of shallow earthquakes in a closely confined area. The small magnitudes of the earthquakes can however pose a problem, especially since the local noise-level is unknown. It is therefore necessary to conduct test measurements before setting up a large-scale or long-term field experiment, to find out whether SE signal from earthquakes can actually be detected with the sufficient data quality (see chapter 4).
When a suitable location for a field experiment is identified, it would be interesting to deploy multiple receivers in close distance to each other. In that case it is not only possible to test the potential of applying SESRs and envelope-analysis, but the influence of lateral changes in the subsurface could also be investigated. It is important to find out over which lateral extend the SE signals can deliver reliable information. Moreover with closely spaced stations, stacking techniques could be explored to enhance the signal-to-noise ratio, improving the chance to directly identify IR amplitudes in the SE wavetrain.
A last aspect worth investigating in a field experiment is the 3D dependency of the SE signals. The field data presented in chapter 2 seems to be highly influenced by 3D scattering, shown by the fact that the same characteristics can be observed for data from the radial as well as transversal components. Sun et al. (2019) recently showed how modelling results can be improved by taking scattering effects into account. To better understand SE field data it is necessary to further investigate this phenomenon to find out up to which degree it influences the signals.

While a field experiment is probably the most necessary next step, other aspects of SE research should not be neglected. Similar to what was presented in section 2.3 analysing large SE data-sets for different parts of the world could help answer the question, whether a global distance-magnitude threshold for observing SE signals can be established or if local conditions influence the SE signals so strongly that local thresholds are necessary in different regions. Furthermore, the relationship between the anthropogenic noise-level and the detectability of SE signals could be investigated. The data presented in section 2.3 show that for earthquakes of the same magnitude the radius in which SE signals are identifiable decreases significantly with increasing anthropogenic noise. If a relationship between the noise-level and the detection radius could be established, a quick assessment of the local noise conditions could be sufficient to determine if a location is suitable for SE measurements.

Last but not least, the research on SESRs needs to be continued. We showed that SESRs can potentially be used to analyse the subsurface. It is now necessary to test this method for different locations and with different data-sets to verify its reliability. Furthermore different inversion algorithms should be tested and evaluated. Finally it could be considered to transfer the SESR-approach from data recorded during earthquakes to data gathered during active SE field campaigns to test if SESRs are also applicable for this kind of field data.

Obviously, a lot of open questions remain concerning the analysis of SE signals from earthquakes. Many of these questions can best be answered via actual field measurements. In the next few years the acquisition and analysis of field records should therefore become a priority, as this is the best way to enhance our knowledge about SE earthquake signals and their potential to study the subsurface.

5.5 Conclusion

In this thesis we investigated SE signals generated by earthquakes. SE signals can best be detected if the magnitudes of the earthquakes are large enough for the generated SE amplitudes to overcome the anthropogenic noise-level in a certain epicentral distance. While coseismic signals can be observed more than 400 km away from the earthquake source, IRs are most likely to be identified in close vicinity to the epicenter. When investigating SE signals, SESRs and envelope-analysis provide ways to obtain subsurface information without having to focus on single IR amplitudes. SE signals from earthquakes are site-dependent and sensitive towards porosity and the salinity of the pore-fluid in the first few hundred meters of the subsurface. It might therefore be possible to extract subsurface information from SE signals that cannot be obtained by seismic measurements alone. Nevertheless, as these assumptions are largely based on numeric calculations, field measurements need to be conducted to evaluate the actual potential of SE signals generated by earthquakes.

Bibliography

Allègre, V., L. Jouniaux, F. Lehmann, and P. Sailhac, 2010: Streaming potential dependence on water-content in Fontainebleau sand. *Geophysical Journal International*, **182 (3)**, 1248–1266, doi:10.1111/j.1365-246x.2010.04716.x.

Araya Vargas, J., and O. Ritter, 2015: Source effects in mid-latitude geomagnetic transfer functions. *Geophysical Journal International*, **204 (1)**, 606–630, doi:10.1093/gji/ggv474.

Araya Vargas, J. A., 2016: Large-scale distribution of fluids in the subduction zone of Northern Chile–constraints from magnetotelluric monitoring. Ph.D. thesis, Freie Universität Berlin.

Baris, S., 2002: Microearthquake Activity before the Izmit Earthquake in the Eastern Marmara Region, Turkey (1 January 1993-17 August 1999). *Bulletin of the Seismological Society of America*, **92 (1)**, 394–405, doi:10.1785/0120000826.

Barka, A., and Coauthors, 2002: The Surface Rupture and Slip Distribution of the 17 August 1999 Izmit Earthquake (M 7.4), North Anatolian Fault. *Bulletin of the Seismological Society of America*, **92 (1)**, 43–60, doi:10.1785/0120000841.

Bekler, T., and C. Gurbuz, 2008: Insight into the Crustal Structure of the Eastern Marmara Region, NW Turkey. *Pure and Applied Geophysics*, **165 (2)**, 295–309, doi:10.1007/s00024-008-0302-3.

Biot, M. A., 1956: Theory of Propagation of Elastic Waves in a Fluid-Saturated Porous Solid. I. Low-Frequency Range. *The Journal of the Acoustical Society of America*, **28 (2)**, 168–178, doi:10.1121/1.1908239.

Biot, M. A., 1962: Mechanics of Deformation and Acoustic Propagation in Porous Media. *Journal of Applied Physics*, **33 (4)**, 1482–1498, doi:10.1063/1.1728759.

Blau, L. W., and L. Statham, 1936: US Patent 2,054,067. Method and apparatus for seismicelectric prospecting.

Block, G. I., and J. G. Harris, 2006: Conductivity dependence of seismoelectric wave phenomena in fluid-saturated sediments. *Journal of Geophysical Research*, **111 (B1)**, doi:10.1029/2005jb003798.

Bogazici University Kandilli Observatory And Earthquake Research Institute, 2001: Bogazici University Kandilli Observatory And Earthquake Research Institute. International Federation of Digital Seismograph Networks, doi:10.7914/sn/ko.

Borcherdt, R. D., 1970: Effects of local geology on ground motion near San Francisco Bay. *Bulletin of the Seismological Society of America*, **60** (**1**), 29–61.

Bordes, C., L. Jouniaux, S. Garambois, M. Dietrich, J.-P. Pozzi, and S. Gaffet, 2008: Evidence of the theoretically predicted seismo-magnetic conversion. *Geophysical Journal International*, **174** (**2**), 489–504, doi:10.1111/j.1365-246x.2008.03828.x.

Bordes, C., P. Sénéchal, J. Barrière, D. Brito, E. Normandin, and D. Jougnot, 2015: Impact of water saturation on seismoelectric transfer functions: a laboratory study of coseismic phenomenon. *Geophysical Journal International*, **200** (**3**), 1317–1335, doi:10.1093/gji/ggu464.

Bormann, P., K. Klinge, and S. Wendt, 2002: Chapter 11: data analysis and seismogram interpretation. *IASPEI new manual of seismological observatory practice*, **1**, 89–98.

Bormann, P., S. Wendt, and D. DiGiacomo, 2013: Seismic Sources and Source Parameters. *New Manual of Seismological Observatory Practice 2 (NMSOP2)*, doi:10.2312/gfz.nmsop-2_ch3.

Butler, K. E., B. Kulessa, and A. J.-M. Pugin, 2018: Multimode seismoelectric phenomena generated using explosive and vibroseis sources. *Geophysical Journal International*, **213** (**2**), 836–850, doi:10.1093/gji/ggy017.

Butler, K. E., and R. D. Russell, 1993: Subtraction of powerline harmonics from geophysical records. *GEOPHYSICS*, **58** (**6**), 898–903, doi:10.1190/1.1443474.

Butler, K. E., and R. D. Russell, 2003: Cancellation of multiple harmonic noise series in geophysical records. *GEOPHYSICS*, **68** (**3**), 1083–1090, doi:10.1190/1.1581080.

Butler, K. E., R. D. Russell, A. W. Kepic, and M. Maxwell, 1996: Measurement of the seismoelectric response from a shallow boundary. *GEOPHYSICS*, **61** (**6**), 1769–1778, doi:10.1190/1.1444093.

Çakir, Z., J.-B. de Chabalier, R. Armijo, B. Meyer, A. Barka, and G. Peltzer, 2003: Coseismic and early post-seismic slip associated with the 1999 Izmit earthquake (Turkey), from SAR interferometry and tectonic field observations. *Geophysical Journal International*, **155** (**1**), 93–110, doi:10.1046/j.1365-246x.2003.02001.x.

Cesca, S., F. Grigoli, S. Heimann, T. Dahm, M. Kriegerowski, M. Sobiesiak, C. Tassara, and M. Olcay, 2016: The Mw8.1 2014 Iquique, Chile, seismic sequence: a tale of foreshocks and aftershocks. *Geophysical Journal International*, **204** (**3**), 1766–1780, doi:10.1093/gji/ggv544.

Charmoille, A., O. Fabbri, J. Mudry, Y. Guglielmi, and C. Bertrand, 2005: Post-seismic permeability change in a shallow fractured aquifer following a ML5.1 earthquake (Fourbanne karst aquifer, Jura outermost thrust unit, eastern France). *Geophysical Research Letters*, **32** (**18**), n/a–n/a, doi:10.1029/2005gl023859.

Devi, M., 2017: Experimental and numerical investigations of the coupled seismic and electromagnetic wave-fields propagation in saturated unconsolidated materials. Ph.D. thesis, Université Grenoble Alpes, URL https://tel.archives-ouvertes.fr/tel-01682910.

Devi, M. S., S. Garambois, D. Brito, M. Dietrich, V. Poydenot, and C. Bordes, 2018: A novel approach for seismoelectric measurements using multielectrode arrangements: II—Laboratory measurements. *Geophysical Journal International*, **214** **(3)**, 1783–1799, doi:10.1093/gji/ggy251.

Dietrich, M., M. S. Devi, S. Garambois, D. Brito, and C. Bordes, 2018: A novel approach for seismoelectric measurements using multielectrode arrangements – I: theory and numerical experiments. *Geophysical Journal International*, **215** **(1)**, 61–80, doi: 10.1093/gji/ggy269.

Dupuis, J. C., K. E. Butler, and A. W. Kepic, 2007: Seismoelectric imaging of the vadose zone of a sand aquifer. *GEOPHYSICS*, **72** **(6)**, A81–A85, doi:10.1190/1.2773780.

Dzieran, L., W. Rabbel, M. Thorwart, and O. Ritter, 2020: Seismoelectric ground response to local and regional earthquakes. *Seismoelectric exploration: Theory, experiments and applications*, N. Grobbe, A. Revil, Z. Zhu, and E. Slob, Eds., Wiley Online Library, in press.

Dzieran, L., M. Thorwart, W. Rabbel, and O. Ritter, 2019: Quantifying interface responses with seismoelectric spectral ratios. *Geophysical Journal International*, **217** **(1)**, 108–121, doi:10.1093/gji/ggz010.

Elkhoury, J. E., E. E. Brodsky, and D. C. Agnew, 2006: Seismic waves increase permeability. *Nature*, **441** **(7097)**, 1135–1138, doi:10.1038/nature04798.

Frenkel, J., 1944: To the theory of seismic and seismoelectric phenomena in saturated soil. *Izv. Acad. Nauk USSR*, **8** **(4)**.

Frenkel, J., 2005: On the Theory of Seismic and Seismoelectric Phenomena in a Moist Soil. *Journal of Engineering Mechanics*, **131** **(9)**, 879–887, doi:10.1061/(asce) 0733-9399(2005)131:9(879).

Gao, Y., X. Chen, H. Hu, J. Wen, J. Tang, and G. Fang, 2014: Induced electromagnetic field by seismic waves in Earth's magnetic field. *Journal of Geophysical Research: Solid Earth*, **119** **(7)**, 5651–5685, doi:10.1002/2014jb010962.

Gao, Y., X. Chen, H. Hu, and J. Zhang, 2013: Early electromagnetic waves from earthquake rupturing: II. validation and numerical experiments. *Geophysical Journal International*, **192** **(3)**, 1308–1323, doi:10.1093/gji/ggs097.

Gao, Y., J. M. Harris, J. Wen, Y. Huang, C. Twardzik, X. Chen, and H. Hu, 2016: Modeling of the coseismic electromagnetic fields observed during the 2004 Mw6.0 Parkfield earthquake. *Geophysical Research Letters*, **43** **(2)**, 620–627, doi:10.1002/ 2015gl067183.

Gao, Y., and H. Hu, 2010: Seismoelectromagnetic waves radiated by a double couple source in a saturated porous medium. *Geophysical Journal International*, doi:10.1111/j.1365-246x.2010.04526.x.

Garambois, S., and M. Dietrich, 2001: Seismoelectric wave conversions in porous media: Field measurements and transfer function analysis. *GEOPHYSICS*, **66 (5)**, 1417–1430, doi:10.1190/1.1487087.

Garambois, S., and M. Dietrich, 2002: Full waveform numerical simulations of seismo-electromagnetic wave conversions in fluid-saturated stratified porous media. *Journal of Geophysical Research: Solid Earth*, **107 (B7)**, ESE 5–1–ESE 5–18, doi:10.1029/2001jb000316.

GEOFON Data Centre, 1993: GEOFON Seismic Network. Deutsches GeoForschungsZentrum GFZ, URL https://geofon.gfz-potsdam.de, doi:10.14470/tr560404.

Gershenzon, N., M. Gokhberg, and S. Yunga, 1993: On the electromagnetic field of an earthquake focus. *Physics of the Earth and Planetary Interiors*, **77 (1-2)**, 13–19, doi:10.1016/0031-9201(93)90030-d.

Gershenzon, N. I., G. Bambakidis, and I. Ternovskiy, 2014: Coseismic electromagnetic field due to the electrokinetic effect. *GEOPHYSICS*, **79 (5)**, E217–E229, doi:10.1190/geo2014-0125.1.

GFZ German Research Centre For Geosciences, and Institut Des Sciences De L'Univers-Centre National De La Recherche CNRS-INSU, 2006: IPOC Seismic Network. Integrated Plate boundary Observatory Chile - IPOC, http://www.ipoc-network.org, doi:10.14470/pk615318.

Grobbe, N., and E. C. Slob, 2016: Seismo-electromagnetic thin-bed responses: Natural signal enhancements? *Journal of Geophysical Research: Solid Earth*, **121 (4)**, 2460–2479, doi:10.1002/2015jb012381.

Guichet, X., L. Jouniaux, and J.-P. Pozzi, 2003: Streaming potential of a sand column in partial saturation conditions. *Journal of Geophysical Research: Solid Earth*, **108 (B3)**, doi:10.1029/2001jb001517.

Haartsen, M. W., and S. R. Pride, 1997: Electroseismic waves from point sources in layered media. *Journal of Geophysical Research: Solid Earth*, **102 (B11)**, 24 745–24 769, doi:10.1029/97jb02936.

Hartmann, J., and J. K. Levy, 2005: Hydrogeological and Gasgeochemical Earthquake Precursors? A Review for Application. *Natural Hazards*, **34 (3)**, 279–304, doi:10.1007/s11069-004-2072-2.

Havskov, J., and L. Ottemoller, 2010: *Routine Data Processing in Earthquake Seismology*. Springer Netherlands, doi:10.1007/978-90-481-8697-6.

Holzhauer, J., D. Brito, C. Bordes, Y. Brun, and B. Guatarbes, 2016: Experimental quantification of the seismoelectric transfer function and its dependence on conductivity and saturation in loose sand. *Geophysical Prospecting*, **65 (4)**, 1097–1120, doi: 10.1111/1365-2478.12448.

Honkura, Y., and Coauthors, 2000: Preliminary results of multidisciplinary observations before, during and after the Kocaeli (Izmit) earthquake in the western part of the North Anatolian Fault Zone. *Earth, Planets and Space*, **52 (4)**, 293–298, doi: 10.1186/bf03351638.

Hu, H., and Y. Gao, 2011: Electromagnetic field generated by a finite fault due to electrokinetic effect. *Journal of Geophysical Research*, **116 (B8)**, doi:10.1029/2010jb007958.

Huang, Q., 2002: One possible generation mechanism of co-seismic electric signals. *Proceedings of the Japan Academy. Ser. B: Physical and Biological Sciences*, **78 (7)**, 173–178, doi:10.2183/pjab.78.173.

Huang, Q., 2011: Retrospective investigation of geophysical data possibly associated with the Ms8.0 Wenchuan earthquake in Sichuan, China. *Journal of Asian Earth Sciences*, **41 (4-5)**, 421–427, doi:10.1016/j.jseaes.2010.05.014.

International Seismological Centre, 2015: *On-line Bulletin*. Thatcham, United Kingdom, Internatl. Seismol. Cent., doi:10.31905/d808b830, http://www.isc.ac.uk.

Ivanov, A., 1939: Effect of electrization of earth layers by elastic waves passing through them. *Doklady Akademii Nauk SSSR*, **24 (1)**, 42–45.

Jaafar, M. Z., J. Vinogradov, and M. D. Jackson, 2009: Measurement of streaming potential coupling coefficient in sandstones saturated with high salinity NaCl brine. *Geophysical Research Letters*, **36 (21)**, doi:10.1029/2009gl040549.

Jardani, A., and A. Revil, 2015: Seismoelectric couplings in a poroelastic material containing two immiscible fluid phases. *Geophysical Journal International*, **202 (2)**, 850–870, doi:10.1093/gji/ggv176.

Jardani, A., A. Revil, E. Slob, and W. Söllner, 2010: Stochastic joint inversion of 2D seismic and seismoelectric signals in linear poroelastic materials: A numerical investigation. *GEOPHYSICS*, **75 (1)**, N19–N31, doi:10.1190/1.3279833.

Johnston, M. J. S., 2006: Seismomagnetic Effects from the Long-Awaited 28 September 2004 M 6.0 Parkfield Earthquake. *Bulletin of the Seismological Society of America*, **96 (4B)**, S206–S220, doi:10.1785/0120050810.

Jouniaux, L., and F. Zyserman, 2016: A review on electrokinetically induced seismoelectrics, electro-seismics, and seismo-magnetics for Earth sciences. *Solid Earth*, **7 (1)**, 249–284, doi:10.5194/se-7-249-2016.

Karabulut, H., S. Özalaybey, T. Taymaz, M. Aktar, O. Selvi, and A. Kocaoğlu, 2003: A tomographic image of the shallow crustal structure in the Eastern Marmara. *Geophysical Research Letters*, **30 (24)**, doi:10.1029/2003gl018074.

Kinscher, J., F. Krüger, H. Woith, B. Lühr, E. Hintersberger, T. Irmak, and S. Baris, 2013: Seismotectonics of the Armutlu peninsula (Marmara Sea, NW Turkey) from geological field observation and regional moment tensor inversion. *Tectonophysics*, **608**, 980–995, doi:10.1016/j.tecto.2013.07.016.

Konno, K., and T. Ohmachi, 1998: Ground-motion characteristics estimated from spectral ratio between horizontal and vertical components of microtremor. *Bulletin of the Seismological Society of America*, **88 (1)**, 228–241.

Krischer, L., T. Megies, R. Barsch, M. Beyreuther, T. Lecocq, C. Caudron, and J. Wassermann, 2015: ObsPy: a bridge for seismology into the scientific Python ecosystem. *Computational Science & Discovery*, **8 (1)**, 014 003, doi:10.1088/1749-4699/8/1/014003.

Kröger, B., U. Yaramanci, and A. Kemna, 2013: Numerical analysis of seismoelectric wave propagation in spatially confined geological units. *Geophysical Prospecting*, **62 (1)**, 133–147, doi:10.1111/1365-2478.12020.

Lines, L., and S. Treitel, 1984: A review of least-squares inversion and its application to geophysical problems. *Geophysical Prospecting*, **32 (2)**, 159–186, doi:10.1111/j.1365-2478.1984.tb00726.x.

Mahardika, H., A. Revil, and A. Jardani, 2012: Waveform joint inversion of seismograms and electrograms for moment tensor characterization of fracking events. *GEOPHYSICS*, **77 (5)**, ID23–ID39, doi:10.1190/geo2012-0019.1.

Manga, M., I. Beresnev, E. E. Brodsky, J. E. Elkhoury, D. Elsworth, S. E. Ingebritsen, D. C. Mays, and C.-Y. Wang, 2012: Changes in permeability caused by transient stresses: Field observations, experiments, and mechanisms. *Reviews of Geophysics*, **50 (2)**, doi:10.1029/2011rg000382.

Martner, S. T., and N. R. Sparks, 1959: THE ELECTROSEISMIC EFFECT. *GEOPHYSICS*, **24 (2)**, 297–308, doi:10.1190/1.1438585.

Matsushima, M., Y. Honkura, M. Kuriki, and Y. Ogawa, 2013: Circularly polarized electric fields associated with seismic waves generated by blasting. *Geophysical Journal International*, **194 (1)**, 200–211, doi:10.1093/gji/ggt110.

Matsushima, M., and Coauthors, 2002: Seismoelectromagnetic Effect Associated with the Izmit Earthquake and Its Aftershocks. *Bulletin of the Seismological Society of America*, **92 (1)**, 350–360, doi:10.1785/0120000807.

Monachesi, L. B., F. I. Zyserman, and L. Jouniaux, 2018: An analytical solution to assess the SH seismoelectric response of the vadose zone. *Geophysical Journal International*, **213 (3)**, 1999–2019, doi:10.1093/gji/ggy101.

Nagao, T., Y. Orihara, T. Yamaguchi, I. Takahashi, K. Hattori, Y. Noda, K. Sayanagi, and S. Uyeda, 2000: Co-seismic geoelectric potential changes observed in Japan. *Geophysical Research Letters*, **27 (10)**, 1535–1538, doi:10.1029/1999gl005440.

Pride, S., 1994: Governing equations for the coupled electromagnetics and acoustics of porous media. *Physical Review B*, **50 (21)**, 15 678–15 696, doi:10.1103/physrevb.50.15678.

Pride, S. R., and S. Garambois, 2005: Electroseismic Wave Theory of Frenkel and More Recent Developments. *Journal of Engineering Mechanics*, **131 (9)**, 898–907, doi:10.1061/(asce)0733-9399(2005)131:9(898).

Pride, S. R., and M. W. Haartsen, 1996: Electroseismic wave properties. *The Journal of the Acoustical Society of America*, **100 (3)**, 1301–1315, doi:10.1121/1.416018.

Pride, S. R., and F. D. Morgan, 1991: Electrokinetic dissipation induced by seismic waves. *GEOPHYSICS*, **56 (7)**, 914–925, doi:10.1190/1.1443125.

Rabbel, W., K. Iwanowski-Strahser, M. Strahser, L. Dzieran, and M. Thorwart, 2020: Seismoelectric field measurements in unconsolidated sediments in comparison with other methods of near-surface prospecting. *Seismoelectric exploration: Theory, experiments and applications*, N. Grobbe, A. Revil, Z. Zhu, and E. Slob, Eds., Wiley Online Library, in press.

Ren, H., Q. Huang, and X. Chen, 2010: A new numerical technique for simulating the coupled seismic and electromagnetic waves in layered porous media. *Earthquake Science*, **23 (2)**, 167–176, doi:10.1007/s11589-009-0071-9.

Ren, H., Q. Huang, and X. Chen, 2015: Existence of evanescent electromagnetic waves resulting from seismoelectric conversion at a solid–porous interface. *Geophysical Journal International*, **204 (1)**, 147–166, doi:10.1093/gji/ggv400.

Ren, H., Q. Huang, and X. Chen, 2018: Quantitative Understanding on the Amplitude Decay Characteristic of the Evanescent Electromagnetic Waves Generated by Seismoelectric Conversion. *Pure and Applied Geophysics*, **175 (8)**, 2853–2879, doi:10.1007/s00024-018-1823-z.

Ren, H., J. Wen, Q. Huang, and X. Chen, 2014: Electrokinetic effect combined with surface-charge assumption: a possible generation mechanism of coseismic EM signals. *Geophysical Journal International*, **200 (2)**, 837–850, doi:10.1093/gji/ggu435.

Revil, A., 2015: *The Seismoelectric Method*. Wiley-Blackwell, URL https://www.ebook.de/de/product/23546059/andre_revil_the_seismoelectric_method.html.

Revil, A., 2017: Comment on “Dependence of shear wave seismoelectrics on soil textures: a numerical study in the vadose zone” by F.I. Zyserman, L.B. Monachesi and L. Jouniaux. *Geophysical Journal International*, **209** **(2)**, 1095–1098, doi:10.1093/gji/ggx078.

Revil, A., G. Barnier, M. Karaoulis, P. Sava, A. Jardani, and B. Kulessa, 2013: Seismoelectric coupling in unsaturated porous media: theory, petrophysics, and saturation front localization using an electroacoustic approach. *Geophysical Journal International*, **196** **(2)**, 867–884, doi:10.1093/gji/ggt440.

Revil, A., and A. Jardani, 2010: Seismoelectric response of heavy oil reservoirs: theory and numerical modelling. *Geophysical Journal International*, **180** **(2)**, 781–797, doi:10.1111/j.1365-246x.2009.04439.x.

Revil, A., N. Linde, A. Cerepi, D. Jougnot, S. Matthäi, and S. Finsterle, 2007: Electrokinetic coupling in unsaturated porous media. *Journal of Colloid and Interface Science*, **313** **(1)**, 315–327, doi:10.1016/j.jcis.2007.03.037.

Revil, A., and H. Mahardika, 2013: Coupled hydromechanical and electromagnetic disturbances in unsaturated porous materials. *Water Resources Research*, **49** **(2)**, 744–766, doi:10.1002/wrcr.20092.

Rojstaczer, S., and S. Wolf, 1992: Permeability changes associated with large earthquakes: An example from Loma Prieta, California. *Geology*, **20** **(3)**, 211–214, doi:10.1130/0091-7613(1992)020<0211:PCAWLE>2.3.CO;2.

Rojstaczer, S., S. Wolf, and R. Michel, 1995: Permeability enhancement in the shallow crust as a cause of earthquake-induced hydrological changes. *Nature*, **373** **(6511)**, 237–239, doi:10.1038/373237a0.

Russell, R. D., K. E. Butler, A. W. Kepic, and M. Maxwell, 1997: Seismoelectric exploration. *The Leading Edge*, **16** **(11)**, 1611–1615, doi:10.1190/1.1437536.

Schakel, M. D., D. M. J. Smeulders, E. C. Slob, and H. K. J. Heller, 2011: Laboratory measurements and theoretical modeling of seismoelectric interface response and coseismic wave fields. *Journal of Applied Physics*, **109** **(7)**, 074 903, doi:10.1063/1.3567945.

Scholz, C. H., 2019: *The Mechanics of Earthquakes and Faulting*. Cambridge University Press, URL https://www.ebook.de/de/product/33155884/christopher_h_scholz_the_mechanics_of_earthquakes_and_faulting.html.

Schurr, B., and Coauthors, 2014: Gradual unlocking of plate boundary controlled initiation of the 2014 Iquique earthquake. *Nature*, **512** **(7514)**, 299–302, doi:10.1038/nature13681.

Shi, Z., and G. Wang, 2014: Sustained groundwater level changes and permeability variation in a fault zone following the 12 May 2008, Mw7.9 Wenchuan earthquake. *Hydrological Processes*, **29 (12)**, 2659–2667, doi:10.1002/hyp.10387.

Sibson, R. H., 1981: Fluid Flow Accompanying Faulting: Field Evidence and Models. *Earthquake prediction: an international review, Maurice Ewing Series 4*, American Geophysical Union, 593–603, doi:10.1029/me004p0593.

Sick, C., and Coauthors, 2006: Seismic Images of Accretive and Erosive Subduction Zones from the Chilean Margin. *The Andes*, Springer Berlin Heidelberg, 147–169, doi: 10.1007/978-3-540-48684-8_7.

Skelton, A., and Coauthors, 2014: Changes in groundwater chemistry before two consecutive earthquakes in Iceland. *Nature Geoscience*, **7 (10)**, 752–756, doi:10.1038/ngeo2250.

Strahser, M., L. Jouniaux, P. Sailhac, P.-D. Matthey, and M. Zillmer, 2011: Dependence of seismoelectric amplitudes on water content. *Geophysical Journal International*, **187 (3)**, 1378–1392, doi:10.1111/j.1365-246x.2011.05232.x.

Strahser, M. H., W. Rabbel, and F. Schildknecht, 2007: Polarisation and slowness of seismoelectric signals: a case study. *Near Surface Geophysics*, **5 (2)**, 97–114, doi: 10.3997/1873-0604.2006022.

Süer, S., N. Güleç, H. Mutlu, D. R. Hilton, C. Çifter, and M. Sayin, 2008: Geochemical Monitoring of Geothermal Waters (2002–2004) along the North Anatolian Fault Zone, Turkey: Spatial and Temporal Variations and Relationship to Seismic Activity. *Pure and Applied Geophysics*, **165 (1)**, 17–43, doi:10.1007/s00024-007-0294-4.

Sun, Y.-C., and Coauthors, 2019: Numerical simulations to explain the coseismic electromagnetic signals: a case study for a M5.4 aftershock of the 2016 Kumamoto earthquake. *Earth, Planets and Space*, **71 (1)**, doi:10.1186/s40623-019-1122-7.

Taner, M. T., F. Koehler, and R. E. Sheriff, 1979: Complex seismic trace analysis. *GEOPHYSICS*, **44 (6)**, 1041–1063, doi:10.1190/1.1440994.

Tank, S. B., and Coauthors, 2003: Resistivity structure in the western part of the fault rupture zone associated with the 1999 İzmit earthquake and its seismogenic implication. *Earth, Planets and Space*, **55 (7)**, 437–442, doi:10.1186/bf03351777.

Thompson, A. H., and G. A. Gist, 1993: Geophysical applications of electrokinetic conversion. *The Leading Edge*, **12 (12)**, 1169–1173, doi:10.1190/1.1436931.

Thompson, A. H., and Coauthors, 2007: Field tests of electroseismic hydrocarbon detection. *GEOPHYSICS*, **72 (1)**, N1–N9, doi:10.1190/1.2399458.

Thompson, R. R., 1936: THE SEISMIC ELECTRIC EFFECT. *GEOPHYSICS*, **1 (3)**, 327–335, doi:10.1190/1.1437119.

Thompson, R. R., 1939: A NOTE ON THE SEISMIC-ELECTRIC EFFECT. *GEOPHYSICS*, **4 (2)**, 102–105, doi:10.1190/1.1440485.

Tunc, B., and Coauthors, 2011: The Armutlu Network: an investigation into the seismotectonic setting of Armutlu–Yalova–Gemlik and the surrounding regions. *Annals of Geophysics*, **54 (1)**, 35–45, doi:10.4401/ag-4877.

Warden, S., S. Garambois, L. Jouniaux, D. Brito, P. Sailhac, and C. Bordes, 2013: Seismoelectric wave propagation numerical modelling in partially saturated materials. *Geophysical Journal International*, **194 (3)**, 1498–1513, doi:10.1093/gji/ggt198.

Warden, S., S. Garambois, P. Sailhac, L. Jouniaux, and M. Bano, 2012: Curvelet-based seismoelectric data processing. *Geophysical Journal International*, **190 (3)**, 1533–1550, doi:10.1111/j.1365-246x.2012.05587.x.

Wessel, P., W. H. F. Smith, R. Scharroo, J. Luis, and F. Wobbe, 2013: Generic Mapping Tools: Improved Version Released. *Eos, Transactions American Geophysical Union*, **94 (45)**, 409–410, doi:10.1002/2013eo450001.

Woith, H., 2015: Radon earthquake precursor: A short review. *The European Physical Journal Special Topics*, **224 (4)**, 611–627, doi:10.1140/epjst/e2015-02395-9.

Woith, H., R. Wang, D. Caka, T. S. Irmak, B. Tunc, B.-G. Luehr, and S. Baris, 2014: Seismically induced pressure transients at geothermal reservoirs in the eastern Marmara region. *EGU General Assembly Conference Abstracts*, EGU General Assembly Conference Abstracts, Vol. 16, 9586.

Woith, H., R. Wang, U. Maiwald, A. Pekdeger, and J. Zschau, 2013: On the origin of geochemical anomalies in groundwaters induced by the Adana 1998 earthquake. *Chemical Geology*, **339**, 177–186, doi:10.1016/j.chemgeo.2012.10.012.

Wyss, M., 1997: Second round of evaluations of proposed earthquake precursors. *Pure and Applied Geophysics*, **149 (1)**, 3–16, doi:10.1007/bf00945158.

Wyss, M., and D. C. Booth, 1997: The IASPEI procedure for the evaluation of earthquake precursors. *Geophysical Journal International*, **131 (3)**, 423–424, doi:10.1111/j.1365-246x.1997.tb06587.x.

Yavuz, E., D. Çaka, B. Tunç, T. Serkan Irmak, H. Woith, S. Cesca, B.-G. Lühr, and Ş. Barış, 2015: Earthquake Swarm in Armutlu Peninsula, Eastern Marmara Region, Turkey. *EGU General Assembly Conference Abstracts*, EGU General Assembly Conference Abstracts, Vol. 17, 5099.

Yılmaz, Y., Ş. Genç, E. Yiğitbaş, M. Bozcu, and K. Yılmaz, 1995: Geological evolution of the late Mesozoic continental margin of Northwestern Anatolia. *Tectonophysics*, **243 (1-2)**, 155–171, doi:10.1016/0040-1951(94)00196-g.

Zhang, H., Z. Shi, G. Wang, X. Sun, R. Yan, and C. Liu, 2019: Large Earthquake Reshapes the Groundwater Flow System: Insight From the Water-Level Response to Earth Tides and Atmospheric Pressure in a Deep Well. *Water Resources Research*, **55** (**5**), 4207–4219, doi:10.1029/2018wr024608.

Zyserman, F., L. Monachesi, and L. Jouniaux, 2016: Dependence of shear wave seismoelectrics on soil textures: a numerical study in the vadose zone. *Geophysical Journal International*, **208** (**2**), 918–935, doi:10.1093/gji/ggw431.

Zyserman, F., L. Monachesi, and L. Jouniaux, 2017: Reply to 'Comment on "Dependence of shear wave seismoelectrics on soil textures: a numerical study in the vadose zone by F.I. Zyserman, L.B. Monachesi and L. Jouniaux" by Revil, A.'. *Geophysical Journal International*, **210** (**3**), 1652–1658, doi:10.1093/gji/ggx262.

List of Figures

List of Tables

Acknowledgements

Many people have supported me throughout the creation of this thesis.

First of all I would like to thank my supervisor Wolfgang Rabbel for his support, advise and constant help. Thank you for always finding ways to fund my work and giving me the opportunity to visit numerous conferences around the globe.
A special thanks is also directed at Martin Thorwart, co-author of all my papers. Thank you for always finding time for me, the fruitful discussions and necessary encouragements.
I would like to thank Stéphane Garambois for agreeing to be the second examiner as well as all members of my defence committee.
I am grateful to Oliver Ritter and Jaime Araya Vargas from GFZ Potsdam for providing the SE field data from the MT-stations of the IPOC network in Chile and their support in ‘understanding’ the data. I am furthermore grateful to Michel Dietrich, Stéphane Garambois and Sheldon Warden for letting me use their SE modelling code with which the calculations for this thesis were performed and their helpful input when questions arose.

This thesis would not exist without funding. I am especially grateful for the 2-year-funding from the *Landesgraduiertenstipendium zur Förderung des wissenschaftlichen und des künstlerischen Nachwuchses* from the federal state Schleswig-Holstein without which I would probably never have started to work on this thesis. I would also like to thank the *DAAD* for giving me the opportunity to visit two consecutive AGU conferences in the USA via their ‘Kongressreisenprogramm’.

Thank you to all members of the *Angewandte Geophysik* working group. I enjoyed being part of your team and our sharing of ideas, tasks and lunchtimes. A special Thanks is thereby included to my fellow phd-students: Katharina, Johanna, Michaela, Annika, Rebekka, Erica, Natalie and Diana. Thanks for sharing this time with me and your support during the good but especially the exhausting times (‘We’re all in this together’). Thank you, Micha, for motivating me to go to the gym, Annika, for always making me laugh and Johanna, for being the best office-mate imaginable.
And to Katha: You know my work wouldn’t be the same without you. Your read all my texts, listened to all my talks, designed all my posters,... Thank you for bearing with me in the last 13 years in- and outside of University (and especially in the last 6 month in which you had to endure my constant complaining; I promise, it’s over now).
I would also like to thank my ‘new’ colleagues from the Dezernat 64 at the *Landesamt für Landwirtschaft, Umwelt und ländliche Räume (LLUR)*. You introduced me to a work-life outside of the University while allowing me to pursue this thesis, always being interested in the ‘current status’.

Last but not least I would like to thank my friends and family.
Thank you, Nadine, for guiding me through the academic jungle, your constant pushing and encouragement as well as moral support, Katha and Ina, for making me feel home, Hanna, for the endless telephone calls, Liana, for reminding me of a life outside of the University and Moritz, for the fun game nights. Thank you to the rest of my Geophysik-Friends (Kerstin, Linda, Anke, Kim) for the shared time during our studies (and beyond) and to my BaLi-Girls (and Boys) for being the coolest and most loyal group of school-friends imaginable.
Thank you to my parents Susanne and Wolfgang, for always letting me pursue my goals, supporting me in every imaginable way. Thank you to my sister Lene, for being a great roommate, accepting my messiness and taking care of our home-duties, especially during my crunch-times and to my sister Linda, for your support via the phone and the relaxing and much needed vacations.

Everyone mentioned and many more not mentioned here helped me to finish this thesis, each in their individual way. So again:

THANKS TO ALL OF YOU

... and now, let a new chapter begin!

Erklärung

Diese Arbeit ist – abgesehen von den angegebenen Hilfsmitteln und der Beratung durch meinen Betreuer – nach Form und Inhalt meine eigene. Die Arbeit hat weder ganz noch zum Teil schon einer anderen Stelle im Rahmen eines Prüfungsverfahren vorgelegen. Die Arbeit wurde – mit Ausnahme der einbezogenen und gekennzeichneten Publikationen – weder veröffentlicht noch zur Veröffentlichung eingereicht. Die Arbeit ist unter Einhaltung der Regeln guter wissenschaftlicher Praxis der Deutschen Forschungsgemeinschaft entstanden. Ein akademischer Grad wurde nicht entzogen.

Kiel, April 2020

(Laura Dzieran)